

Aus dem Institut für Molekular- und Zellbiologie
der Hochschule Mannheim
(Direktor: Prof. Dr. rer. nat. Mathias Hafner)

Optimizing Microscopy in Three Dimensions: Optical Clearing Techniques for
the Study of hiPSC-Derived Neural Spheroids and 3D Cell Cultures

Inauguraldissertation
zur Erlangung des Doctor scientiarum humanarum (Dr. sc. hum.)
der
Medizinischen Fakultät Mannheim
der Ruprecht-Karls-Universität
zu
Heidelberg

vorgelegt von
Elina Nürnberg

aus
Schwetzingen

2023

Dekan: Prof. Dr. med. Sergij Goerd
Referent: Prof. Dr. rer. nat. Mathias Hafner

Table of contents

	Page
Abbreviations.....	iv
List of figures	vi
List of tables	viii
1 Introduction	1
1.1 3D-Cell culture.....	1
1.1.1 Scaffold-free techniques	2
1.1.2 Scaffold-based techniques	3
1.1.3 Microfluidic organ-on-a-chip techniques	4
1.2 Confocal microscopy and optical sectioning	5
1.3 Interaction of light and matter.....	8
1.3.1 Reflection, transmission, and absorption of light.	9
1.3.2 Diffraction and interference.....	9
1.3.3 Refraction and scattering of light.	12
1.4 Optical tissue clearing.....	14
1.4.1 Organic solvent-based techniques	16
1.4.2 High-refractive index aqueous solutions	18
1.4.3 Hyperhydration-based techniques.....	19
1.4.4 Tissue transformation	21
1.5 Optical clearing of 3D-cell culture models	22
1.6 Aims of this study	27
2 Material and Methods.....	28
2.1 Cell culture.....	28
2.1.1 Cell Lines.....	28
2.1.2 Cell culture methods and spheroid generation.....	28
2.1.3 Dynarray co-culture model.....	31
2.2 Immunofluorescence stainings.....	31
2.2.1 Fixation of spheroids and co-culture models.....	31
2.2.2 Preparation of cryosections and immunofluorescence labeling of spheroid sections	32
2.2.3 Whole-mount immunofluorescence.....	33
2.3 Optical clearing.....	34
2.3.1 Embedding in PBS and Mowiol	34

2.3.2	88 % Glycerol.....	34
2.3.3	Clear ^{T2}	35
2.3.4	CytoVista.....	35
2.3.5	ScaleS.....	35
2.4	Microscopy.....	36
2.4.1	Confocal microscopy.....	36
2.4.2	Light sheet microscopy.....	37
2.5	Image processing and analysis.....	37
2.5.1	Measurement of spheroid diameter and depth-dependent signal intensity.....	37
2.5.2	Depth-dependent signal-to-noise ratio.....	37
2.5.3	3D-Segmentation of nuclei.....	38
2.5.4	Statistical analysis.....	38
3	Results.....	39
3.1	hiPSC-derived neural spheroids for exploring OTC protocols in 3D-cell cultures.....	39
3.1.1	Proliferation of hiPSC-derived neural spheroids is decreased upon FGF2-exposure.....	39
3.1.2	3D-cultivation of hiPSC derived neural spheroids maintains a steady pool of SOX2+ NPCs throughout differentiation.....	42
3.2	Optical clearing of hiPSC-derived neural spheroids.....	44
3.2.1	Post-fixation sample size of B7_033#1NPC1 spheroids is best preserved by ScaleS.....	44
3.2.2	Optical clearing techniques alter fluorophore signal intensity, sample size, and optical transparency of hiPSC-derived neural spheroids.....	45
3.2.3	Simple immersion in a high refractive index aqueous solution of glycerol highly improves imaging depth and image quality in B7_033#1NPC1 spheroids.....	48
3.2.4	Glycerol-based optical clearing yields superior imaging and segmentation quality in hiPSC-derived neural precursor spheroids.....	51
3.2.5	Glycerol clearing of differentiated hiPSC-derived neural spheroids reveals intricate networks of neurons and astrocytes.....	54
3.3	Comparison of optical clearing protocols across different 3D-cell culture models.....	56
3.3.1	Cell line dependent sample volume changes are best prevented by ScaleS and glycerol clearing.....	56
3.3.2	Depth-dependent signal intensity and SNR vary across cell lines, OTC methods and fluorophores.....	60
3.3.3	Efficiency of optical clearing is influenced by the complexity of 3D-cell culture models.....	64
3.3.4	Optical clearing with glycerol consistently improves nuclear segmentation across cell culture models.....	68
3.3.5	Application of z-compensation significantly improves image segmentation in glycerol cleared spheroids.....	70

4 Discussion	74
4.1 Generation of a 3D-spheroid model from hiPSC-derived NPCs	75
4.1.1 hiPSC-derived NPCs form spheroids by a self-driven mechanism	75
4.1.2 3D-cultured hiPSC neural spheroids maintain constant levels of SOX2+ NPCs throughout differentiation.....	76
4.2 Optical clearing of hiPSC-derived neural spheroids for whole mount microscopy.....	78
4.2.1 Aqueous hyperhydration with ScaleS preserves sample dimensions	79
4.2.2 Optical clearing with glycerol enhances light penetration into hiPSC-derived neural spheroids and image quality in depth	80
4.2.3 Optical clearing with glycerol and ScaleS enable semi-automated segmentation of entire hiPSC-derived spheroids.....	82
4.2.4 Combining optical clearing with glycerol and LSM enables 3D-microscopy of entire neural spheroids.....	83
4.3 Comparison of OTC protocols across cell lines.....	84
4.3.1 Sample size preservation, optical transparency and image quality vary across cell lines.....	84
4.3.2 Optical tissue clearing efficiency is challenged by the complexity of 3D-cell culture models.....	85
4.3.3 Implementation of z-compensation into the imaging process improves data segmentation in optically cleared spheroids.....	86
4.4 Conclusion and outlook	87
5 Summary	89
6 Zusammenfassung	91
7 References.....	93
8 Appendix.....	107
8.1 List of cell culture materials	107
8.2 Consumables and chemicals used for immunofluorescence and optical clearing experiments	108
8.3 Percentage loss of depth-dependent signal intensity in cleared B7_033#1NPC1 spheroids.....	109
8.4 Overview of fluorescence penetration and SNR in depth of simple spheroids sorted by cell type	110
8.5 Overview of fluorescence penetration and SNR in depth in complex 3D cell cultures.....	112
8.6 Publications.....	113
8.7 Statement on contributions, copyright, and self-plagiarism.....	114
9 Curriculum Vitae.....	116
10 Acknowledgments.....	116

Abbreviations

2D	Two-dimensional
3D	Three dimensional
3DISCO	3D imaging of solvent cleared organs
BABB	Benzyl alcohol and benzyl benzoate
BME	Basement membrane extract
BSA	Bovine serum albumin
CAS3	Cleaved caspase-3
CIP	Contact inhibition of proliferation
CLSM	Confocal laser scanning microscopy
CUBIC	Clear unobstructed brain imaging cocktails and computational analysis
DBE	Dibenzyl ether
DCM	Dichloromethane
DMEM	Dulbecco's Modified Eagle Medium
DMSO	Dimethyl sulfoxide
ECM	Extracellular matrix
EDTA	Ethylenediaminetetraacetic acid
ETC	Electrophoretic tissue clearing
FBS	Fetal bovine serum
GA	Glutaraldehyde
GAG	Glycosaminoglycan
GFAP	Glial fibrillary acidic protein
hASCs	Human adipose-derived stem cells
hiPSC	Human induced pluripotent stem cells
HTS	High throughput screening
IMDM	Iscove's Modified Dulbecco's Medium
iPSC	Induced pluripotent stem cell
LoG	Laplace of Gaussian
MCTs	Multicellular tumor spheroid
MEM-NEAA	Minimum Essential Medium Non-Essential Amino Acids
MSBB	Methyl-salicylate and benzyl benzoate
MW	Molecular weight
NA	Numerical aperture
NADPH	β -nicotinamide adenine dinucleotide phosphate
NPC	Neural precursor cell
OOAC	Organ-on-a-chip
OTC	Optical tissue clearing
PACT	Passive CLARITY technique
PBS	Phosphate-buffered saline
PEG	Poly(ethylene glycol)

Pen/Strep	<i>Penicillin/streptomycin</i>
PFA	<i>Paraformaldehyde</i>
PHEMA	<i>Poly(1-hydroxyethyl methacrylate)</i>
PLO	<i>Poly-L-ornithine</i>
PMT	<i>Photomultiplier tube</i>
PSF	<i>Point spread function</i>
PVA	<i>Siehe, Poly(vinyl alcohol)</i>
Quadrol	<i>N,N,N',N'-Tetrakis(2-hydroxypropyl)ethylenediamine</i>
RI	<i>Refractive index</i>
RIMS	<i>Refractive index matching solution</i>
ROI	<i>Region of interest</i>
RT	<i>Room temperature</i>
SDS	<i>Sodium dodecyl sulfate</i>
seeDB	<i>See deep brain</i>
SNR	<i>Signal-to-noise ratio</i>
SWITCH	<i>System-wide control of interaction time and kinetics of chemicals</i>
TDE	<i>2,2'-thiodiethanol</i>
THF	<i>Tetrahydrofuran</i>
TUBB3	<i>β III tubulin</i>
ULA	<i>Ultra-low attachment, Ultra-low attachment</i>

List of figures

Figure 1-1:	Cellular environment in 2D- and 3D-cultured cells	1
Figure 1-2:	Structure and microenvironment of spheroids.....	3
Figure 1-3:	Diffraction and PSF in confocal microscopy.	7
Figure 1-4:	Creation of a plane wave from single wavelets according to the Huygens' principle.....	10
Figure 1-5:	Characteristics of electromagnetic waves and wave interference.	11
Figure 1-6:	Creation of a diffraction pattern by wave interference.....	12
Figure 1-7:	Taxonomy of optical tissue clearing protocols.....	16
Figure 2-1:	Timeline of 3D-differentiation of hiPSC-derived NPCs into neurons and astrocytes.....	30
Figure 3-1:	Scaffold-free spheroids can be formed from hiPSC-derived NPCs.	40
Figure 3-2:	Proliferation and apoptosis in NPC-derived spheroids depend on FGF2 and cultivation time.....	41
Figure 3-3:	Distribution of marker protein stainings in NPC spheroids changes during differentiation.....	43
Figure 3-4:	Sample size preservation is best ensured by optical clearing with Sca/eS.	44
Figure 3-5:	The maintenance of fluorophore signal intensity, sample size, and optical transparency is variably influenced by optical clearing techniques.	46
Figure 3-6:	Optical tissue clearing with a glycerol performs superior and greatly improves light penetration into spheroids.	47
Figure 3-7:	Conservation of fluorescent signal intensity, depth-dependent SNR and sample clarity are clearing method-dependent.	49
Figure 3-8:	Optical clearing of hiPSC-derived neural spheroids enhances detection and quantification of cell nuclei with varying quality.....	53
Figure 3-9:	Optical clearing of neural spheroids reveals partial polarization and differentiation into neurons and astrocytes.	55
Figure 3-10:	Post-fixation sample volume changes are best averted by optical clearing with Glycerol and Sca/eS, in a cell line-independent matter.....	57
Figure 3-11:	Degree of sample volume change induced by clearing varies based on the cell line.	59
Figure 3-12:	Preservation of signal intensity, sample size, and optical transparency through optical clearing varies across different cell types.....	60
Figure 3-13:	Optical clearing with CytoVista consistently preserves high fluorescence intensity of DAPI, independent of the cell line.....	62
Figure 3-14:	Preserved high fluorescence intensity of DAPI upon CytoVista clearing is accompanied by increased depth-dependent SNR.....	63
Figure 3-15:	Optical clearing efficiency is affected by complexity of a spheroid-based tri-culture model.....	65
Figure 3-16:	ECFP fluorescence is preserved by optical clearing with glycerol and quenched by Clear ^{T2} in a chip-based co-culture model of breast cancer cells and fibroblasts.	67
Figure 3-17:	Optical clearing with glycerol consistently improves nuclear segmentation across cell lines.	69

Figure 3-18:	Stability of signal intensity and SNR profiles remains higher with z-compensation.	71
Figure 3-19:	Z-compensation improves semi-automated segmentation of nuclei in glycerol cleared spheroids.	72

List of tables

Table 1-1:	Wave-Particle Duality	8
Table 1-2:	Refractive indices of tissues, cells, and cellular components.	14
Table 2-1:	Overview of cell lines used in this study, including cell type, fluorescent labeling, and cell number used for sample generation.	29
Table 2-2:	Primary antibodies and fluorescent labels used for immunofluorescence staining of cryosections.....	33
Table 2-3:	Primary antibodies and fluorescent labels used for whole mount immunofluorescence stainings.	34
Table 2-4:	Composition of buffers used for whole mount immunofluorescence stainings.	34
Table 2-5:	Composition of solutions for Sca/eS tissue clearing protocols.	36
Table 3-1:	Summary of depth dependent DAPI signal loss and SNR in optically cleared B7_033#1NPC1 spheroids	49
Table 3-2:	Summary of depth dependent DRAQ5 signal loss and SNR in optically cleared B7_033#1NPC1 spheroids	50
Table 8-1:	List of cell culture materials.....	107
Table 8-2:	List of materials for immunofluorescence labeling and optical clearing.....	108
Table 8-3:	Percentage loss of depth-dependent signal intensity in cleared B7_033#1NPC1 spheroids.	109
Table 8-4:	Summary of depth-dependent signal loss and SNR in B7_033#1NPC1 spheroids.....	110
Table 8-5:	Summary of depth-dependent signal loss and SNR in HaCaT spheroids.....	110
Table 8-6:	Summary of depth-dependent signal loss and SNR in CCD-1137SK spheroids.....	111
Table 8-7:	Summary of depth-dependent signal loss and SNR in HT29 spheroids.....	111
Table 8-8:	Summary of depth-dependent signal loss and SNR in HTC-8 spheroids.....	111
Table 8-9:	Summary of depth-dependent signal loss and SNR in complex 3D-cell cultures.	112
Table 8-10:	Contributions from other persons.....	114

1 Introduction

1.1 3D-Cell culture

Since the first publications of *ex vivo* cultivation of living cells in the late nineteenth century¹, cell cultures have become a cornerstone in biological science and today play central roles in biomedical research, such as the investigation of underlying disease mechanisms or the field of drug discovery and development. Especially for the latter, *in vitro* cell culture has become an integral part in preclinical testing of potential drug candidates for the prediction of efficacy and toxicity. With most therapeutic compounds undergoing clinical trials failing in Phase II and III, the need for more predictive, reliable, and cost-effective test systems in the preclinical phase is ever-growing^{2,3}. Until recently, traditional cell-based assays focused exclusively on the two dimensional-like (2D) growth of cells on a flat, rigid surface. Despite their irrefutable contribution to experimental science, these monolayer cultures do not entirely recapitulate the native cellular environment, due to being mainly exposed to an artificial surface, e.g., glass or plastic, and having limited opportunity to form cell-cell-contacts and adhesion sites. Furthermore, the equal exposure to nutrients and oxygen, absent accumulation of metabolic waste products and facilitated migration potential due to the absence of an extracellular matrix (ECM) contribute to non-physiological culture conditions⁴⁻⁷. However, in multicellular organisms, cells grow in clusters, organizing themselves from function-specific tissues to multifunctional organs and organ systems with the inherent characteristic of spreading in all three spatial dimensions^{8,9}. As a result, three dimensional (3D) aggregates of cells display an increased number of intercellular contact sites and interactions with the surrounding ECM, as well as gradients of signaling molecules, nutrients, and oxygen (Figure 1-1). These changes to the microenvironment of cells have been shown to elicit alterations in gene expression profiles and influence signaling pathways associated with differentiation, proliferation, and apoptosis¹⁰⁻¹⁴.

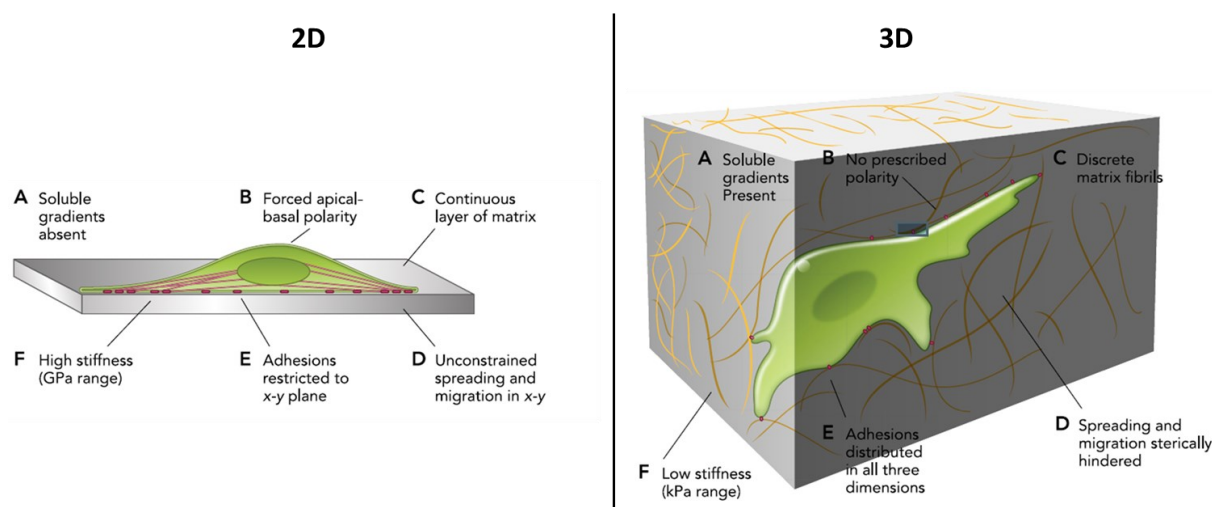


Figure 1-1: Cellular environment in 2D- and 3D-cultured cells. Schematic image shows differences in the cellular microenvironment with respect to nutrient and oxygen gradients (A), cell polarity (B), ECM properties (C, F), migration potential (D), and cellular adhesion sites (E). Adapted from Baker and Chen (2012)⁴ and Duval et al. (2017)⁵. Rights obtained for use.

In a 2D *in vitro* environment, homogeneously distributed nutrients, facilitated diffusion of gases and regular removal of metabolic waste products make programmed cell death usually a consequence of non-ideal culture conditions or drug treatment. Cell lines cultured as a monolayer usually maintain a proliferative state until lack of space and reduced spatial proximity to neighboring cells induce a process called contact inhibition of proliferation (CIP), where cells exit the repetitive cycle of cell division due to mechanical cues introduced by increased formation of cell-cell-contacts^{15,16}. In contrast, *in vivo* proliferation and apoptosis of cells are highly regulated processes, and their balance plays a crucial role during embryonic development and in pathological processes like wound healing or cancer^{14,17–20}. In the recent years, a large variety of 3D-cell culture models have been developed, that recapitulate important aspects of cellular behavior in a more physiological way, compared to their 2D-counterpart. Especially with respect to drug development, many of these models have been shown to be more predictive with respect to drug efficacy and safety, and thus highlighting their potential as a standard complement to classical 2D-cell culture and animal testing in preclinical trials. In the following, the most common, well-established types of 3D-culture models are summarized.

1.1.1 Scaffold-free techniques

Scaffold-free methods for the generation of 3D-cell cultures do not use additional material to provide structure to cell clusters, but instead only rely on aggregation by intercellular adhesion. One of the oldest and, until today, most common method for generating 3D aggregates of cells uses spatial proximity of cells in suspension and their inherent tendency to form cell-cell-contacts. Already at the beginning of the 20th century, aiming to examine the outgrowth of nerve fibers, Ross G Harrison was not only one of the first scientists to show that primary cells can be cultured outside of the living organism, but also applied the hanging drop method, initially developed by bacteriologists, to successfully cultivate neuroblasts in a 3D-format and demonstrate active nerve growth *in vitro*²¹.

The hanging drop method consists of a flat surface, e.g., the lid of a 96-well cell culture plate, on which small droplets of medium with singularized cells are transferred and carefully inverted. After inverting the plate, physical forces like surface tension will prevent the drop from falling, while cells are forced into close proximity by gravity and start to adhere to each other by formation of intercellular contact sites. Within a timeframe that is cell line-dependent, aggregation of cells proceeds until a compact cluster, termed spheroid, is formed.

Despite being one of the oldest techniques, the hanging drop method is still widely applied. For example, a variety of studies have shown, that culturing hepatocyte-like cells, like the HepG2 or HepRG cell lines in a hanging drop system significantly increases expression of genes associated with primary hepatocyte function, making them a suitable system to analyze liver toxicity of substances. Moreover, this culture also enables high throughput screenings (HTS)^{22–24}. Therefore, this technique is still widely used for drug screening in multicellular tumor spheroids (MCTs), highlighting the applicability in the preclinical phase of drug development^{25–31}.

Over the last decades, new advances in cell culture devices, like surface modification of glass and plastics by either chemical or physical modification, have brought forth the development of cell-repellent surfaces. By using the same mechanisms that take effect in the hanging drop method, cell culture vessels with ultra-low attachment (ULA) surfaces prevent cells from adhering and use their inherent drive to cluster together, however without the sensitive handling of free droplets. Commercially available multiwell formats are nowadays widely used for the generation of spheroids^{32–36} and more advanced models, e.g., co-cultures^{37–41} and organoids^{42–46}.

Spheroids generated with these methods often display a distinct patterning, that consists of an outer proliferative layer of cells, a non-proliferative zone where residing cells enter a quiescent state, and, depending on the size of the spheroid, an inner necrotic core, where cells die due to a lack of oxygen and nutrients, e.g., glucose (Figure 1-2)^{3,47}. Especially in the field of cancer research, these features of spheroidal 3D-cell culture models recapitulate important physiological aspects of tumor biology, making this method an ideal candidate for preclinical drug testing^{48,49}.

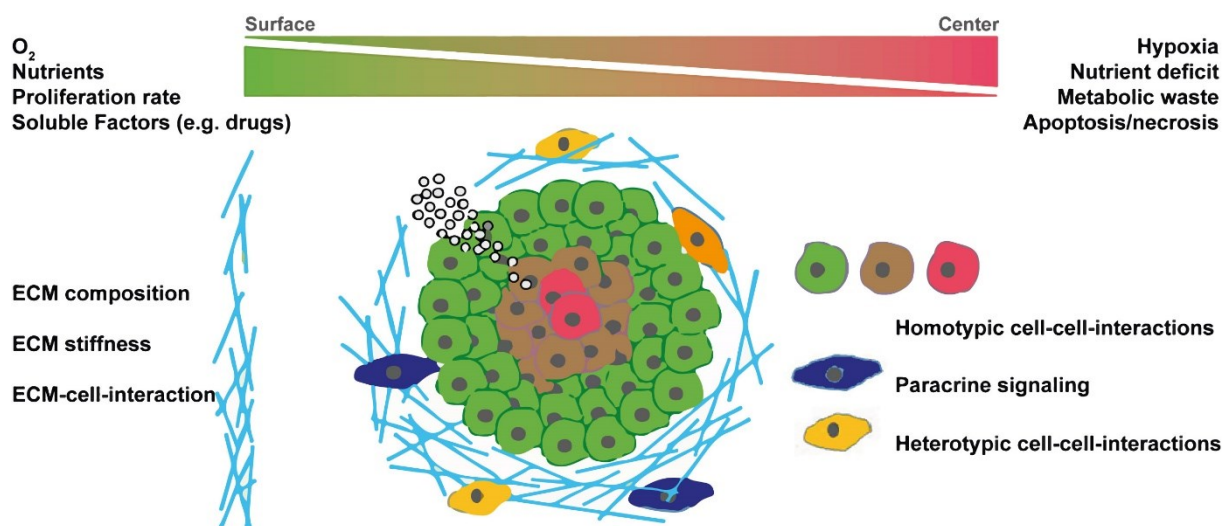


Figure 1-2: Structure and microenvironment of spheroids. Due to gradients of nutrients, oxygen and metabolic waste, cells cultured as a 3D-spheroid often display a distinct patterning with actively proliferating cells in the outer region (green), a non-proliferative, quiescent layer (brown), and a necrotic core (red). Additionally, interactions with ECM proteins (light blue) and other cell types (yellow, dark blue) define the microenvironment. Taken and adapted from Langhans et al. (2018)³ according to the Creative Commons Attribution License (CC BY 4.0)

1.1.2 Scaffold-based techniques

In some cases or specific applications, certain cell types may need additional structural support to grow in 3D or to adapt a certain phenotype.^{37,50} This can be achieved by providing cells with a natural or synthetic scaffold that mimics the presence of an ECM and serves not only as structural support but can also provide biochemical and mechanical cues. Alongside fibrous scaffolds, hydrogels - networks of cross-linked polymer chains, where the void in between chains is occupied by aqueous fluids - are nowadays one of the most used biomimetic ECM-like materials due to their ability to emulate important characteristics of most soft tissues. Synthetic materials, which are often used for the fabrication of hydrogels, are poly(ethylene glycol) (PEG)^{51–54}, poly(vinyl alcohol) (PVA)^{55–57}, and poly(1-

hydroxyethyl methacrylate) (PHEMA)⁵⁸⁻⁶⁰ and can be advantageous due to their chemically controlled composition and matrix architecture⁶¹⁻⁶³. However, synthetic polymers cannot entirely mimic the complexity of ECM architecture due to their inability to provide biochemical signaling molecules. Although this can be partially compensated for by functionalizing polymers with such biomolecules, natural hydrogels provide a more physiological composition^{64,65}. The mammalian ECM is composed of approximately 300 different proteins, also termed the matrisome, that vary in their composition in a tissue-specific manner, however, the major players can be subdivided into three groups: collagens, proteoglycans, and glycoproteins. With at least 28 different subtypes, collagens make up the backbone of the ECM to provide structural support and interaction sites for cells and other ECM components. Located in between collagen fibrils, proteoglycans (glycoproteins with one or more side chains of glycosaminoglycans (GAGs)) are responsible for providing lubricating properties to the ECM by binding water molecules and influencing signaling pathways by binding certain ions and secreted factors. The last large group of ECM macromolecules are glycoproteins, like laminins and fibronectins, which exert a vast variety of functions, such as assisting in cell adhesion, cell signaling and binding of growth factors to build up extracellular reservoirs⁶⁶⁻⁷⁰. Nowadays, commercially available ECM extracts, like Matrigel[®], GelTrex or BME, are often used for the preparation of scaffold-based 3D-cell cultures. However due to their non-defined composition and batch-to-batch variation, results obtained from those models must be interpreted with caution.

A new method of creating scaffold-based cell culture models has arisen together with the increased availability of 3D-printers and the corresponding technology⁷¹. Bioprinting, as reviewed by Moroni et al. (2018), can be defined as “the use of computer-aided transfer process for the patterning and assembly of living and non-living materials with a defined 2D or 3D architecture to produce bioengineered structures”⁷². Most common is the method of extrusion-based bioprinting, where hydrogels are printed in the form of continuous filaments by pneumatic extrusion through a nozzle, into a pre-designed shape that is application-specific⁷³. Singularized cells or already formed aggregates can be either resuspended into bio-inks prior to the printing process or subsequently transferred onto the printed structure. Those bio-inks can be selected according to the requirements of the research question, cellular model and, ultimately, the necessary physical properties, which are needed for the realization of a specific design^{72,74-82}.

1.1.3 Microfluidic organ-on-a-chip techniques

Despite capturing important hallmarks of physiology, the application of solely scaffold-free or scaffold-based 3D-cell culture models faces certain limitations when it comes to mimicking certain aspects, such as continuous medium supply, and therefore shear stress; vasculature, or tissue specific gradients of signaling molecules and spatial organization⁸³. In order to overcome these limitations, the combination of microfluidic systems, perfusable devices with micron-sized channels that work with very small volumes⁸⁴, and 3D-cell culture models has led to the development of organ-on-a-chip (OOAC) systems.

Having control over the spatial positioning of cells, e.g., in defined compartments interconnected by channels or a layered orientation of different cell types, allows to establish co-cultures, that recreate tissue architecture more precisely^{83,85–87}. Perfusion of channels enables the generation of short-term gradients when applying chemical cues, and stable, long-term gradients, as often found *in vivo* during embryonic development, angiogenesis and cancer cell migration, can be achieved by combining OOACs with hydrogels that provide said gradients^{88–96}.

1.2 Confocal microscopy and optical sectioning

In a historical context, the invention of microscopes went alongside the development of telescopes and associated techniques to grind and polish glass lenses. The earliest microscopes, called simple microscopes, were plain magnifying glasses made up of one convex lens with a magnification power of 6x to 10x. Beyond those scales, higher magnification was limited by optical effects and the need for techniques to produce smaller lenses. These obstructive effects are caused by spherical and chromatic aberration, introduced by the curved geometry of lenses and the inherent behavior of light^{97,98}. Spherical or lens aberration occurs due to the curved surface of a lens, which causes light to be refracted depending on its incidence angle with respect to the optical axis. The resulting image appears to be distorted and blurry in the periphery. Chromatic aberration describes the wavelength-dependent refraction of light, leading to light of different wavelengths being focused on different focal points along the optical axis and the colors of the image to be distorted and fringed⁹⁹.

In the late 16th century, Zaccharias Janssen discovered a way to reach higher magnification by combining multiple lenses and thereby creating the first compound microscope^{100,101}. With these optical systems, important hallmarks of biological discoveries, such as the Robert Hooke's observation of cork cells in 1665, were finally possible. However, despite reaching higher magnification, compound microscopes were not frequently used. Image distortion caused by optical aberration, especially spherical aberration, increases with the number of lenses in a system resulting in essentially unusable images. For this reason, simple microscopes were still the method of choice for microscopic observations during those times¹⁰².

It was not until the 19th century, that compound microscopes took the leading role in microscopic research. Advancements in manufacturing of lenses, new materials and sophisticated optical setups enabled new developments to improve image distortion, e. g. minimizing chromatic aberration by using achromatic or apochromatic lenses. Furthermore, new techniques for the specific visualization of biological structures, such as hematoxylin and eosin staining, opened new possibilities.

The method of widefield microscopy, which is the combination of compound microscopes and fluorescence microscopy, proved to be a powerful tool in biological research, which led to countless new discoveries on the mechanisms and workings of cells. However, it comes with specific limitations. Most of all, in widefield microscopy, the entire specimen is illuminated by the light source, not just the plane of focus^{103,104}. This leads to out-of-focus light from above and below the focal plane and which

contributes to the amount of lateral light scattering and reflection. This results in poor resolution and blurriness of the image. Additionally, the illumination of the entire sample leads to fast photo-bleaching of the fluorophores outside of the focal plane and a reduced intensity of emitted light over time. To overcome those obstacles, Marvin Minsky developed a new type of microscope in the 1950s which revolutionized modern microscopy, and which remains among the most used technical setups used today¹⁰⁵.

The first of many differences between conventional widefield and confocal microscopes, is the light source and the way a specimen is illuminated. Instead of bathing the whole specimen in light, confocal microscopes use a point source of light, e.g., a monochromatic laser emitting light of a single wavelength, which is focused on only a small spot of the entire sample, thereby drastically reducing the amount of out-of-focus light¹⁰⁴. The emitted light from excited fluorophores is then collected by a series of mirrors and lenses, and focused on a small pin hole aperture, which further reduces the amount of light from outside the focal plane by letting pass only light from the illuminated spot. Light passing the pinhole is then transmitted onto a detector, such as a photomultiplier tube (PMT) and translated into a digital signal which can be interpreted by computers¹⁰⁴. The microscope then moves the excitation light across the sample, building up an image pixel by pixel. The resulting digital representation of those pixels is an image of the focal plane. Additionally, by moving the excitation beam not only in the x- and y-direction but also in depth (the z-direction), a series of 2-dimensional images through the sample can be created (a process known as optical sectioning), which can be computationally realigned to create a 3D-reconstruction of the specimen¹⁰⁴. In prior times, when computational resources and suitable algorithms were not available yet, these reconstructions had to be done manually in a time-consuming and tedious process. Nowadays, however, many of those algorithms are already implemented in commercially available software, such as LASX (Leica Microsystems GmbH).

One might think that the resolving power of a confocal microscope, meaning the closest distance between two points in the focal plane, which can still be detected as separate signals, is defined by the magnification of the optical setup and the predefined number of pixels which are used to create the image of an optical section. Although those two factors do play a role, the resolving power of a confocal microscope is mostly determined by other factors, arising from the interaction of light and matter^{104,106,107}.

As previously mentioned, the excitation light of a confocal microscope passes through a small aperture called pinhole. As a result, diffraction, or the bending of electromagnetic waves, takes place. The details of this process are explained in chapter 1.3.2. Briefly, a plane wave of light is composed of countless small individual point sources of light, which interfere in a way that creates a plane wave front. Once this wave front passes a small aperture, the light is bent and the wave interference changes, creating a distinct diffraction pattern¹⁰⁶. In terms of confocal laser scanning microscopy (CLSM), this diffraction pattern is called point-spread-function (PSF) and appears in x-/ y-direction as a bright spot in the center

of the pattern surrounded by dimmer concentric rings, which decrease in intensity with increasing distance from the center (Figure 1-3)^{104,106}.

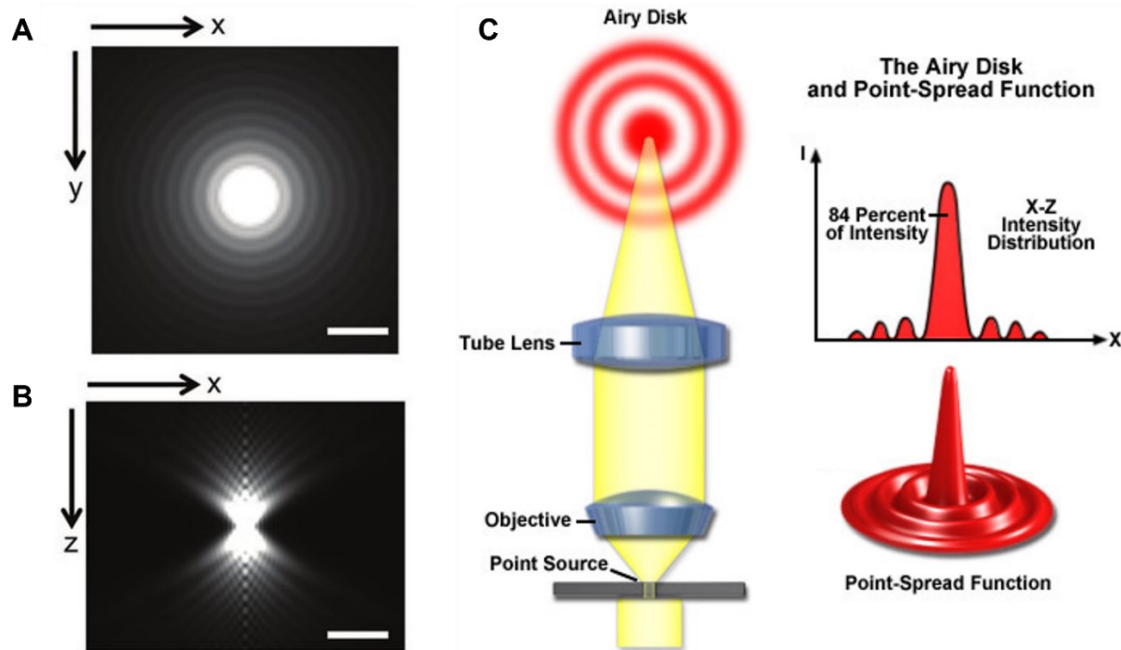


Figure 1-3: Diffraction and PSF in confocal microscopy. Exemplary profile of a point-spread-function (PSF) in the xy-plane (A) and xz-plane (B). A simplified representation of the beam path involved in the creation of the Airy disk is depicted in (C, left), as well as an intensity profile (C, upper right) and a 3D-representation of a PSF (C, lower right). Adapted from: (A,B) Herbert et al. (2012)¹⁰⁸, rights obtained for use; (C) Source: <https://zeiss-campus.magnet.fsu.edu/articles/basics/resolution.html>, accessed on 03/07/2023

However, what determines the shape of the PSF and therefore the resolving power of an optical system is not only determined by the presence or absence of a pinhole, but also on the properties of the objective to collect emitted light and separate the fringes around the central peak of the PSF¹⁰⁹. The measure to describe these properties is the numerical aperture (NA) and it is calculated as:

$$NA = n \cdot \sin(\alpha)$$

In this formula n describes the refractive index (RI) of the medium in which the specimen is embedded and the sine of half the angular aperture of the objective lens, which is the angle α that defines the cone of light entering the objective lens. The numerical aperture thus provides a measure of the ability of the objective lens to capture light from the specimen and to resolve fine details¹⁰⁹. In general, higher numerical aperture values indicate that more light can be captured, and finer details can be resolved, which results in higher-quality images. If the NA of an objective and the RI are known, the resolving power can be estimated according to the Rayleigh criterion¹⁰⁶:

$$Resolution_{xy} = \frac{0.61 \cdot \lambda}{NA} = \frac{0.61 \cdot \lambda}{n \cdot \sin(\alpha)} \quad Resolution_z = \frac{2 \cdot \lambda}{NA^2} = \frac{2 \cdot \lambda}{(n \cdot \sin(\alpha))^2}$$

It is important to note, that in the context of these formulas, the result is a distance in nm, and it is to be desired to be of low numbers. Therefore, a better resolution is reflected in low numbers. These formulas



highlight, that for an objective with a given, fixed angle α and a given wavelength λ , one way to decrease the resolution in either dimension is to increase the refractive index of immersion media. Additionally, they highlight, that for an objective with given NA, the resolution is smaller for lower wavelengths compared to high ones. Another fundamental principle in optical microscopy is the Abbe resolution limit or diffraction limit. It describes the minimal, wavelength dependent resolution for an optical system with a given numerical aperture as follows:

$$Resolution_{Abbe} = \frac{\lambda}{2 \cdot NA}$$

1.3 Interaction of light and matter

In order understand how optical systems such as microscopes work, how image artifacts are created and ultimately find ways to overcome these obstacles and limitations, one must understand the characteristics and underlying physics of light and its interaction with matter. For hundreds of years, great scientists, like Isaac Newton, Christiaan Huygens, James Clerk Maxwell, Albert Einstein, and Max Planck have been baffled by the nature and behavior of light. The research of Max Planck ultimately led to the back-then new scientific field of quantum physics. Today we know that light is electromagnetic energy, which propagates with both wave-like and particle-like properties¹¹⁰. This ambiguity is known as wave-particle-duality. Observable optical effects and whether they can be explained by wave- or particle-like behavior are summarized in Table 1-1. In the context of this chapter, however, the generalization applies that light can be regarded as a wave when travelling from one point to another.

Table 1-1: Wave-Particle Duality. Adapted from Sanderson (2019)^{97,110} (rights obtained for use)

Phenomenon	Explained in terms of waves 	Explained in terms of particles 
Reflection	Yes	Yes
Refraction	Yes	Yes
Interference	Yes	No
Diffraction	Yes	No
Polarization	Yes	No
Photoelectric effect	No	Yes

The main effects, which occur when light interacts with matter, e.g., a biological specimen, are, in order of occurrence, **reflection, transmission, absorption, and scattering**¹¹⁰. It is important to note these processes always take place, but it is the individual strength of each that contributes to the observable outcome of the interaction. In turn, what determines the dominating effect is dependent on nature and composition of the matter light interacts with.

1.3.1 Reflection, transmission, and absorption of light.

In the following, reflection, transmission, and absorption will be briefly described. However, since the process of light scattering is the most relevant type of light-matter interaction, it will be described in more detail in chapter 1.3.3. **Reflection** describes a directional change of an incoming wave upon interaction with matter at the interface¹¹⁰. Incoming light waves do not pass through the material and instead are reflected depending on their incident angle. For an ideal surface, incident angle and the angle of reflection are equal with respect to the normal of the surface (law of reflection). This behavior is essential in the design and properties of optical setups, such as microscopes, which use mirrors for directing the light path. For light rays that are not reflected, but instead pass the interface from one material into another, the process is termed transmission. **Transmission** describes the passage of light through a medium and is the dominating effect when light travels through translucent materials, such as glass¹¹⁰. **Absorption** of light defines the process in which the energy of an incoming electromagnetic wave is converted and absorbed by molecules of the interacting material. Thus, the intensity of the transmitted light is reduced and the order of magnitude of this reduction is dependent on the nature and density of the molecules. In contrast to the aforementioned effects, this process is best described by the particle theory of light, because the energy transfer occurs in discrete quanta¹¹⁰.

1.3.2 Diffraction and interference

Light diffraction, interference, and refraction describe the interaction between light waves and objects or boundaries they encounter. **Diffraction** of light is a process of especially high importance in microscopy and describes the bending of waves at the corner of an object or when waves pass through a small opening, such as the aperture of a confocal microscopes' pinhole or an objective¹⁰⁶. In fact, the observation that a plane wave entering a hole does not continue its path as a plane wave when leaving the aperture is what initially led to the wave theory of light, because this behavior could not be entirely explained by particles^{106,111}. In 1690, Huygens postulated a theory, today known as the Huygens' principle, which partially explained this behavior. He stated that every point on a wavefront is itself the source of a secondary circular wave, termed wavelet. Considering an infinitely large number of those wavelets, which mutually interfere, the formation of a plane wavefront from circular waves becomes clear (Figure 1-4)^{106,110}. Although Huygens did not explain the lack of backward propagation of waves and simply assumed that secondary waves travel only on the forward direction (this happened only in the 1990s), his theory contributed largely to the prediction of wave behavior.

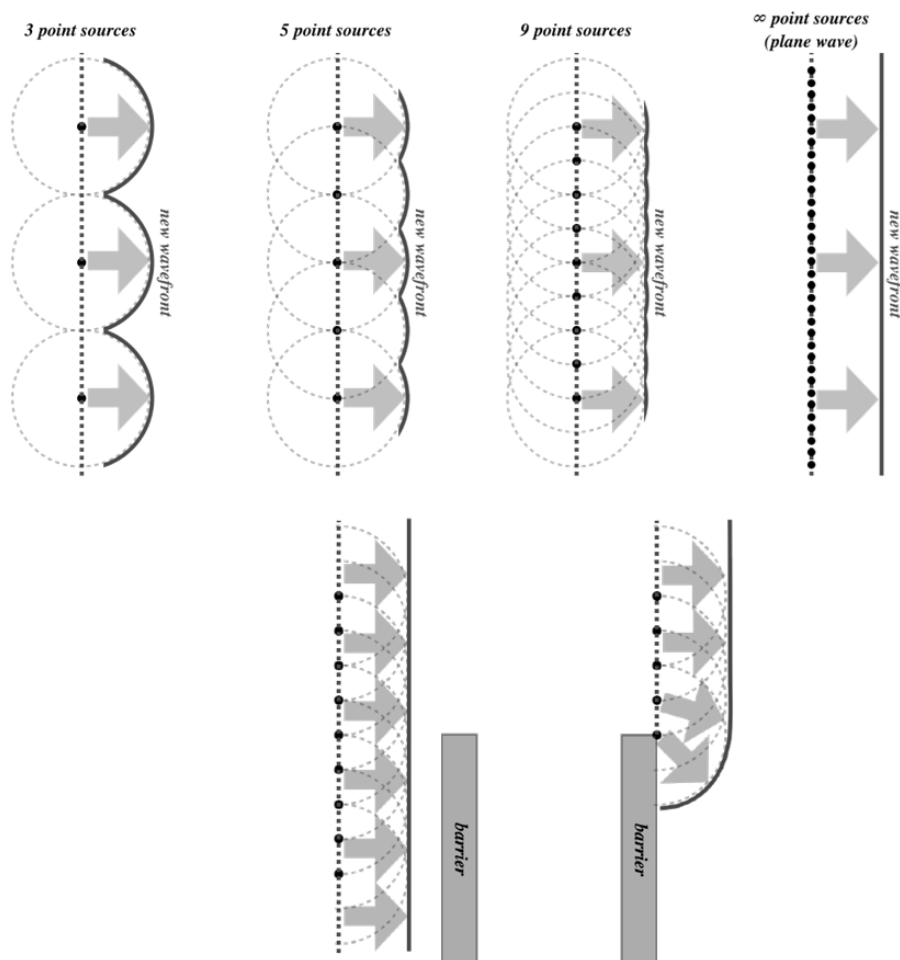


Figure 1-4: Creation of a plane wave from single wavelets according to the Huygens' principle. Circular waves emerging from point sources (wavelets) interfere to create a new wavefront. For a small number of point sources, the new wavefront appears wave-like. With an increasing number of point sources, the emerging wavefront appears smoother. For an infinite number of point sources, the new wavefront appears like a plane wave (upper panel). Upon encountering a barrier, a part of the wavefront is either reflected or absorbed, thus leading to a loss of destructive interference from secondary waves right at the boundary (lower panel). Adapted from: Libretexts.org, Physics7C, General Physics, Dina Zhabinskaya, UC Davis url: https://phys.libretexts.org/Courses/University_of_California_Davis/UCD%3A_Physics_7C_-_General_Physics/8%3A_Waves/8.7%3A_Double-Slit_Interference, accessed on: 04/06/2023

Another important observation can be made when observing the passage of light through a narrow opening, and it usually occurs in concordance with diffraction. When shining light in the form of a plane wave through one or even several narrow openings onto a surface, one would expect a slightly larger spot of light that is fringed at the edges. Instead, if the opening is small enough, a distinct pattern of alternating dark and bright regions becomes visible, with the brightest area in the middle and decreasing intensity away from the central beam^{106,110}. This pattern is the result of **interference** and describes the way in which two waves interact by adding their displacement, meaning their distance and direction in relation to the equilibrium (Figure 1-5).

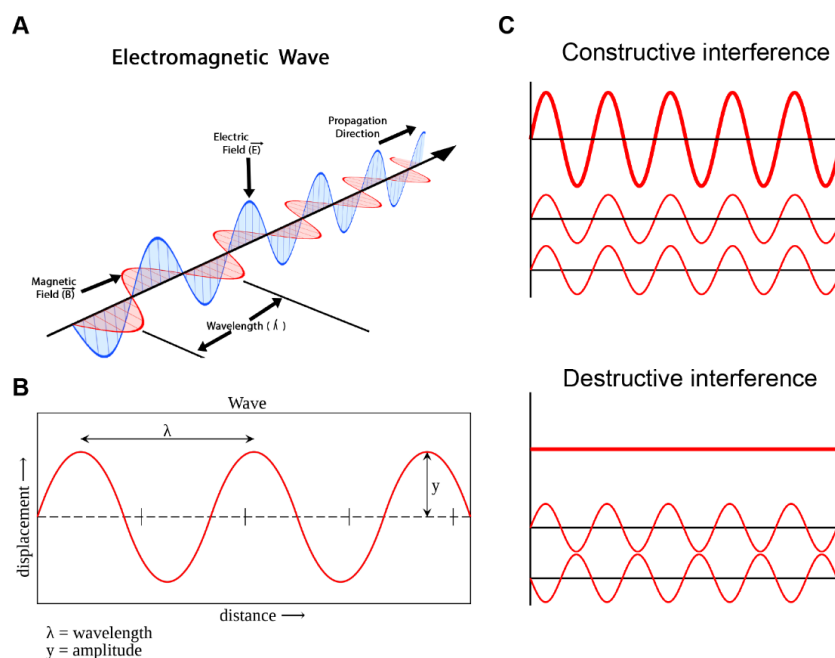


Figure 1-5: Characteristics of electromagnetic waves and wave interference. (A) Direction and propagation of electric and magnetic field components of an electromagnetic wave. (B) Important wave characteristics, e.g., wavelength λ and amplitude y . (C) Principle of constructive and destructive wave interference. Adapted from: (A) Kvapilová (2020)¹¹² according to the Creative Commons Attribution License (CC BY 3.0), (B) Wikimedia Commons, Wave characteristics, Licensing: public domain; url: https://commons.wikimedia.org/wiki/File:Wave_characteristics.svg, accessed on 03/05/2023, (C) Wikimedia Commons, Interference of two waves, Haade, Licensing: CC-BY-SA 3.0; url: https://commons.wikimedia.org/wiki/File:Interference_of_two_waves.svg, both accessed on 03/05/2023

In the special case of monochromatic light, the waves are coherent, having the same frequency and amplitude. If these waves are exactly an even order of magnitude of half a wavelength out of phase, the peaks of each wave meet, and the amplitude of the resulting wave is the sum of the two contributing waves. Contrary, if the two incoming waves are exactly an odd half of a wavelength out of phase, every peak meets a trough, and the two waves cancel each other out. These processes are known as complete constructive or destructive interference, respectively (Figure 1-5C)^{106,110}. But how does monochromatic light like a laser beam become out of synch, when passing through an opening? The answer to this question is diffraction. When light diffracts in different directions, waves will have to travel different path lengths to reach the same spot on a screen. This difference in path length causes the waves to be out of synch and interfere either constructively or destructively and create the characteristic striped diffraction pattern (Figure 1-6)¹⁰⁶. This pattern is highly relevant in confocal microscopy, as diffraction, interference, and refraction determine the PSF of an optical system and are irrefutably related to its resolving power. The details of this connection are discussed in chapter 1.2.

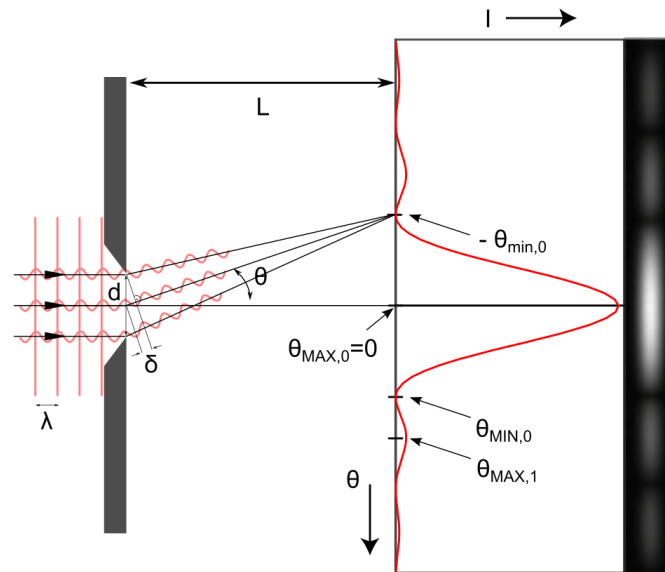


Figure 1-6: Creation of a diffraction pattern by wave interference. Diffraction of incoming plane waves of monochromatic light at a small opening, such as a microscope's aperture, causes initially synchronized waves to shift out of phase. If the path difference is exactly an odd number of halves of the wavelength, the waves will interfere destructively. Likewise, if the difference is an even number of halves of the wavelength, they will interfere constructively. Source: Wikimedia Commons, Single Slit Diffraction, jkrieger, Licensing: CC-BY-SA 3.0; url: https://commons.wikimedia.org/wiki/File:Single_Slit_Diffraction.svg, accessed on 03/05/2023

1.3.3 Refraction and scattering of light.

To comprehend how light behaves in different materials, it is crucial to understand the principles of diffraction and interference (chapter 1.3.2). However, the fundamental phenomena of refraction and scattering of light are particularly important in the interaction of light with biological tissues because they are among the most important influential factors determining the image quality. The level of detail and information one can infer from an image are depending on its resolution. As discussed in chapter 1.2, the resolution in turn is influenced by the NA of an objective and the index of refraction n . In this chapter, the focus will be on exploring the physical background of light refraction and principles of light scattering. **Refraction** refers to the redirection of light as it passes from one transparent medium to another, as opposed to diffraction, which describes the bending of waves around an obstacle^{107,110}. We observe refraction in our everyday lives, such as when objects appear to bend when submerged in water. In a vacuum, the speed of electromagnetic waves is the speed of light, but when particles are present, the speed of light appears slower due to the interaction of light waves with electrons and molecules. The interaction of an incoming electromagnetic wave with a molecule can cause the electrons to oscillate, creating a perpendicular electromagnetic field with the same frequency as the light wave^{107,110}. Additionally, some energy from the incoming light wave is transferred briefly to the outer electrons of molecules and then reemitted in the form of a spherical electromagnetic wave, which propagates in all directions, and which has the same energy and frequency. This process is known as elastic **scattering** since no energy loss occurs. Although only brief, these interactions result in a change of the apparent speed of light and bending of the light towards the normal of the interface^{107,110}.

The refractive index n , the ratio of the speed of light in a vacuum c to the speed of light in a medium v , is one measure to describe the behavior of light and the amount of light bending when passing from one transparent medium to another.

$$n = \frac{c}{v}$$

One should bear in mind, however, that the refractive index of a particular substance is not only influenced by the nature of the molecules it is made of, but also external physical factors, such as the temperature and the wavelength of the incident light¹¹³. It is important to note that scattering is a process which always takes place where molecules are present. So how can it be, that materials like glass or water appear transparent even though the molecules they are made of scatter the incoming light? The answer to this question lies in the concept of wave interference and its destructive or constructive effects (chapter 1.3.2)^{110,114,115}. In case of homogeneous, densely packed molecules, the distance between scatterers is much smaller than the wavelength of visible light (380 – 700 nm). An incoming plane wave sets the molecules in a plane into unison oscillation resulting in the emission of closely packed, spherical waves. Due their density, along the axes of the plane, almost every peak of a wave meets a trough resulting in nearly complete destructive interference in the lateral direction¹¹⁴. In contrast to lateral scattering, scatterers along the axis of the light's direction are set into vibration sequentially and always interfere constructively leading to the propagation of light in the forward direction^{114,115}.

With respect to biological samples, one reason for their opacity is the inhomogeneity of scatterers. Biological specimens are composed of an immensely large variety of molecules and structures, such as cell membranes, organelles, and extracellular matrices, which all have a distinguished RI^{110,116–119}. It is important to note, that the exact RI can vary depending on the concentration of said molecules, especially proteins, which is specific to the tissue or cellular identity. Additionally, refractive indices reported in literature for the same substance can vary due to differences in measurement techniques and conditions used during experimentation. Summarized in Table 1-2 are exemplary RIs obtained from different tissues, cell types or subcellular components. As explained previously, in the case of homogeneous densely packed molecules, the influence of lateral scattering is negligible. In biological samples, however, the heterogeneity of the sample causes the destructive interference of laterally scattered light to be reduced leading to an observable increase of diffuse light. With respect to microscopy, this diffuse light is displayed by an increased blurriness of the images^{114,115,118,119}.

Table 1-2: Refractive indices of tissues, cells, and cellular components. Adapted from Gul et al. (2021)¹²⁰ and Khan et al. (2021)¹²¹

Material	Refractive index	References
Water	1.33	
Refractive index of various human tissues and related components		
Bone	≈ 1.52 – 1.55	122–124
Hydroxyapatite	≈ 1.53 – 1.65	125,126
Enamel	≈ 1.63 – 1.65	127,128
Dentin	≈ 1.54	127,128
Skin	≈ 1.39	129,130
Dermis	≈ 1.40 – 1.50	131–134
Epidermis	≈ 1.34 – 1.56	131–134
Stratum corneum	≈ 1.50 – 1.55	119,134
Brain	≈ 1.36 – 1.40	135–137
Muscle	≈ 1.36 – 1.38	138–140
Adipose tissue	≈ 1.44 – 1.47	131,134,141,142
Kidney	≈ 1.42 – 1.52	142–144
Refractive indices of cellular components		
Cell membrane	≈ 1.46 – 1.60	145–147
Cytoplasm	≈ 1.35 – 1.39	148–151
Nucleus	≈ 1.34 – 1.37	151,152
Nucleolus	≈ 1.37 – 1.39	149,153,154
Mitochondria	≈ 1.40 – 1.42	153,155,156
Lysosomes	≈ 1.60	156

1.4 Optical tissue clearing

With modern microscopy and improved imaging techniques on the rise, the goal to obtain 3D information from biological tissues has been a long-standing challenge in biomedical research. As explained in the previous chapter, in confocal microscopy, the accessible imaging depth is limited by the effects of light scattering, absorption, and fluorescent background signal caused by inherently fluorescent molecules. Therefore, to obtain images with high resolution, these effects need to be minimized by reducing the lateral scattering of light. Typically, clear confocal images can be generated until depths of approx. 50 – 100 μm , depending on the sample and imaging conditions^{114,157}. However, as the imaging depth increases, these effects become more pronounced and can result in significant blurriness and distortion of the images.

Traditional sample preparation methods, such as cryosectioning and block-face imaging, were among the first techniques which have been developed to obtain relevant information from deep within a sample. Cryosectioning is a method which involves freezing the entire sample, subsequently slicing it

in thin sections of 3-20 μm thickness and a transfer of the individual sections onto microscopic glass slides^{38,114,158}. After labelling and image acquisition of each section, the original structure of the sample can then be reconstructed by aligning images of adjacent tissue sections and thereby retrospectively generating a 3D-volumetric image of the specimen. In earlier times the process of aligning individual images was a laborious and time-consuming task that had to be performed manually, owing to the unavailability of computational methods with appropriate algorithms. Despite today's availability of more efficient methods for image alignment, cryosectioning still poses certain challenges. These complications can include factors such as variations in tissue thickness, deformation during cutting, loss of individual sections, and other issues that may affect the accuracy of image alignment^{114,117,157,159}. In addition, certain sample preparation techniques can also introduce image artifacts that further complicate the microscopy of tissue sections. For example, embedding the sample in a matrix to facilitate cryosectioning or subjecting the sample to the freezing process itself can alter the tissue morphology and create artifacts that obscure the true image. These artifacts can include ice crystal formation, tissue distortion, and other anomalies that can interfere with the visualization and analysis of the tissue. As a result, it is crucial to carefully evaluate the quality of the acquired images. However, cryosectioning is still a reliable and widely used tool for the analysis of tissue sections, especially in histology and pathology.

Serial block-face imaging, in contrast to traditional cryosectioning, also involves the embedding of intact tissue into a matrix such as resin^{114,160,161}. However, instead of sectioning the sample prior to imaging, the top layer of the sample is initially imaged with a microscope, and then removed with an attached ultramicrotome. This process is repeated sequentially, with each removed section revealing the underlying layer of the sample for subsequent imaging. The result is a series of closely spaced images that capture the full extent of the tissue, without the tedious work of preparing individual sections and realigning images to create a volumetric representation of the sample. However, with the subsequent removal of tissue layers, the sample is inevitably lost after the imaging process is completed, leaving no possibility for further analysis or experimentation on the same sample.

Another possibility to gain information on a 3D-sample without the aforementioned pitfalls, is the elimination of the cause of (lateral) scattering by rendering the amount and species of scatterers as homogeneous as possible and reducing RI mismatches. The methods to achieve this goal are summarized under the term "Optical Tissue Clearing" (OTC) and it includes various chemical techniques to homogenize the RI across the tissue, while preserving the inhomogeneous distribution of the individual tissue components¹⁶². For *ex situ* OTC protocols, the major steps to achieve tissue transparency are (a) fixation, (b) permeabilization, (c) decolorization/ delipidation, and (d) RI matching¹⁶³. However, the individual chemicals which are used for each of these steps differ amongst techniques. In 2016, Silvestri et al. (2016) made an effort to bring order to the existing methods by defining a taxonomy of OTC protocols comprised of four major categories, namely, organic solvent-based techniques, high-refractive index aqueous solutions, hyperhydrating solutions, and tissue

transformation.¹¹⁷ Through this meticulous categorization, Silvestri et al. succeeded in simplifying the classification process by assigning the majority of the then-existing techniques to one of the four identified categories, facilitating a more organized understanding of OTC protocols. The fact that only a mere three years later, Matryba et al. (2019) released a revised version of the taxonomy, which not only included over twenty novel techniques but also expanded upon the initial version, only highlights the significance and importance of this field (Figure 1-7)¹⁵⁷.

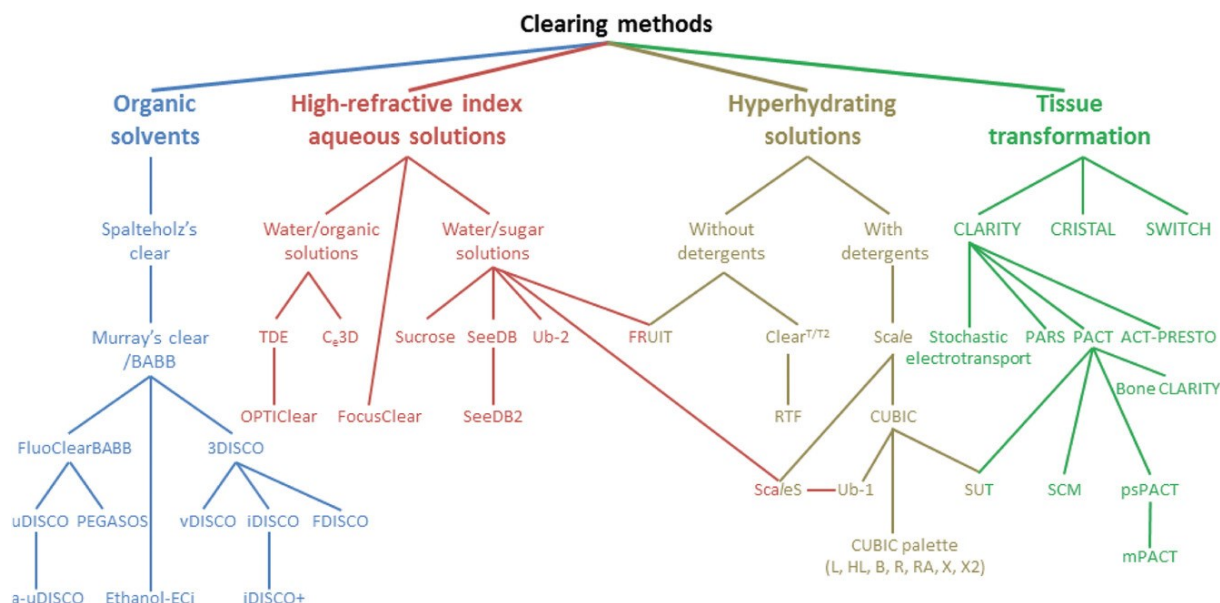


Figure 1-7: Taxonomy of optical tissue clearing protocols. Taken from Matryba et al. (2019)¹⁵⁷ (rights obtained for use)

1.4.1 Organic solvent-based techniques

Optical clearing procedures that utilize organic solvents typically rely on a gradient of alcohol solutions, where the tissue is dehydrated through sequential immersion in solutions of increasing alcohol concentration. This stepwise dehydration process serves the purpose of effectively reducing the water content of the sample. Subsequently, the dehydrated tissue is immersed in a high refractive index solution, such as a mixture of methyl salicylate, benzyl benzoate and wintergreen oil ($n \approx 1.50$). The latter is part of a protocol, which was first proposed by Werner Spalteholz in 1914, today known as Spalteholz's clear or methyl-salicylate and benzyl benzoate (MSBB), and is one of the earliest scientific publications in the field of tissue clearing^{164,165}. In addition to dehydration and RI matching, Spalteholz applied a bleaching step with hydrogen peroxide in order to eliminate light absorption caused by endogenous pigments. Although developed more than a hundred years ago, this method of optical tissue clearing was still applied until the end of the 20th century. However, with microscopy and fluorescent imaging becoming more and more advanced, the demand for new, more efficient methods rose. In the late 1980s, Andrew Murray developed a slightly modified version of the Spalteholz's clear by replacing methyl-salicylate with benzyl alcohol and exchanging methanol with ethanol for tissue dehydration^{166,167}. This method, termed Murray's clear or benzyl alcohol and benzyl benzoate (BABB), laid the foundation for the large majority of organic solvent-based clearing techniques following in its

footsteps. Although the performance of BABB was superior to the original Spalteholz's clear, a major drawback of both methods was still a rapid quenching of fluorescent molecules, and limited clearing capacity in lipid-rich tissue¹⁶⁸. In an attempt to overcome these obstacles, modified versions of BABB clearing have been developed, which make use of different organic solvents, such as dibenzyl ether (DBE), tetrahydrofuran (THF), polyethylene glycol (PEG) or *tert*-butanol^{157,169–171}. Regarding the compatibility of organic solvent-based clearing and endogenously expressed fluorescent proteins, major improvements could be achieved by maintaining a stable pH of 9.5 throughout the clearing process. This highlights that clearing efficiency is not only dependent on the type of chemicals, but also on environmental factors¹⁷¹. A special emphasis should be placed on the method “3D imaging of solvent-cleared organs”, or short 3DISCO, developed by Ertürk et al. in 2012, as it holds significant importance in the history of OTC protocols. By employing a combination of THF for dehydration, dichloromethane (DCM) for delipidation, and subsequent RI matching with DBE, the 3DISCO technique enables remarkable optical transparency in even large tissue samples, encompassing entire mouse organs and human embryos. This method exhibits a remarkable clearing capacity, enabling imaging depths exceeding 1000 μm . Notably, it remains fully compatible with endogenously expressed fluorescent molecules, an array of antibodies, and diverse fluorescent dyes^{170,172,173}. However, it is important to acknowledge that due to the use of harsh and toxic chemicals during sample processing and imaging, long-term storage of samples is precluded by potential tissue degradation. For the same reason, imaging should be done with great caution to prevent potential harm to objectives and imaging devices. Additionally, the compatibility with fluorescent molecules is transient, with a rapid signal loss occurring within 1-2 days.

Since its initial publication in 2012, numerous modified or extended versions of 3DISCO have emerged, aiming to enhance its performance and broaden its applications, particularly concerning fluorescence preservation and immunolabeling. Among the most significant advancements are iDISCO¹⁷⁴, iDISCO+¹⁷⁵, uDISCO¹⁷⁶, FDISCO¹⁷⁷, and sDISCO¹⁷⁸.

In addition to the aforementioned OTC protocols, nowadays commercially available, ready-to-use clearing agents, such as Visikol or CytoVista, exist^{179,180}. Although the exact mixture of chemicals is still proprietary, the main active components in these reagents are trichloroethanol and/or some of its derivatives, making them fall into the category of organic solvent-based clearing procedures. The major advantage of those chemical cocktails is their ease of use by simple immersion and incubation of samples in the clearing agent. However, their use is restricted to small sample sizes below 1000 μm .

To summarize, organic solvent-based optical clearing methods provide several notable advantages. One of their key strengths is the ability to achieve exceptional tissue transparency and high RIs ($n \approx 1.55 - 1.56$), allowing for enhanced imaging of intricate structures and deeper visualization. Newer methods are compatible with various labeling techniques, endogenously expressed fluorescent molecules, as well as multiple imaging modalities. However, it's important to consider certain limitations. Tissue shrinkage and distortion often occur during the process, potentially altering the

original tissue structure and long-term sample storage is often not feasible due to the use of harsh and toxic chemicals, leading to tissue degradation.

1.4.2 High-refractive index aqueous solutions

Driven by the limitations inherent to conventional organic solvent-based clearing methodologies with regards to the effective retention of fluorescent signals, new OTC protocols have been developed focusing on providing an aqueous environment, which is more suitable for conserving fluorescent proteins and, by eliminating sample dehydration, also tissue architecture over a longer period of time. The majority of these protocols are performed by simple immersion of the sample in an aqueous solution, whose RI is matched to the average RI of the tissue ($n > 1.45$)^{114,115,117}.

One of the earliest studies for identifying suitable compounds for aqueous clearing solutions identified 2,2'-thiodiethanol (TDE) as a promising candidate for a tunable clearing and mounting agent for high resolution microscopy. Due to its water-soluble properties, TDE can be either used as a high-concentrated solution with a high RI ($n = 1.515$), or in a diluted manner to adapt the RI of the solution to either sample or that of the microscopic setup. However, the original publication primarily showed the reduction of local refractive index changes and increased stability of fluorescent signal intensity along the z-axis in 2D-cultured PtK2 cells over a range of $25 \mu\text{m}$ ¹⁸¹. Later on, Aoyagi et al. (2015) confirmed the suitability of TDE as a clearing and mounting agent in $400 \mu\text{m}$ thick sections of mouse brain tissue and additionally showed, that a concentration of 60 % of TDE achieved optimal results regarding imaging depth and preservation of fluorescence signal^{182,183}. Until today, TDE is often used as an additional component in newer clearing protocols.

In parallel with exploring the possibilities of TDE as an OTC agent, highly concentrated sugar solutions were identified as possessing both a high refractive index and good clearing capacity. For example, Tsai et al. showed that gradual incubation of $1400 \mu\text{m}$ thick sections of mouse brain in solutions with increasing concentrations of sucrose was sufficient to visualize immunolabelled neurons throughout the entire sample. Additionally, the group also showed that tissue shrinkage induced by high concentrations of sucrose could be mostly compensated by a pretreatment of the sample with low concentrations of the detergent Triton X-100¹⁸⁴.

Based on the results obtained for sucrose, Ke et al. (2013) explored the clearing capability of various other sugar solutions and found fructose to be a superior candidate for an ideal clearing agent. Based on their results, the group developed “see deep brain” or seeDB, a protocol using a sequential incubation of samples in fructose solutions with increasing concentrations. ($n = 1.48 - 1.49$).¹⁸⁵ Based on seeDB, the same group later on developed seeDB2, a finely tuned protocol for high numerical aperture objective lenses with oil or glycerol immersion. In contrast to seeDB, seeDB2 is based on solutions composed of different concentrations of iohexol, a substance classically used as a contrast agent in X-ray imaging, and saponin¹⁸⁶. Another extension of seeDB termed FRUIT was introduced by Hou et al. (2015) by adding urea at a concentration of 4 M to the fructose solutions¹⁸⁷. With respect to optical tissue clearing,

urea is often deployed in hyperhydrating approaches and its mode of action will be discussed in the following chapter 1.4.3.

Among commercially available clearing agents, FocusClear ($n = 1.45$), akin to its organic solvent-based counterparts CytoVista and Visikol, has garnered significant favor in the field upon its introduction to the market owing to its convenience as a readily employable solution. Although the exact composition is still not entirely available to the public, the main ingredients listed in the patent are dimethyl sulfoxide (DMSO), diatrizoate acid, ethylenediaminetetraacetic acid (EDTA), glucamine, β -nicotinamide adenine dinucleotide phosphate (NADPH), sodium diatrizoate, and derivatives of polyoxyalkalene^{157,188}. However, despite its efficacy in achieving optical transparency and ease-of-use, FocusClear reagents remain quite costly and therefore are of limited usability, especially for larger tissue samples or microscopy techniques, such as light sheet microscopy (LSFM).

Among the large variety of components of all types of optical clearing protocols, it is important to highlight the significance of glycerol. Although most protocols only use it as one component of the overall process, glycerol can exert optical clearing capacity on its own to a certain extent^{189–195}. Due to its hydrophilic properties, glycerol exerts good solubility in water and the capacity to form hydrogen bonds with both, water, and protein residues. Because of this, it can be used for tissue dehydration, acting similar to sucrose or fructose, by causing an efflux of water from the sample and a potential influx of glycerol and other external molecules along the osmotic gradient between the internal and external tissue^{196,197}. Furthermore, it is worth noting that a considerable number of immersion media employed in microscopy are based on glycerol, making it a suitable candidate for achieving congruence between the refractive index of tissues and that of the immersion medium.

However, the major drawback of aqueous high refractive index-based clearing solutions using high concentration of sugars or glycerol, is their high viscosity. This makes overall handling of solutions and sample processing more difficult and RI mismatches can be introduced due to trapped air bubbles and insufficient diffusion of the clearing agent through the sample. In the case of highly concentrated sugar solutions, precipitates can form and, depending on their size, very small samples can float at the air-liquid interface of the solution, causing incomplete immersion and therefore optical clearing.^{114,117,198}. Additionally, since all processes rely on passive diffusion, aqueous high RI-based techniques are more time intensive in comparison to organic solvent-based clearing, sometimes taking up to weeks to complete the clearing process.

1.4.3 Hyperhydration-based techniques

Hyperhydration-based optical clearing is a method that involves controlled tissue hydration, achieved by introducing specific chemicals such as urea or formamide into the clearing process. The clearing capacity of urea was first published by Hama et al. in 2011, who found that a 4 M solution of urea was capable of rendering polyvinylidene fluoride membranes translucent¹⁹⁴. In an attempt to optimize this process for biological tissue, the group developed *Scale*, a set of clearing solutions based on 4 M urea,

glycerol to counteract the volume expansion induced by urea, and 0.1 % Triton X-100 as a detergent for delipidation and tissue permeability. Although the exact mechanism is still not entirely clear, urea is thought to act as a weak denaturant and relaxant to protein scaffolds, while also increasing the membrane fluidity to enhance molecular flux and thereby reducing the overall refractive index to ~ 1.38 ^{114,194,199}. By applying *Scale* to sections, entire mouse brain and embryos, remarkable transparency could be achieved, alongside preservation of antibody-coupled fluorophores and expressed fluorescent proteins. However, due to urea-induced hyperhydration, an average sample expansion of approx. 28 % could be observed and the passive diffusion-driven process of *Scale* clearing for whole brain lasted for two weeks. In an attempt to compensate for the volume expansion of samples, the same group later developed *ScaleS*, a protocol based on five solutions of varying amounts of sorbitol, glycerol, urea, Triton X-100 and DMSO ($n = 1.334 - 1.439$).¹⁹³ This new refined method showed only transient expansion of tissue during the clearing process, which did not affect the overall tissue architecture, membrane ultrastructure or signal intensity of fluorescent proteins¹⁹³.

Seeking to find alternative reagents for optical clearing, the same group initiated an extensive screening of polyhydric alcohols, detergents and urea-like chemicals and found the amino alcohol N,N,N',N'-Tetrakis(2-hydroxypropyl)ethylenediamine, or Quadrol, to be highly effective²⁰⁰. Besides being able to decolorize tissue by hemoglobin or myoglobin removal, it is thought to exert delipidating function by solvating anionic phospholipids^{196,201,202}. Based on their findings, the group developed CUBIC (*clear, unobstructed brain imaging cocktails and computational analysis*, $n = 1.48$), which used high concentrations of Quadrol and Triton X-100 to achieve remarkable transparency in whole mouse brains. However, such high amounts of amino alcohols or detergents may be detrimental concerning protein denaturation and loss of antibody epitopes, as well as preservation of fluorescence and overall protein loss¹¹⁴.

Lastly, as an alternative to urea as a hyperhydrating agent, Kuwajima et al. (2013) introduced the two procedures termed *Clear^T* and *Clear^{T2}* ($n = 1.44$), which both are based on gradients of the small amide formamide²⁰³. It exhibits properties similar to urea and additionally has low delipidating capabilities^{196,204}. In contrast to *Clear^T*, which consists of an increasing gradient of formamide solutions, *Clear^{T2}* operates on lower formamide concentrations and includes polyethylene glycol as a hydrophilic component¹⁹⁸.

To summarize, hyperhydration-based clearing protocols provide a good alternative to methods involving organic solvents or simple immersion in aqueous solutions with high refractive indices. They involve incubation of samples in a series of solutions, often with increasing concentrations of the active clearing components and therefore often take longer times compared to protocols using organic solvents or simple immersion. For lipid-rich tissues, techniques including detergents, such as Triton X-100 or Quadrol, can be applied to increase transparency of the samples. Protocols operating in an aqueous environment are compatible with expressed fluorescent proteins and antibodies, however, the hyperhydrating character of these methods is often accompanied by an expansion of the sample volume.

This effect is not necessarily disadvantageous, for example as seen in expansion microscopy, but can come with distortion of the original tissue structures. Also, tissue expansion is closely associated with increased imaging time and data size of the resulting image volumes.

1.4.4 Tissue transformation

Major drawbacks of the previously discussed clearing methods involve loss of fluorescent signal (organic solvent-based techniques), restriction to small samples due to relying on simple immersion and passive diffusion (aqueous high refractive index-based protocols) and long incubation times (weeks to months), high protein loss and fluorophore quenching due to extremely high concentration of detergents (hyperhydrating solutions). Tissue transformation techniques, often also called hydrogel embedding methods, have been developed to overcome these obstacles. The revolutionary method “Clear Lipid-exchanged Acrylamide-hybridized Rigid imaging, Immunostaining, in-situ-hybridization-compatible Tissue hYdrogel, or CLARITY (n = 1.457) for short, was introduced by Chung et al. in 2013¹⁹⁵. The major difference to clearing protocols from other categories involves crosslinking of the samples in an acrylamide/ bis-acrylamide hydrogel before further sample processing and thereby creating a tissue-hydrogel-hybrid. The resulting rigid mesh structure stabilizes tissue architecture and biomolecules to prevent their loss during further sample processing¹⁵⁷. Most importantly, lipids and other molecules lacking functional groups necessary for crosslinking are excluded from the mesh structure and can be effectively removed from the sample. Delipidation of samples is initiated by applying an electrical field inside a custom build electrophoresis chamber for electrophoretic tissue clearing (ETC) with a continuous flow of 8 % sodium dodecyl sulfate (SDS)^{195,205,206}. Similar results can be obtained by simple immersion of the sample in SDS, however, the process takes considerably more time (PASSive Clarity Technique, PACT)^{207,208}. Nowadays a large palette of clearing techniques, such as PARS, ACT-PRESTO, SHIELD, FACT, CLARITY2, or SWITCH, which are ultimately based on the original CLARITY protocol, can be found in literature^{159,208–212}. In comparison to other clearing procedures, e.g., Sca/e or CUBIC, CLARITY shows considerably less protein loss (Sca/e: 41 % vs. CLARITY: 8 %) ²¹³, however, the high concentrations of SDS can also be the cause of extensive protein denaturation, which can potentially destroy binding sites for fluorescent labeling¹⁸⁹. Additionally, active CLARITY requires a specialized ETC chamber, which requires additional investment and technical training, and can lead to tissue deformation due to the high applied currents²¹³.

Lastly, one tissue transformation technique which should be briefly mentioned, is “system-wide control of interaction time and kinetics of chemicals” (SWITCH), published by Murray et al. in 2015²¹². Instead of acrylamide/ bis-acrylamide, SWITCH uses glutaraldehyde (GA) for hydrogel embedding. Furthermore, the protocol uses pH- and temperature-dependent processes and two major solutions, SWITCH-off and SWITCH-on. The former prevents molecules and antibodies from binding to the tissue and allows their free diffusion through the sample¹⁵⁷. Subsequently incubation of samples in SWITCH-on solution returns the tissue to its reactive state, allowing already penetrated antibodies and molecules

to bind¹⁵⁷. The uniqueness of this protocol lies within the repeatability of this process. Alternating between SWITCH-off and SWITCH-on enables multiple rounds of fluorescent labeling and thereby allows to gain extensively more information from a single sample^{157,212}.

1.5 Optical clearing of 3D-cell culture models

With the advent of 3D-cell culture models and modern imaging techniques, it seems surprising that it took an extended period of time for optical clearing techniques to spill over from tissue applications to the realm of *in vitro* systems. Despite the existence of suitable clearing methods with a solid foundation, the majority of microscopy-based investigations of 3D cell cultures relied on either imaging of only superficial layers or using conventional approaches, such as cryosectioning. One of the first studies implementing optical clearing of 3D-cell cultures was proposed by Timmins and Nielsen in 2007³⁰. They published a protocol for the generation of MCTs using the hanging drop method and applying 80% glycerol to immunolabelled spheroids for whole mount confocal microscopy. However, it seemed like the topic of OTC subsequently almost vanished from the field of 3D-cell culture models.

In this chapter, the most important studies on 3D-cell cultures using OTC are summarized according to the classification presented in chapter 0, namely organic solvent-based techniques, aqueous high refractive index solution, hyperhydrating protocols and tissue transformation techniques.

Organic solvent-based optical clearing

Among all available clearing techniques, organic solvent-based methods were among the first ones to be implemented into the analytical workflow of 3D-cell culture models. Wenzel et al. (2014) applied BABB clearing to approx. 400 μm large MCTs of T47D breast cancer cells, labelled with the nuclear dye Hoechst33342 and SytoxGreen for the visualization of dead cells²¹⁴. By using BABB in combination with LSM, the group was able to visualize the necrotic core of spheroids as indicated by a positive SytoxGreen staining in the center²¹⁴. However, the impact of BABB clearing on the staining quality and sample integrity were not addressed. The former was partially addressed in an extensive analytical approach by the group of Ernst Stelzer, a pioneer in the field of optical clearing of 3D-cell culture models and LSM microscopy²¹⁴⁻²¹⁶. They analyzed the impact of different fixation and permeabilization reagents on the staining quality in BABB-cleared U343 spheroids of approx. 600 μm size²¹⁵. The outcome of this systematic study was an optimized immunofluorescent staining protocol for spheroids, which consisted of (1) fixation at room temperature (RT) with 4 % paraformaldehyde (PFA), (2) detergent-based permeabilization using Triton X-100 at RT, (3) blocking of unspecific binding sites by a combination of bovine serum albumin (BSA), serum and low concentrations of detergents, (4) incubation of primary antibody at 37 °C for 18-24 h, (5) secondary antibody incubation for only 4 h at 37°C, and lastly (5) dehydration and clearing of the sample with BABB^{116,215}. Based on their results, the group presented their work on a topic which still proves challenging today: the transfer from qualitative 3D image data to quantitative results²¹⁶. Schmitz et al. (2017) published a pipeline on nuclear

segmentation of BABB-cleared T47D spheroids based on a 3D seeded watershed algorithm, which enabled quantification of nuclei and their morphology through the entire sample²¹⁶.

Desmaison et al. (2018) used a similar approach for large HCT116 cancer spheroids (~ 650 μm), which were cultivated either free floating or physically confined by embedding MCTs in agarose. Their results revealed an improved imaging depth mediated by BABB clearing and differences in nuclear morphology and cell division between the two cultivation methods^{116,217}.

Although most studies using BABB clearing in 3D-culture models focused on MTCs, the method has also been successfully used to clear organoids^{218,219}. Other organic solvent-based clearing protocols, which have been successfully applied to spheroids and/or organoids are ECI, which is based on ethyl cinnamate, and iDISCO^{220–223}.

Aqueous high refractive index-based optical clearing

Simple immersion techniques using water-miscible reagents for RI matching are of great interest regarding the optical clearing of 3D-cell cultures, due to the straight-forward handling, easy implementation into existing workflows, compatibility with a large variety of antibodies and dyes and tunability to different RIs. Though the high viscosity of clearing solutions makes sample handling tedious, various methods from this category have successfully been transferred and adapted to *in vitro* cell culture models.

For example, immersion of samples in the organic compound TDE has successfully been applied to H2B-mCherry expressing tumor spheroids of approx. 300 μm by stepwise immersion in 25 %, 50 %, and 68 % TDE²²⁴. The concentration of TDE in this case was chosen to match the RI of fused silica, which was used to mount samples in a custom-build, integrated optofluidic device for LSFM microscopy. Cleared spheroids were moved through the microfluidic channel and the LSFM at a constant speed of 20 $\mu\text{m s}^{-1}$, thereby enabling the visualization of entire spheroids in a subsequent manner^{116,224}. Lallemand et al. (2020) included TDE in a systematic study comparing optical clearing with TDE, OptiClear, RapiClear and CUBIC in large murine intestinal organoids (~800 μm)²²⁵. After immunofluorescent labeling, samples were incubated in increasing concentrations of TDE and imaged in the final concentration of 80 %. Their results showed significant differences in clearing capacity between methods: while OptiClear and CUBIC led to almost complete quenching of fluorescence, TDE was able to preserve signals of indirectly labelled sucrose isomerase. However, the same could not be observed for the directly labelled phalloidin staining^{116,225}. Additionally, TDE has been used as mounting medium for LSFM microscopy in combination with BABB clearing.²¹⁵

Boutin et al. (2014) explored the capabilities of different optical clearing protocols in different 3D-cultured neural stem cell spheres of only 100 μm diameter¹⁵⁸. Among others, the group tested SeeDB, a representative of highly concentrated sugar solutions and an aqueous high refractive index matching solution. Their results showed a substantial amount of sample shrinkage (~24.7 %) in spheroids cleared with SeeDB. Additionally, although fluorescent labels for nuclei and the neural marker nestin were not affected by SeeDB, the change in sample morphology was accompanied by a low signal-to-noise ratio

(SNR) and almost non-separable nuclei¹⁵⁸. Furthermore, a high amount of sample loss and difficulties in imaging due to sample floating was reported, which was attributed to the high viscosity of fructose solutions used in SeeDB¹⁵⁸. In contrast to the results of Boutin et al. (2014), Grist et al. (2016) adapted SeeDB successfully to an on-chip application for clearing of microtissues in the form of MCF-7 breast cancer cells ($\sim 370 \mu\text{m}$)^{158,226}.

Due to its good solubility in water, RI tunability and lack of reactivity with lenses and objective components, many immersion media in microscopy are based on glycerol. Therefore, similarly to TDE, it has also been used as a sample immersion solution for refractive index matching¹⁹⁵. However, when used as a standalone clearing agent, its pronounced high viscosity and restricted clearing capacity in larger tissues bring its limitations to the forefront. Nonetheless, with 3D-cell cultures often being considerably smaller than their tissue counterparts, glycerol as a refractive index matching solution should still be considered. This was shown by Timmins and Nielsen (2007) in one of the earliest publications applying optical clearing with 80% glycerol to MCTs³⁰. Supporting these findings are studies on clearing of 3D-cell cultures using the commercially available reagent RapiClear, which can be purchased already adapted to a range of RIs. Although the exact composition is still proprietary, one of its major component is glycerol²²⁷. In fact, clearing experiments performed by Steinberg et al. (2020) on three different types of pancreatic cancer spheroids showed comparable clearing efficiency of RapiClear, 100 % glycerol and 85% glycerol, where imaging depths of $\sim 200 \mu\text{m}$ could be achieved²²⁸. Due to the high viscosity of pure glycerol and the higher cost for RapiClear, the group deemed 85 % glycerol as an optimal clearing reagent. Good results for optical clearing with RapiClear ($n = 1.47$), which is closest to the RI of pure glycerol ($n = 1.473$), could also be obtained for murine intestinal organoids and induced pluripotent stem cell (iPSC)-derived neural spheroids^{225,229}.

Hyperhydration-based optical clearing

In addition to being conducted in a watery environment, which enhances its compatibility with a wide range of antibodies and fluorescent dyes, optical clearing protocols based on hyperhydration utilize extra delipidation to enhance optical transparency even more. With lipids being one major source of RI mismatches, delipidation can improve transparency and therefore imaging depth extensively, especially in lipid-rich tissue.

One particular method, which has been used in several studies on 3D-cell culture models, is Clear^T or Clear^{T2}²⁰³. The same comparative study by Boutin et al. (2014), which explored SeeDB as a potential candidate for optical clearing of neural stem cell spheres, applied Clear^{T2} and *Scale*, which are also part of hyperhydrating clearing techniques¹⁵⁸. Interestingly, both protocols achieved comparable results regarding sample transparency and preservation of fluorescent molecules. However, *Scale* induced significant sample swelling by $\sim 35.8\%$. Reasoning that the goal of the study was to determine a clearing protocol which induces no or minimal changes in sample morphology, Clear^{T2} was deemed to be superior technique and later on applied in further studies^{158,230,231}. Comparable results could be obtained in a study by Kabadi et al. (2015) in microtissues generated from human lung epithelial cells, human

prostate adenocarcinoma cells and hepatocytes²³². The protocol of Clear^{T2} for use in multicellular spheroids was later optimized by Costa et al. (2018) by analyzing the influence of PEG molecular weight (MW) on the clearing efficiency²³³. Their analysis of exchanging 8000 kDa PEG, as used in the original protocol, with either 4000 kDa or 10000 kDa PEG, showed a slight improvement of imaging depth and fluorescence preservation in spheroids of human dermal fibroblasts, if PEG with a MW of 4000 kDa was used.^{203,233}

Clear^T, which uses significantly higher concentrations of formamide and no PEG, has also been applied to human dermal fibroblast spheroids. Although an increase in imaging depth and fluorescence intensity of propidium iodide could be observed in cleared spheroids, the authors did not address the decrease in SNR, which was evident in confocal images²³⁴.

Lastly, the hyperhydrating clearing technique CUBIC, which originally belongs to the *Scale* family of clearing protocols, has been applied in the study by Lallemand et al. (2020) in murine intestinal organoids²²⁵. As previously described, CUBIC was used alongside RapiClear and TDE, to analyze clearing efficiency. Although CUBIC clearing increased sample transparency comparably to other tested methods, the fluorescence signal of tested antibodies was thoroughly quenched, and therefore, this method was not considered suitable for immunofluorescence. Contrary to those results, Castellanos-Montiel et al. (2023) recently published their results on an optimized protocol for the generation of iPSC-derived motor neuron spheroids (~260 – 325 μm)²³⁵. The group successfully applied CUBIC clearing to spheroids fluorescently labelled with the nuclear dye Hoechs33342 and antibodies for motor neuron marker proteins Hb9, Isl1, and NF-H.

Tissue transformation techniques

Among the large variety of tissue clearing protocols, tissue transformation techniques are certainly among the most refined methods. The creation of a tissue-hydrogel hybrid and replacement of lipid bilayer membranes with a stable crosslinked mesh enables remarkable tissue transparency and high penetration of dyes and antibodies throughout the sample^{205–207,210}. However, the harsh conditions under high SDS concentrations and applied currents in ETC can be destructive, even to tissues like muscle¹⁸⁹. Since 3D-cell culture samples are usually less durable than native tissue, it is no surprise that tissue transformation techniques have rarely been applied in this field. Furthermore, the small sample sizes can make handling during this technique an exceptionally high challenge.

Nevertheless, a few studies using CLARITY for on-chip clearing in microfluidic chambers exist. Chen et al. (2016) developed a “spiraling” microfluidic chamber in which spheroids of varying sizes (250 – 450 μm) were loaded and trapped inside cavities along the flow channel²³⁶. By perfusing the chamber with an acrylamide/ formaldehyde solution and subsequently polymerizing the solution at 37 °C, sample-hydrogel-hybrids were formed. Once polymerized, the chamber was flushed with a 4 % or 8 % SDS solution to remove lipids and other scatterers, followed by perfusion with fluorescent dyes and antibodies. Finally, RI matching was carried out by perfusion with refractive index matching solution (RIMS). This modified version of CLARITY enabled imaging of entire spheroids of different

entities to gain high quality images suitable for quantitative segmentation in a high-throughput manner in an extremely short timeframe compared to the original protocol²³⁶. Similarly, Santisteban et al. (2017) developed a microfluidic chip where CLARITY was applied to clear and label spheroids of human adipose-derived stem cells (hASCs), where the total amount of time taken to carry out the protocol was reduced from 14 days to just 5 h²³⁷. Although solutions used in those studies were also applied in the original CLARITY technique, incubation of samples in an electrophoretic chamber is not applied, therefore they should be considered as PACT protocols. Aside from microfluidic chips, PACT has also been applied for clearing and whole mount imaging of intact iPSC-derived retinal organoids²³⁸.

Newer techniques, such as SWITCH or SHIELD have mainly been applied to iPSC-derived organoids^{239,240}. Especially the former, which was used by Renner et al. (2017) to track developmental patterning and differentiation in cerebral organoids, highlighted the reasoning behind the importance of whole mount image data²³⁹. By applying SWITCH clearing to organoid samples, the group was able to show that ventricular areas inside the samples, which were previously thought to be small, isolated regions, were in fact a large network-like structure spanning large areas throughout the sample.

Taking everything into consideration, although numerous OTC protocols have been applied to various 3D-cell culture models, ranging from small MTCs to large cerebral organoids, there does not seem to be a gold standard for optical clearing of 3D *in vitro* systems^{116,241}. This is not surprising, since the same can be observed for tissues of different origins²⁴²⁻²⁴⁴. However, studies on the variability between clearing protocols in different *in vitro* systems are rare. In fact, to my knowledge, only one comparative study exists, which focused on the variability of OTC techniques between different 3D-cell culture models. Diosdi et al. (2021) applied five aqueous high-refractive index-based and hyperhydrating methods (Clear^T, Clear^{T2}, CUBIC, ScaleA2 and sucrose) to three different types of cancer spheroids (T-47D, 5-8F and Huh-7D12) of a similar size of $\sim 250 \mu\text{m}$ ^{245,246}. Following optical clearing, samples were stained with the nuclear dye DRAQ5 and visualized with CLSM. Their results showed that none of the protocols affected fluorophore preservation, though differences in image quality between OTC methods and cell lines were evident. In T-47D spheroids, the obtained outcomes exhibited a high degree of comparability across all employed protocols, nonetheless, subtle distinctions emerged wherein Sucrose, CUBIC, and ScaleA2 demonstrated a slightly enhanced efficacy. In 5-8F spheroids, Clear^T and Clear^{T2} did not improve imaging depth or image quality compared to uncleared controls. For Huh-7D12 samples, only sucrose clearing was able to visualize distinguishable nuclei throughout the sample^{245,246}. However, the study did not address sample preservation, compatibility with fluorescent proteins or labeled antibodies, or suitability for image segmentation algorithms. In general, more in depth analyses are needed for the evaluation of suitable OTC protocols in different 3D-cell culture models.

1.6 Aims of this study

In recent years, the field of cell biology and biomedical research has seen a significant shift towards 3D-cell culture models. These models provide a more faithful representation of complex 3D microenvironments compared to traditional 2D cultures, offering valuable insights into cellular behavior. One promising application is the neural differentiation of human induced pluripotent stem cells (hiPSCs), which can form brain organoids closely resembling fetal brain development. However, 3D-hiPSC cultures are associated with challenges, including cost, time, and batch-to-batch variability. To address these challenges, stable hiPSC-derived neural precursor cells (NPCs) have been proposed as a more cost-effective and consistent alternative, despite their limited differentiation potential. However, 3D-cultivation of these NPCs remains relatively unexplored.

Additionally, microscopy in 3D-cell culture models presents challenges such as light scattering within dense samples. OTC techniques aim to mitigate this issue by homogenizing the refractive index across the specimen. While OTC has been applied to 3D-cell cultures in some studies, variations in clearing methods, particularly among different cell lines within a single protocol, remain relatively uninvestigated.

Therefore, this thesis aims to achieve three major objectives:

- (i) Development and characterization of a 3D-spheroid model using hiPSC-derived NPCs capable of differentiating into a diverse population of neural cells.
- (ii) Establishment of an effective optical clearing protocol from multiple available procedures, enabling the analysis of these spheroids in a 3D context.
- (iii) Apply selected OTC methods to various 3D-cell culture models with varying complexities to gain insight into methodological variations and differences across cell lines.

2 Material and Methods

2.1 Cell culture

2.1.1 Cell Lines

For this study, a total of seven different non-malignant and malignant cell lines of different origin were used. The non-malignant cell lines were comprised of the human iPSC (hiPSC)-derived neural precursor cell (NPC) line B7_033#1NPC1 (kindly provided by Sandra Horschitz, Hector Institute for Translational Brain Research, Central Institute of Mental Health, Mannheim, Germany), human fibroblast cell line CCD-1137SK (ATCC), the human keratinocyte cell line HaCaT and the human taste bud-derived cell line HTC8 (both kindly provided by B.R.A.I.N. AG, Zwingenberg, Germany). Malignant cell lines were comprised of human colorectal adenocarcinoma-derived HT29 cells, triple-negative breast cancer cells MDA-MB231 and the human melanoma cell line SK-MEL-28 (all ATCC).

2.1.2 Cell culture methods and spheroid generation

All cell lines were cultured under standard conditions at 37 °C at 5 % CO₂ fumigation in a humidified cell culture incubator. For all experiments, cells were handled under sterile, aseptic conditions in a biosafety class II cabinet and maintained in their respective culture medium until reaching a confluency of 80%, with medium change every other day. All cell lines were repeatedly authenticated by phenotypic analysis and regularly tested for mycoplasma. A complete list of cell culture materials, including suppliers, catalogue, and lot numbers, can be found in Appendix 8.1.

For the generation of mono- and tri-culture spheroids, a cell line-dependent number of cells was seeded onto ultra-low attachment (ULA) 96-well U-bottom plates in their respective medium and centrifuged at 300 xg for 5 min. All cells were maintained in a humidified incubator at 37 °C and 5 % CO₂ fumigation. For the investigation of optical clearing protocols, all spheroids, with the exception of a melanoma tri-culture model, were kept in culture until reaching a diameter of approximately 300 µm. A summary of all cell lines, including their type of origin, if present specific labeling, and cell number used for experiments on optical tissue clearing, is presented in Table 2-1^{i,ii}.

ⁱ Contribution from Elena von Molitor, Julia Klicks, Mario Vitacolonna and Tiziana Cesetti, see Table 8-10: Contributions from other persons, p. 117

ⁱⁱ Contribution from Samira Maxhuni, see Table 8-10: Contributions from other persons, p. 117

Table 2-1: Overview of cell lines used in this study, including cell type, fluorescent labeling, and cell number used for sample generation. Adapted from Nürnberg et al. (2020)²⁴⁷.

	Cell line	Cell type	Labeling	Cell number
Mono-cultures	B7_033#1NPC1	iPSC-derived neural precursor	-	1x10 ⁵
	HaCaT	Keratinocyte	-	9x10 ³
	CCD-1137SK	Fibroblast	-	1x10 ⁴
	HT29	Colorectal adenocarcinoma	-	1x10 ³
	HTC-8	Human taste bud	-	6x10 ³
Dynarray co-culture	MDA-MB231	Triple-negative breast cancer	ECFP	2x10 ⁶
	CCD-1137SK	Fibroblast	CellTracker Red	2x10 ⁶
Melanoma tri-culture	HaCaT	Keratinocyte	CellTracker Red	1x10 ⁴
	SK-MEL-28	Melanoma	CellTracker Green	ATCC
	CCD-1137SK	Fibroblast	-	1x10 ⁴

B7_033#1NPC1

The hiPSC-derived B7_033#1 NPC1 line was cultured on poly-L-ornithine (PLO)-coated culture dishes. Briefly, PLO solution was diluted in sterile 1x phosphate-buffered saline (PBS) in a concentration of 150 μ L PLO/ mL PBS, mixed and transferred onto 10 cm culture dishes. After even distribution, plates needed to be incubated at 37 °C for at least 2 hours or alternatively overnight (o.n.) at RT. After incubation, plates were washed three times with 1xPBS and were ready for use. When covered with PBS, plates could be stored at RT under the laminar flow for 1 week.

Cultivation of non-differentiating NPCs was performed according to Nürnberg et al. (2018)²⁴⁸. Briefly, cells were cultured in Dulbecco's Modified Eagle Medium (DMEM)/Ham's F12 + GlutaMAX supplemented with 1% N2 and 2% B27 supplements, 1% GlutaMAX, 1% Minimum Essential Medium Non-Essential Amino Acids (MEM-NEAA), 1% penicillin/streptomycin (Pen/Strep) and 20 ng/mL FGF-2_Type 147. For spheroid generation, cells were detached using TrypLE Express and seeded onto 96-well ULA U-bottom plates. For investigations on the time-dependent spheroid growth, a range of 500 – 16.000 cells per spheroid was seeded. Experiments for the analysis of proliferation, apoptosis, and neural differentiation by immunofluorescent labeling of cryosections and assessment of optical clearing methods, a concentration of 1x10⁴ cells per spheroid was used²⁴⁷. A diameter of ~300 μ m was reached after one to three days of cultivation. For further analyses of differentiating NPCs, spheroids were kept in FGF2-containing medium for two weeks with medium change occurring every other day. After two weeks, FGF2 was withdrawn from cultivation medium to initiate differentiation according to Nürnberg et al (2018)²⁴⁸. A schematic display of the differentiation timeline is shown in Figure 2-1.

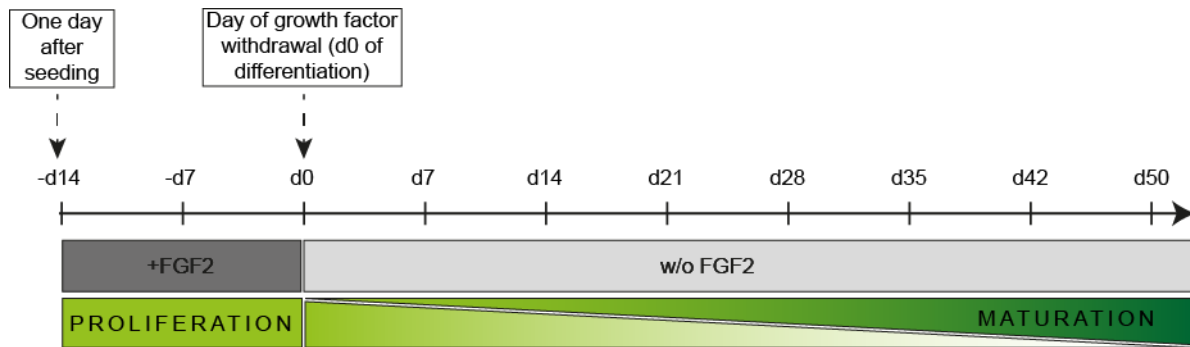


Figure 2-1: Timeline of 3D-differentiation of hiPSC-derived NPCs into neurons and astrocytes. For generation of B7_033#1NPC1 spheroids, undifferentiated NPCs were detached from the culture dish using TrypLE Express and seeded onto ULA U-bottom plates. After centrifugation for 5 min at 300 xg, cells were kept in culture in FGF2-containing medium for 14 days (-d14 – d0), with medium change occurring every other day. Differentiation and maturation were initiated by FGF2-withdrawal from the medium at d0. From then on, cells were kept in culture for 50 additional days.

HaCaT spheroids

The HaCaT human keratinocyte cell line was maintained in DMEM, which was supplemented with 1% Pen/Strep and 10% fetal bovine serum (FBS). Spheroids were generated by detaching cells using Trypsin/EDTA and then seeding 9×10^3 cells per well onto 96-well ULA U-bottom plates. Following a cultivation period of four days, the spheroids attained a diameter of $300 \mu\text{m}^{247}$.

CCD-1137SK spheroids

CCD-1137SK fibroblast cells, derived from human foreskin, were cultured in Iscove's Modified Dulbecco's Medium (IMDM), complemented with 10 % FBS and 1 % Pen/Strep. In order to create spheroids, cells were detached using Trypsin/EDTA and placed onto 96-well ULA U-bottom plates at a density of 1×10^4 cells per well. Following four days of cultivation, the spheroids attained an average diameter of $300 \mu\text{m}^{247}$.

HT29 spheroids

HT29 colon cancer cells were grown in McCoy's 5A medium, enriched with 10% FBS and 1% Pen/Strep. To create spheroids, cells were detached using Trypsin/EDTA and then seeded onto 96-well ULA U-bottom plates at a density of 1×10^3 cells per well. Approximately three days of cultivation reached a diameter of around $300 \mu\text{m}^{247}$.

HTC-8 spheroids

The HTC-8 human tongue cell line was cultured using HTC-medium as described by Hochheimer et al. (2014)^{249,250}. To initiate spheroid formation, cells were detached using Trypsin/EDTA, and a density of 6×10^3 cells per well was seeded onto 96-well ULA U-bottom plates. Following five days of cultivation, the spheroids achieved an average diameter of $300 \mu\text{m}^{247}$.

Melanoma tri-culture spheroids

Melanoma tri-cultures were generated following the method outlined in Klicks et al. (2019)³⁸. In brief, CCD-1137SK cells were initially seeded at a concentration of 1×10^4 cells, followed by the simultaneous

introduction of HaCaT cells (1×10^4 cells/well) and SK-MEL-28 cells (2.5×10^3 cells/well) after three days. To distinguish individual cell types, CellTracker Red CMPTX (10 μ M) and CellTracker Green CMFDA (10 μ M) dyes were used to label HaCaT and SK-MEL-28 cells, respectively, following the manufacturer's instructions for a duration of 30 minutes. The tri-culture spheroids were subsequently maintained in culture for an additional two days²⁴⁷.

2.1.3 Dynarray co-culture model

MDA-MB-231 cells were subjected to stable transfection with the ECFP-C1 plasmid using NucleofectorTM II (Lonza), following the prescribed protocol of the manufacturer. In brief, the ECFP plasmid was linearized through incubation at 10 μ g/ μ L DNA concentration with 10% μ L AseI buffer 3.1 and 5% AseI enzyme for 30 minutes at 37 °C under gentle agitation at 300 rpm. To maintain the construct in its linearized form, DNA was incubated with alkaline phosphatase for 30 minutes at 37 °C. Subsequently, 1×10^6 MDA-MB-231 cells were transfected employing Nucleofector II, using 2 μ g of linearized ECFP.

Co-culture experiments in Dynarrays (300MICRONS) were performed according to the method published by Keller et al. (2020), using MDA-MB-231-ECFP and CCD-1137SK cells²⁵¹. In brief, CCD-1137SK cells were subjected to labeling using CellTracker Red CMPTX in line with the manufacturer's instructions. This process occurred at a concentration of 10 μ M in serum-free medium for a duration of 30 minutes. Preceding the seeding of cells, Dynarrays underwent treatment with a sequential isopropyl alcohol gradient (100 %, 70 %, 50 %, and 30 % alcohol in purified water) for 30 seconds each. After two rounds of washing with purified water, the chips were coated with 30 μ g/mL rat tail collagen 1 in 0.2 % acetic acid for a duration of 1 hour at RT, followed by a single wash using PBS. Subsequently, a mixture of 2×10^6 MDA-MB231-ECFP cells and 2×10^6 CellTracker-labeled CCD-1137SK cells was prepared in 100 μ L of media and seeded onto the Dynarray chips. Following an incubation period of 3 hours at 37 °C in a CO₂ incubator, 10 mL of DMEM were introduced and refreshed every other day over the course of nine days^{247, iii}.

2.2 Immunofluorescence stainings

For all procedures involved in immunofluorescence staining, solutions were prepared under sterile conditions or sterile filtered before usage. Solutions containing proteins, such as FBS or BSA, were prepared freshly prior usage and stored at 4 °C for a maximum of 1 week.

2.2.1 Fixation of spheroids and co-culture models

For all experiments, cultured spheroids were carefully transferred into 200 μ L PCR-tubes. Samples were allowed to settle down by gravity and medium was carefully removed. Subsequently, spheroids were

ⁱⁱⁱ Contribution from Florian Keller, see Table 8-10: Contributions from other persons, p. 117

subjected to a dual wash with 1xPBS at RT, followed by fixation using 4 % PFA for a duration of 1 hour at 37 °C. After fixation, the samples underwent two 5-minute washes at RT, each with 1xPBS containing 1% FBS. Lastly, spheroids underwent quenching with 0.5 M glycine in 1xPBS for 1 hour at 37°C with gentle agitation. If not further processed immediately after fixation, samples were stored in sterile 1xPBS for a maximum of 1 week^{iv}.

2.2.2 Preparation of cryosections and immunofluorescence labeling of spheroid sections

For cryosectioning of spheroids, PFA-fixed samples were subjected to dehydration with sequential incubation in 15 % and 30 % (w/v) sucrose in 1xPBS, each for 24 hours at 4 °C. Prior to sectioning, samples were embedded in OCT, snap frozen on dry ice and stored at -80 °C until further processing. Cryosections of 10 µm thickness were prepared using a CM-1950 cryostat (Leica Biosystems, Nussloch, Germany).

For immunofluorescence labeling, sections were permeabilized with 0.1 % Triton X-100 and 0.1 % (w/v) sodium citrate in 1xPBS for 3 minutes on ice, followed by washing three times with 1xPBS at RT. Subsequently, unspecific antibody binding sites were blocked by incubation in blocking solution made from 3 % (w/v) BSA and 0.2 % gelatin from cold water fish skin in 1xPBS. Primary antibodies were diluted in blocking solution and added to the sample for at least 60 min at RT, followed by three washing steps with fresh blocking solution to remove excess antibodies. Secondary antibodies were diluted in blocking solution, subsequently added to the objective slide, and incubated for 45 min at RT in the dark to prevent fluorophore bleaching. All primary antibodies and fluorescent labels used to analyze cryosections are summarized in Table 2-2. To remove unbound secondary antibodies, cryosections were washed three times with 1xPBS and once with ddH₂O before embedding the samples in Mowiol and sealing the objective slide with a glass coverslip. Objective slides were allowed to dry o.n. at RT in the dark^{iv}. A complete list of materials and consumables can be found in Appendix 8.2.

^{iv} Contribution from Samira Maxhuni, see Table 8-10:

Contributions from other persons, p. 117

Table 2-2: Primary antibodies and fluorescent labels used for immunofluorescence staining of cryosections

Dyes & Antibodies	Dilution	Supplier	Ordering No.	Lot No.
1° Ab α cleaved caspase-3	1:500	Cell Signaling	D175	
1° Ab α GFAP	1:500	Synaptic Systems	173 001	
1° Ab α KI67	1:500	Merck Millipore	AB9260	3195946
1° Ab α -nestin	1:250	Abcam	ab105389	
1° Ab α SOX2	1:500	Synaptic Systems	347 003	347003/1-2
1° Ab α β -III-tubulin (TUBB3)	1:1000	Synaptic Systems	302 304	1-10
2° Ab α mouse-AF 488	1:1000	Invitrogen	A11001	1834337
2° Ab α mouse-AF 555	1:1000	Invitrogen	A21424	2123594
2° Ab α mouse-AF 647	1:1000	Invitrogen	A31571	2045337
2° Ab α rabbit-AF Plus 488	1:1000	Invitrogen	A32790	TI271741
2° Ab α rabbit-AF Plus 647	1:1000	Invitrogen	A32795	TJ271043
DAPI dihydrochloride	1:1000	Sigma-Aldrich	D9542-5MG	28114320

2.2.3 Whole-mount immunofluorescence

Except for the ScaleS clearing protocol, all remaining optical clearing methods encompassed the subsequent steps for immunofluorescence labeling according to Nürnberg et al. (2020)²⁴⁷: following fixation and PFA-quenching, samples underwent a permeabilization phase lasting 5-10 minutes in a 2 % Triton X-100 solution diluted in PBS. Subsequently, samples were incubated for 30-minute at RT in penetration buffer, aimed at enhancing the infiltration of antibodies and nuclear dyes. Afterwards, spheroids underwent two washes in PBS/1 % FBS and were subjected to a 2-hour blocking step in blocking buffer at 37 °C, with gentle agitation. After blocking, the samples were exposed to a primary antibody overnight at 37°C, under gentle shaking. On the next day, primary antibodies were removed by five 5-minute washes in washing buffer, followed by incubation of secondary antibodies and nuclear dyes overnight at 37°C with gentle shaking while safeguarded from light. All antibodies and nuclear dyes were diluted in their corresponding concentrations (Table 2-3) in antibody buffer. After secondary antibody incubation samples were washed subsequently five times for 5 minutes in washing buffer with gentle shaking and then embedded or cleared according to chapter 2.3, protected from light to prevent bleaching of fluorophores. The exact compositions of buffers used for fluorescence whole mount labeling of spheroids are summarized in

Table 2-4²⁴⁷. A complete list of used materials can be found in Appendix 8.2.

Table 2-3: Primary antibodies and fluorescent labels used for whole mount immunofluorescence stainings.

Dyes & Antibodies	Dilution/Concentration	Supplier	Ordering No.	Lot No.
1° Ab α KI67	1:300	Merck Millipore	AB9260	3195946
2° Ab α rabbit-AF Plus 488	1:800	Invitrogen	A32790	TI271741
2° Ab α rabbit-AF Plus 647	1:800	Invitrogen	A32795	TJ271043
DAPI dihydrochloride	1:500	Sigma-Aldrich	D9542-5MG	28114320
DRAQ5 Fluorescent Probe Solution (5 mM)	1:1000	Invitrogen	62252	511DR50200

Table 2-4: Composition of buffers used for whole mount immunofluorescence stainings.

	Chemical	Concentration		Chemical	Concentration
	Triton X-100	0.2%		0.2 %	Tween 20
Penetration buffer	Glycine	0.3 M	Antibody buffer	10 μ g/mL	Heparin
	DMSO	20%		1%	BSA
				5%	DMSO
Blocking buffer	0.2 %	Triton X-100	Washing buffer	0.2 %	Tween 20
	1%	BSA		10 μ g/mL	Heparin
	10%	DMSO		1%	BSA

2.3 Optical clearing

All samples were mounted, if not stated otherwise, 24 hours prior to imaging in ibidi 18 well flat bottom μ -slides. All procedures were executed with minimal exposure to light in order to prevent bleaching of fluorophores. After mounding, samples were always kept in the microscope room for several hours to allow for temperature adjustment prior to image acquisition. A complete list of chemicals used for all clearing methods, including catalogue and lot numbers, can be found in Appendix 8.2. All embedding and clearing methods were carried out according to Nürnberg et al. (2020)²⁴⁷.

2.3.1 Embedding in PBS and Mowiol

For the evaluation of clearing efficiency, samples were embedded in PBS (RI 1.33) and, as a reference for commonly used embedding methods, additionally Mowiol (\sim 1.49)²⁴⁷.

2.3.2 88 % Glycerol

Optical clearing of samples with a RI-matched solution of 88 % glycerol (RI 1.459) was performed according to Williams et al.⁹. Briefly, after immunofluorescent staining, samples were immersed in 88 % glycerol for 24 h with gentle shaking. Prior to imaging, samples were mounted in the same solution in order to minimize variations in RI-matching²⁴⁷.

2.3.3 Clear^{T2}

Optical clearing of 3D-samples by Clear^{T2} was performed according to Dingle et al.²³¹. Briefly, fixed, and stained spheroids were incubated for 10 min at RT in a solution of 25% formamide/10% polyethylene glycol (PEG), followed by a 5 min incubation in a 50% formamide/20% PEG solution. Finally, samples were immersed in fresh 50% formamide/20% PEG (RI 1.44¹¹), incubated for 60 min at RT and subsequently mounted. All steps were carried out under gentle movement²⁴⁷.

2.3.4 CytoVista

For optical clearing with the commercially available agent CytoVista, remaining liquid was carefully removed from samples, followed by ON immersion at RT in 30 μ L of CytoVista Tissue Clearing Reagent (RI 1.50). Subsequently, samples were mounted in the same solution²⁴⁷.

2.3.5 ScaleS

An adapted version of the original ScaleS tissue clearing protocol¹⁹³ for indirect immunofluorescence was used. The exact composition of ScaleS solution is displayed in Table 2-5. After fixation, spheroids were immersed ON in ScaleS0 solution to avoid sample floating in subsequent steps. Permeabilization involved immersion in ScaleA2 for 24 h, followed by a 24 h incubation in ScaleB4(0) and a final incubation in ScaleA2 ON. All permeabilization steps were carried out at 37 °C with gentle movement. Then, samples were washed for 6 h in PBS at RT and subsequently blocked in ScaleS blocking solution for 24 h at 37°C. After blocking, samples were incubated with primary antibody diluted in AbScale solution for 24 h at 37°C, washed two times for 2 h each in fresh AbScale at RT and then incubated ON at 37°C in secondary antibody solution containing nuclear dyes. Next, samples were washed in fresh AbScale for 6 h at RT, followed by reblocking twice for 2 h each in ScaleS blocking solution. After re-fixation in 4% PFA for 1 h at RT, spheroids were washed in PBS ON at 4°C. For RI matching, samples were incubated in ScaleS4 (RI 1.437) solution ON at RT and subsequently mounted. All steps were carried out under gentle movement to ensure proper immersion of samples²⁴⁷.

Table 2-5: Composition of solutions for ScaleS tissue clearing protocols.

	Chemical	Concentration		Chemical	Concentration		
ScaleS0	D-Sorbitol	20 % (w/v)	ScaleS	BSA	2.5 % (w/v)		
	Glycerol	5 % (w/v)		Blocking	Tween-20	0.05 % (w/v)	
	DMSO	3 % (v/v)			Solution	Triton X-	
	in	1xPBS				100	0.1 % (w/v)
	pH	7.2				in	1xPBS
ScaleA2	Glycerol	10 % (w/v)	AbScale			Urea	0.33 M
	Urea	4 M		Triton X-		100	0.1 % (w/v)
	Triton X-				in		
	100	0.1 % (w/v)					
	in	ddH ₂ O					1xPBS
pH	7.7	pH	7.4				
ScaleB4(0)	Urea	8 M	ScaleS4	D-Sorbitol		40 % (w/v)	
	in	ddH ₂ O		Glycerol	10 % (w/v)		
				Urea	4 M		
				DMSO	15 % (v/v)		
	pH	8.4		in	ddH ₂ O		
		pH	8.1				

2.4 Microscopy

All bright field images were acquired by using an Axiovert25 microscope (CarlZeiss Microscopy GmbH).

2.4.1 Confocal microscopy

Acquisition of confocal image stacks was performed with an inverted Leica TCS SP8 DLS confocal microscope (Leica Microsystems CMS, Mannheim), equipped with HC PL APO 20 x/0.75 IMM CORR objective and 405 nm, 488 nm, 561 nm, and 633 nm lasers. Using the Leica Application Suite X software, all image stacks were acquired with comparable settings to ensure comparability. For all clearing methods, Immersion Type F (Leica Microsystems, RI 1.52) was used, and images were taken at a resolution of 1024x1024 pixels, with a z-step size of 1.5 μ m. An initial laser intensity of 1-1.5 % and gain settings between 600 and 750 V were chosen to avoid overexposure of pixels. Image stacks for Figure 3-2 to Figure 3-17 were acquired without z-compensation, whereas data for Figure 3-18 and Figure 3-19 was acquired by using z-compensation with a stepwise linear increase of laser intensity up to a final value between 10-12 %²⁴⁷.

2.4.2 Light sheet microscopy

Images for Figure 3-9 were acquired with an inverted Leica TCS SP8 DLS (Leica Microsystems CMS, Mannheim), equipped with an illumination 1.6x/0.05 DLS objective, a HC APO L 10x/0.30 W DLS detection objective, 7.8 mm TwinFlect mirrors, and 405 nm, 488 nm, 561 nm, and 633 nm lasers. Samples were mounted in small 1.5mm, U-shaped glass capillaries (Hilgenberg) and covered with 0.1 % low melting agarose diluted in ddH₂O. Subsequently, glass capillaries were mounted on a custom-made sample holder designed for 35 mm glass bottom dishes for immersion microscopy (ibidi), and subsequently immobilized with low melting agarose. Following sample mounting, the dish was filled with an 88 % glycerol solution.

2.5 Image processing and analysis

2.5.1 Measurement of spheroid diameter and depth-dependent signal intensity

The average spheroid diameter of each cell line was analyzed before and after PFA-fixation by analyzing bright field images. To assess clearing-induced changes in sample size, maximum z-projections generated by using FIJI image processing software were used. Briefly, the mean size for each sample was determined by measuring the spheroid diameter twice in a perpendicular angle using Fiji's line tool and calculating the arithmetic mean. Depth-dependent signal intensities were measured from confocal z-stacks for each fluorophore by placing a circular region of interest (ROI) with a diameter of 100 μ m in the central region of the sample. The selected area was duplicated from the original image stack and the mean signal intensity for each optical section was measured using FIJI's function to plot z-axis profile^{247, v}.

2.5.2 Depth-dependent signal-to-noise ratio

To assess the quality of confocal image stacks and optical sections in greater depth, an intensity-based approach was employed to ascertain the Signal-to-Noise Ratio (SNR). Isolated image stacks generated for the preceding signal intensity analysis were used to measure the depth-dependent SNR for nuclear stainings. In brief, a median filter (radius 1) was applied to each optical section from the central region of each spheroid and a manual threshold range was then defined for the upper regions of the sample, encompassing the areas designated as background. These areas were transformed into binary masks, which were subsequently passed on to FIJI's ROI Manager. These generated ROIs were used to automatically compute the mean background intensity and its corresponding standard deviation for each region within its respective optical section. For the evaluation of signal intensity from nuclear dyes, an automated thresholding algorithm was applied independently to each optical section. Similarly, this

^v Contribution from Roman Bruch, see Table 8-10: Contributions from other persons, p. 117

algorithm was employed to quantify the signal intensity within nuclear regions. The average SNR was computed for each optical section and can be defined as:

$$SNR = \frac{\mu_{SIG\!N\!A\!L}}{\sigma_{background}}$$

Here, ' μ ' represents the mean signal intensity within a single optical section, while ' σ ' represents the corresponding standard deviation of the background intensity^{247,vi}.

2.5.3 3D-Segmentation of nuclei

For 3D-segmentation of confocal image stacks, pre-processing was done using FIJI. Briefly, images were cropped to reduce data size, following splitting of multichannel image stacks into single channels for individual segmentation of nuclear dye signal and immunofluorescent stainings. Subsequent background correction, conversion into 8-bit format and export into .tiff file format was performed. For segmentation a previously published algorithm based on 3D-seeded watershed, which is implemented into Mathematica (Wolfram Research Inc.) and equipped with a graphical user interface (GUI), was applied²¹⁶. Applied parameters included a median filter range of 3 pixels, a local threshold of 10 pixels, and a hole filling range of 1 pixel. A Laplace of Gaussian (LoG) filter was applied for seed detection with a range between 9 and 25 pixels, depending on the individual cell line. Other parameters were applied as default and segmented data was exported as 3D-stacks in .tiff format and quantitative results in tabular form^{247vii}.

2.5.4 Statistical analysis

Statistical analysis was performed using GraphPad Prism 8 (GraphPad Software Inc.). All data sets were tested for normal distribution by Kolmogorov-Smirnov test. Statistics for spheroid size measurements were generated by non-parametric Kruskal-Wallis with Dunn's multiple comparisons test. Segmentation results were analyzed by one-way ANOVA with Tukey's multiple comparisons test. To compare segmentation results obtained for samples imaged with and without z-compensation, an unpaired, non-parametric Mann-Whitney t-test was used. Significance level α was set to 0.05 with 95 % confidence interval and p-values were adjusted to account for multiple comparisons²⁴⁷.

^{vi} Contribution from Roman Bruch, see Table 8-10: Contributions from other persons, p. 117

^{vii} Contribution from Mario Vitacolonna, see Table 8-10: Contributions from other persons, p. 117

3 Results

3.1 hiPSC-derived neural spheroids for exploring OTC protocols in 3D-cell cultures.

3.1.1 Proliferation of hiPSC-derived neural spheroids is decreased upon FGF2-withdrawal

As an initial step in assessing OTC protocols suitable for 3D in-vitro systems, it was essential to choose a suitable model. The stable cell line B7_033#1NPC1, derived from hiPSCs, was chosen for initial experiments, building upon the prior demonstration of these cells' capabilities to differentiate into functional human neurons and astrocytes in a 2D environment^{248,252}. These experiments aimed to assess the cell line's capacity for scaffold-free cultivation as spheroids and its potential for differentiation into a mixture of various neuronal subtypes and astrocytes. Therefore, undifferentiated B7_33#1NPC cultured on PLO-coated, adherent culture dishes were detached from the plate and seeded in different concentrations, ranging from 5×10^3 to 1.6×10^5 , onto ULA U-bottom plates in FGF2-containing medium to suppress differentiation. After centrifugation to bring cells into spatial contact, the plates were replaced in a humidified incubator and spheroid development was tracked with brightfield microscopy over a course of 14 days (Figure 3-1). The naming system for time points during differentiations is illustrated in Figure 2-1. Visual evaluation of brightfield images revealed, that already on the first day after seeding (d-14), B7_033#1NPC cells formed compact spheroids, with smooth edges for all cell concentrations. As the cell number increased, there was a corresponding enlargement in the size of the spheroids. Similarly, for each cell number, spheroid growth persisted throughout the cultivation period of 14 days. Following first experiments on general cell number-dependent spheroid formation and growth, additional experiments were performed to analyze proliferation, apoptosis, and neural differentiation. For this, spheroids of B7_033#1NPC1 cells were generated as described in chapter 2.1.2 and kept in FGF2-containing medium for a period of 14 days to promote further proliferation of cells. Subsequently, differentiation of cells was triggered by FGF2 withdrawal from the medium and spheroids were cultured continuously for 50 additional days. Starting the day after seeding (-d14), spheroid growth, expression of proliferation marker protein KI67 and apoptosis marker cleaved caspase-3 (CAS3) were monitored in a weekly manner by analyzing brightfield images, and fluorescently labeled cryosections for each corresponding day (Figure 3-2). Labeled cryosections were subjected to CSLM and subsequently analyzed for marker protein expression. Representative confocal images showed nuclear expression of KI67 and even distribution of signals throughout the spheroid section (Figure 3-2A). Apoptotic cells and cell fragments could be visualized by CAS3 immunolabeling and showed absence of a necrotic core in B7_033#1NPC1-derived spheroids on d14 of differentiation (Figure 3-2B).

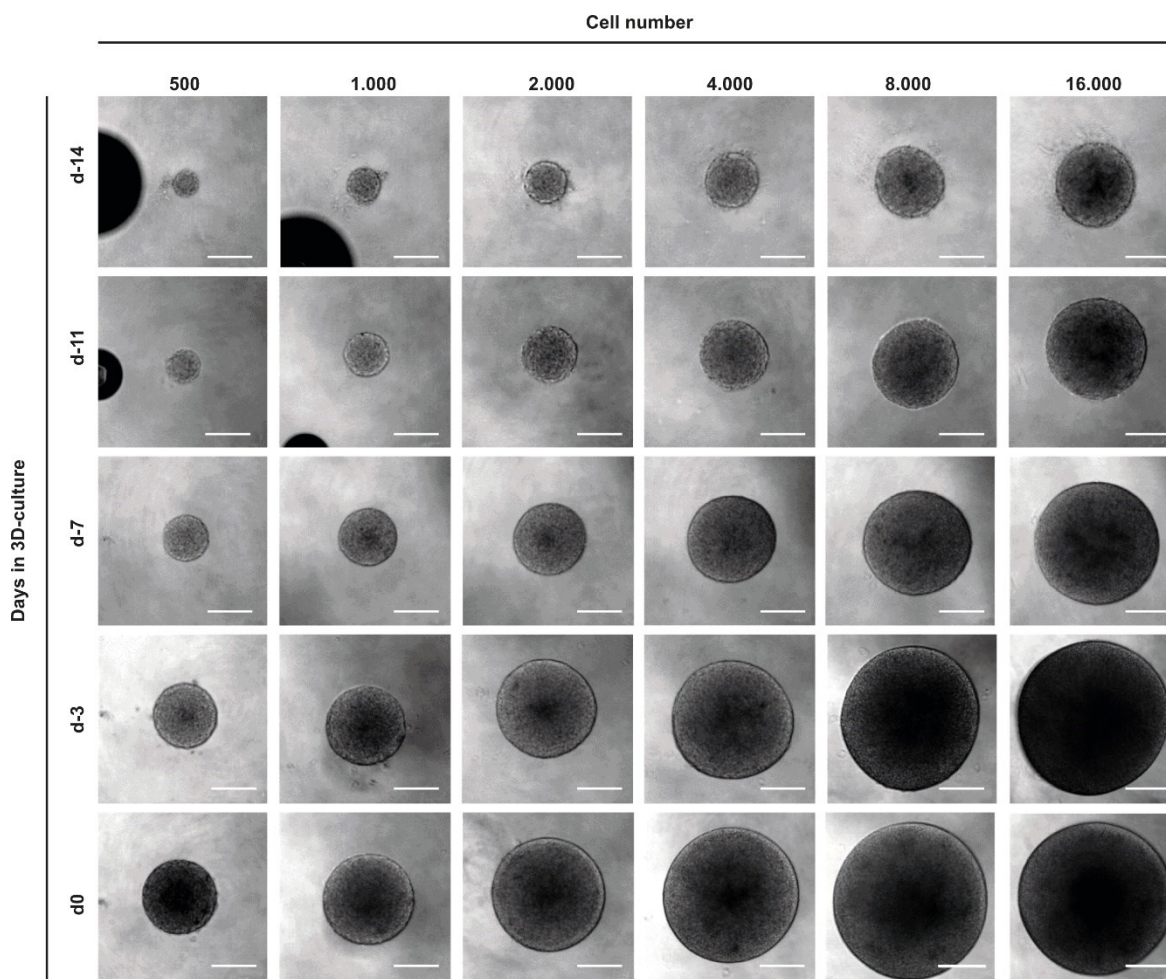


Figure 3-1: Scaffold-free spheroids can be formed from hiPSC-derived NPCs. Dissociated B7_033#1NPC1 cells were seeded onto 96-well ULA plates at concentrations of 5×10^3 to 1.6×10^5 cells per well for spheroid formation. Cultured under the presence of FGF2 for 14 days, the images depict spheroids' brightfield appearance. Progression over time is shown (top to bottom) as cell concentration increased (left to right). Scale bar: 150 μm .

Quantification of KI67-positive (KI67+) nuclei over the entire cultivation period revealed an initial increase in cell proliferation during the first seven days of 3D-cultivation, from 16.8 ± 0.5 % (mean \pm s.d.) to 30.6 ± 2.9 % (mean \pm s.d.), followed by a drop of KI67+ proportion of cells to an intermediate level of 23.2 ± 1.4 % (mean \pm s.d.) after 14 days of 3D-cultivation (Figure 3-2D). Accompanying the relative rise in KI67+ cells was a steady, linear increase of spheroid size as indicated by diameter measurements obtained from brightfield images (Figure 3-2C). Between -d14 and d0 of 3D-differentiation, B7_033#1NPC1 spheroids increased their size from 301.09 ± 11.0 μm (mean \pm s.d.) to 548.3 ± 16.5 μm (mean \pm s.d.). Upon removal of FGF2 from the medium, proliferation was decreased, registered as a sharp drop of KI67+ cells to 4.9 ± 0.8 % (mean \pm s.d.) with a continuous reduction throughout differentiation to a final value of 0.9 ± 0.3 % (mean \pm s.d.) on d50 of differentiation (Figure 3-2D). Similarly, the steady increase of spheroid diameter registered during the first two weeks of cultivation was halted upon FGF2 withdrawal. Triggering differentiation of NPCs on d0 of differentiations was accompanied by the spheroid diameter reaching a plateau between 548.3 ± 16.5 μm and 594.6 ± 15.9 μm (mean \pm s.d.) (Figure 3-2C). In contrast to KI67, the proportion of cells expressing

the apoptosis marker CAS3 was not changed in an FGF2-dependent manner, but instead continuously increased from its lowest value on -d14, 2.01 ± 0.6 % (mean \pm s.d.) to its highest value of 19.2 ± 3.1 % (mean \pm s.d.) on d50 of differentiation (Figure 3-2D).

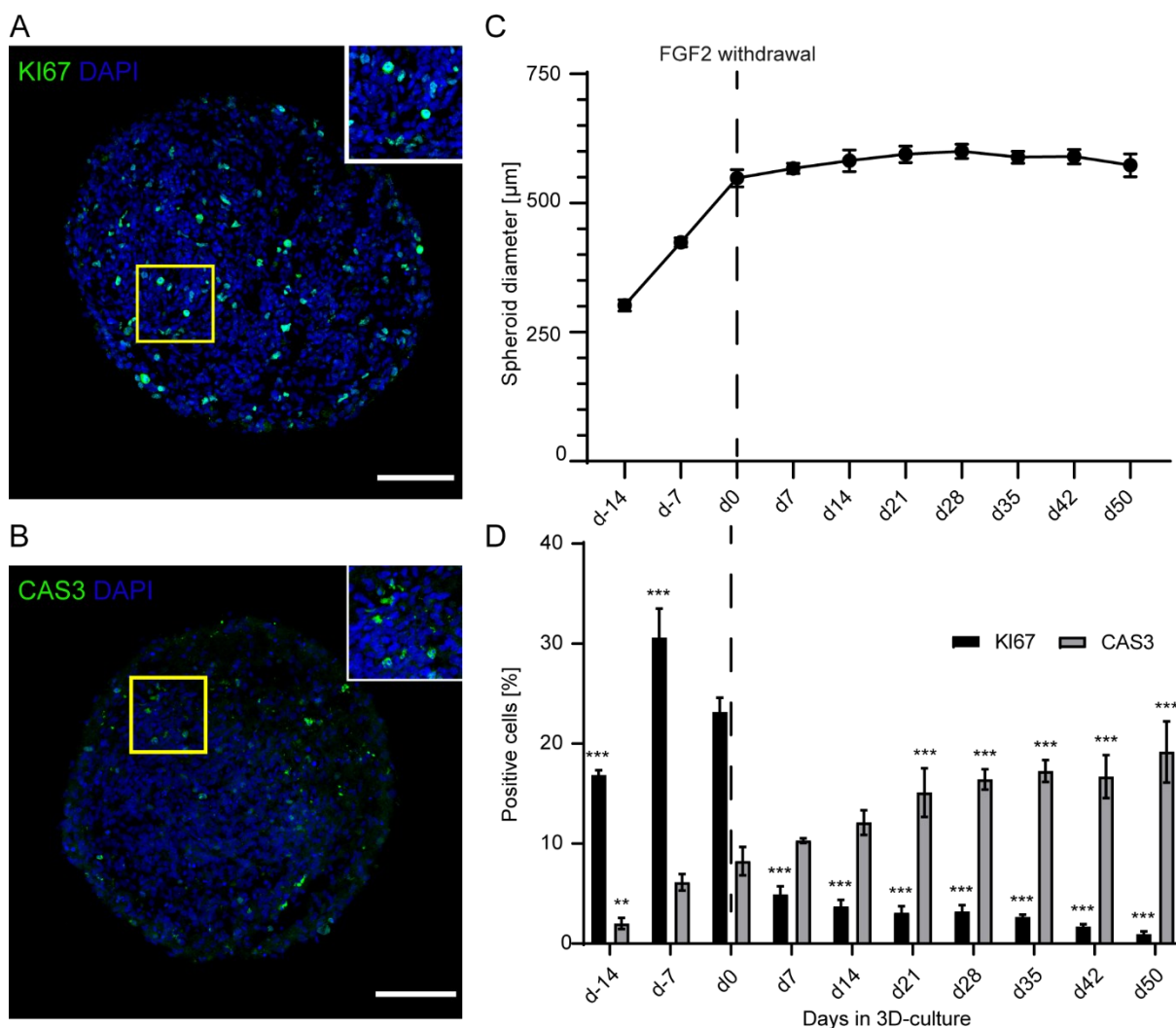


Figure 3-2: Proliferation and apoptosis in NPC-derived spheroids depend on FGF2 and cultivation time. B7_033#1NPC1 were seeded onto 96-well ULA plates at a concentration of 1×10^5 cells per well and cultured in media containing FGF2 for 14 days. Differentiation was triggered by FGF2 withdrawal (d0 of differentiation) and continued until d50. In a weekly manner, brightfield images were taken and subsequently, spheroids were fixed, cryosectioned and fluorescently labeled for proliferation marker KI67 and apoptosis marker CAS3. Figure shows representative maximum projections of d14-differentiated spheroids stained for KI67 and CAS3 (A, B, both green). Nuclei were labeled with DAPI (blue). Spheroid size throughout cultivation period was measured from brightfield images (C), whereas ratio of cells positively stained for both markers were quantified from immunolabeled cryosections (D). Graphs show mean \pm s.d. from $n = 3$ independent experiments with at least 10 measurements per time point. * $p \leq 0.05$; ** $p \leq 0.01$; *** $p \leq 0.001$. Scale bars: $100 \mu\text{m}$ ^{viii}.

^{viii} Contribution from Samira Maxhuni, see Table 8-10:

Contributions from other persons, p. 117

3.1.2 3D-cultivation of hiPSC derived neural spheroids maintains a steady pool of SOX2+ NPCs throughout differentiation

In order to assess the differentiation potential of B7_033#1NPC when cultured as spheroids, several lineage-specific marker proteins were analyzed in cryosections obtained from the same timepoints described in the previous chapter 3.1.1. Briefly, hiPSC-derived B7_033#1NPC1 cells were seeded onto ULA U-bottom plates at a concentration of 1×10^5 cells/well and cultured in the presence of FGF2 for 14 days. Subsequently, differentiation was triggered by FGF2 withdrawal from the medium (d0) and spheroids were continuously cultured until d50. Throughout cultivation, spheroids were monitored weekly for the expression of SOX2, a transcription factor known to be associated with NPCs; β -III-tubulin (TUBB3), which is expressed in young, developing neurons; and glial fibrillary acidic protein (GFAP), a marker for astrocytes. For this, spheroids were fixed on the corresponding day of differentiation, cryosectioned and fluorescently labeled via indirect immunofluorescence, followed by CLSM and quantitative analysis. Representatively for all analyzed time points, Figure 3-3 (A+B) displays exemplary confocal images of cryosections obtained from B7_033#1NPC1 spheroids on d35 of differentiation. At this stage of differentiation, all labeled marker proteins were simultaneously expressed. The NPC marker SOX2 is distributed throughout the spheroid, however an accumulation of SOX2+ nuclei towards the center was apparent (Figure 3-3 A). Vice versa, TUBB3+ cells were mainly located in peripheral regions of the spheroid, resulting in a higher signal intensity at the border (Figure 3-3 A+B). The astrocyte marker GFAP appeared to be homogeneously distributed throughout the spheroid section (Figure 3-3 B). Quantitative analysis of marker expression over time revealed a steady increase of SOX2+ cells prior to FGF2 withdrawal on d0, however throughout differentiation the proportion of NPCs did not significantly change and was maintained at a constant ratio between 58.4 ± 6.28 % (mean \pm s.d.) on d35 and 65.2 ± 0.9 % (mean \pm s.d.) on d14. In contrast to that, TUBB3 expression was already present on -d14 (24.3 ± 2.52 % (mean \pm s.d.)) and did not significantly change until d21 of differentiation, although a slight trend towards an increase could be observed until d7. From this timepoint on, TUBB3 levels started to decrease with the change becoming significant on d28 (17.5 ± 1.21 % (mean \pm s.d.)). From then on, TUBB3 expression further declined to the lowest observed value of only 5.73 ± 1.45 % (mean \pm s.d.) on d50. Interestingly, GFAP+ cells could not be observed until d14 of terminal differentiation. From then on, GFAP-levels significantly and continuously increased from 3.2 ± 1.1 % (mean \pm s.d.) to 22.6 ± 2.2 % (mean \pm s.d.) on d50.

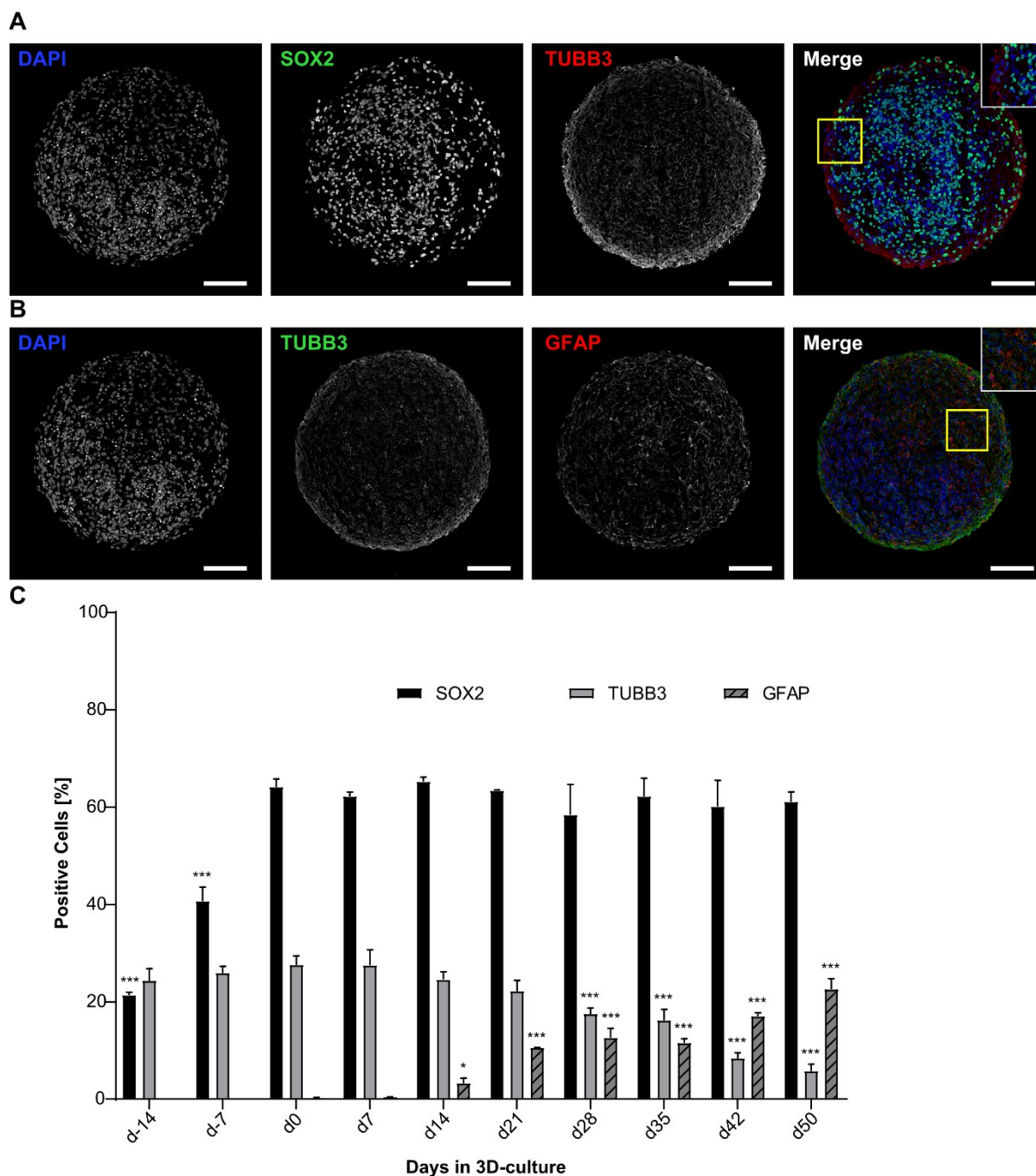


Figure 3-3: Distribution of marker protein stainings in NPC spheroids changes during differentiation. B7_033#1NPC1 cells were seeded onto 96-well ULA plates at a concentration of 10.000 cells per well and cultured in media containing FGF2 for 14 days. Differentiation was triggered by FGF2 withdrawal (d0 of differentiation) and continued until d50. On each corresponding day of analysis, spheroids were fixed, cryosectioned and immunolabeled for NPC marker SOX2, neuronal marker TUBB3 or astrocyte marker (GFAP). Figure shows representative maximum projections of d35-differentiated spheroids stained for either (A) SOX2 (green) and TUBB3 (red), or (B) TUBB3 (green) and GFAP (red). Nuclei were labeled with DAPI (A, B, blue). Ratio of cells positively stained for marker proteins were quantified from immunolabeled cryosections (C). Graph shows mean \pm s.d. from $n = 3$ independent experiments with at least 10 measurements per time point. * $p \leq 0.05$; ** $p \leq 0.01$; *** $p \leq 0.001$. Scale bars: 100 μm^{ix} .

^{ix} Contribution from Samira Maxhuni, see Table 8-10:

Contributions from other persons, p. 117

3.2 Optical clearing of hiPSC-derived neural spheroids

3.2.1 Post-fixation sample size of B7_033#1NPC1 spheroids is best preserved by Sca/eS

To evaluate the effect and efficiency of OTC protocols on the preservation of sample integrity and morphology, spheroids of hiPSC-derived B7_033#1NPC1 cells were prepared and cultured in the presence of FGF2 until a diameter of 300 μm was reached. Subsequently, spheroids were subjected to PFA-fixation, followed by immunofluorescence staining with two nuclear dyes, DAPI and DRAQ5. In order to analyze the impact of optical clearing on the stability of fluorescently labeled antibodies later on, spheroids were additionally labeled with KI67-antibody. Samples were then subjected to either embedding in PBS or Mowiol, or optical clearing with Clear^{T2}, CytoVista, Sca/eS or Glycerol, followed by image acquisition by CLSM. Before and after fixation, brightfield images were taken to measure the average sample size of uncleared samples. Likewise, diameters for embedded and cleared samples were derived from maximum projections of confocal image stacks. Visual examination of image data showed, that prior to fixation, spheroids displayed a regular, rounded shape with a smooth surface, which was not affected by subsequent treatment with PFA, immunofluorescence staining or optical clearing (Figure 3-4).

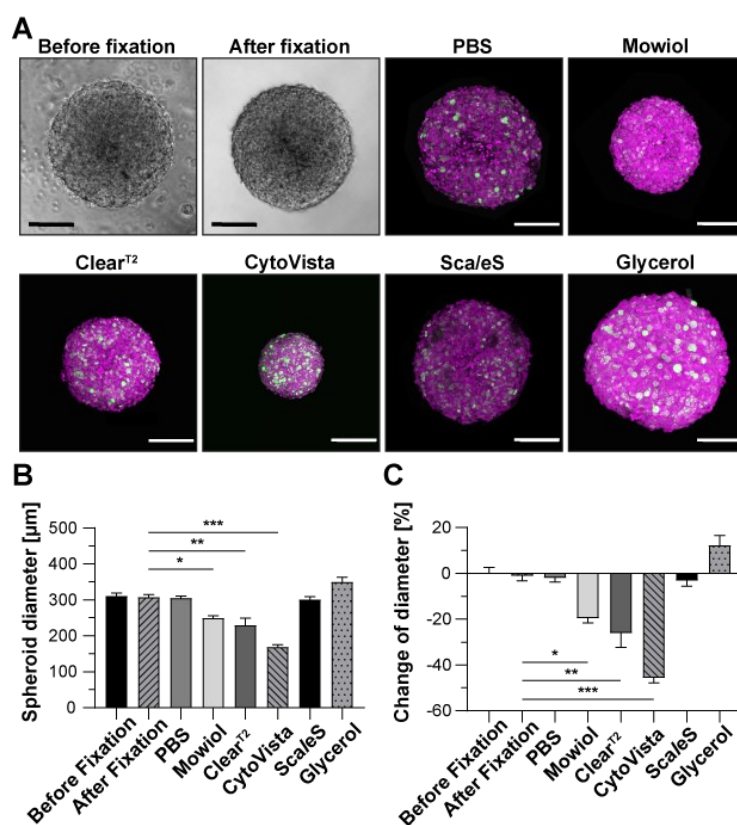


Figure 3-4: Sample size preservation is best ensured by optical clearing with Sca/eS. Upon reaching approximately 300 μm in diameter, B7_033#1NPC1 cell spheroids were fixed and stained with anti-KI67 and DRAQ5. Samples were then either optically cleared or embedded. Spheroid diameter was determined from pre- and post-fixation bright field images, and post-clearing confocal microscopy stacks. Figure shows (A) brightfield images pre- and post-fixation, with maximum projections of KI67 (green) and DRAQ5 (magenta) signals, (B) absolute average sample diameter quantification, and (C) changes in average diameter relative to pre-fixation. Graphs depict mean \pm s.d. for $n = 10$ samples per condition, with * indicating $p \leq 0.05$, ** $p \leq 0.01$, and *** $p \leq 0.001$ significance. Scale bars: 100 μm . Adapted from Nürnberg et al. (2020)²⁴⁷.

Quantitative of spheroid diameter revealed an initial size of $312 \pm 8 \mu\text{m}$ (mean \pm s.d.) before fixation (Figure 3-4). Upon PFA-fixation, spheroids did not significantly change in size compared to unfixed samples ($308 \pm 6 \mu\text{m}$ (mean \pm s.d.), Figure 3-4B, C). However, compared to the size of PFA-fixed samples, embedding in Mowiol, and optical clearing with either Clear^{T2} or CytoVista induced significant sample shrinkage ($250 \pm 6 \mu\text{m}$, $230 \pm 18 \mu\text{m}$ and $169 \pm 6 \mu\text{m}$ (mean \pm s.d.), respectively). This corresponds to a relative reduction in sample size of 20 %, 26 %, and 46 % for Mowiol, ClearT2 and CytoVista, respectively (Figure 3-4C). In contrast to that, immersion in glycerol appeared to induce slight sample swelling compared to PFA-fixed samples, however the change of \sim 12 % was not statistically significant ($350 \pm 13 \mu\text{m}$ (mean \pm s.d.)). Overall, optical clearing with Sca/eS was best able to preserve sample size $302 \pm 7 \mu\text{m}$ (mean \pm s.d.).

3.2.2 Optical clearing techniques alter fluorophore signal intensity, sample size, and optical transparency of hiPSC-derived neural spheroids

In order to investigate the impact of optical clearing methods on sample size and fluorophore preservation, as well as optical transparency, B7_033#1NPC1 spheroids of $300 \mu\text{m}$ size were PFA-fixed and stained with antibodies for proliferation marker KI67 and with the nuclear dyes DAPI and DRAQ5. Following immunofluorescence labeling, spheroids were subjected to either embedding in PBS and Mowiol, or optical clearing with Clear^{T2}, CytoVista, Sca/eS or glycerol. To ensure consistent and comparable results, confocal image stacks were captured with uniform settings. The visual representation of 3D volume projections depicted in Figure 3-5 illustrates that all of the applied methods succeeded in preserving the fluorescent labeling, however, their effectiveness varied. Moreover, upon creating 3D renderings of confocal image stacks, it became evident that there were discrepancies in the extent to which CLSM could capture different proportions of a sample. Notably, compared to control samples embedded in PBS, the spheroids that underwent optical clearing with Sca/eS and glycerol remained discernible in deeper regions across all fluorescent markers. Intriguingly, a similar effect was observed for samples simply embedded in Mowiol, although their overall size appeared marginally smaller than controls (Figure 3-5). In contrast, samples subjected to clearing with Clear^{T2} displayed a limited fraction of the sample volume, indicating insufficient transparency. As outlined in the earlier section 3.2.1, CytoVista induced extensive shrinkage of the sample by 46 % (Figure 3-4). This could also be observed in 3D renderings of confocal image stacks. Despite this shrinkage, nearly the entirety of the sample became visible. Furthermore, the notable enhancement in visibility extending to deeper layers corresponded with an increase in the KI67 signal strength specifically observed in samples that were either embedded in Mowiol or subjected optical clearing with Sca/eS or glycerol.

In summation, the initial qualitative assessment of confocal images acquired from cleared samples revealed distinctive differences in both optical transparency and fluorescence signal intensity across all markers.

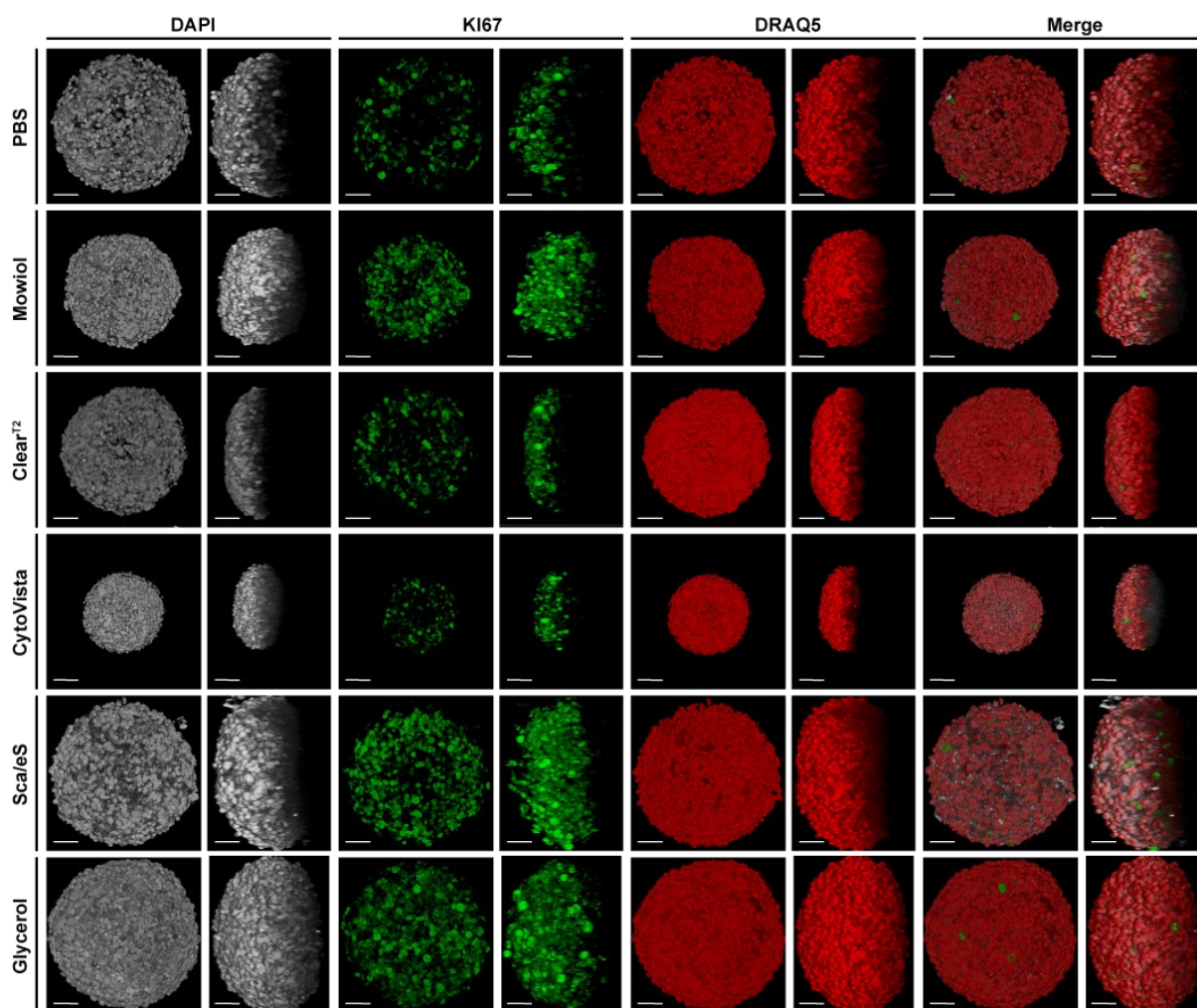


Figure 3-5: The maintenance of fluorophore signal intensity, sample size, and optical transparency is variably influenced by optical clearing techniques. Upon seeding B7_033#1NPCs, spheroids were cultivated until reaching a diameter of around 300 μm . Subsequently, fluorescent staining for DAPI (gray), KI67 (green), and DRAQ5 (red) was conducted. This was followed by either optical clearing or embedding procedures as indicated. Images display representative 3D volume projections of individual stainings and merged channels, captured through CLSM, presented in both top (left panels) and orthogonal (right panels) orientations. Scale bars: 50 μm . Adapted from Nürnberg et al (2020)²⁴⁷.

In order to illustrate the differences in optical transparency and evaluate signal distribution and localization, single optical sections from confocal image stacks were isolated at increasing imaging depth to visually compare fluorescent signal intensity of nuclear dyes and antibody staining (Figure 3-6). For all of the employed methods, DAPI and DRAQ5 both displayed nuclear colocalization. Furthermore, cells positively stained for KI67 showed nuclear distribution as well and appeared to be more frequent in peripheral regions of the spheroid. With the exceptions of CytoVista-cleared samples, stack sizes were comparable between methods. Due to the extensive degree of sample shrinkage of spheroids treated with CytoVista, the acquired number of optical sections per stack was significantly lower (Figure 3-6B). For optical sections from the top of the samples, no major difference of fluorescent signal intensity could be observed. Nonetheless, already at 50 to 100 μm of imaging depth, variations became evident (Figure 3-6A). Compared to PBS controls, the fluorescence signal intensity of the nuclear dye DAPI was increased for samples embedded in Mowiol or optically cleared with ScaleS, glycerol, or CytoVista. Especially the latter resulted in strongly enhanced DAPI fluorescence compared to all other

methods. In contrast to that, signal intensity for Clear^{T2}-treated samples was not altered noticeably. Whereas DAPI signal could still be detected for samples embedded in Mowiol or cleared with Sca/eS and glycerol beyond 150 μm depth. Especially the latter still displayed sufficiently bright fluorescence, even beyond 200 μm .

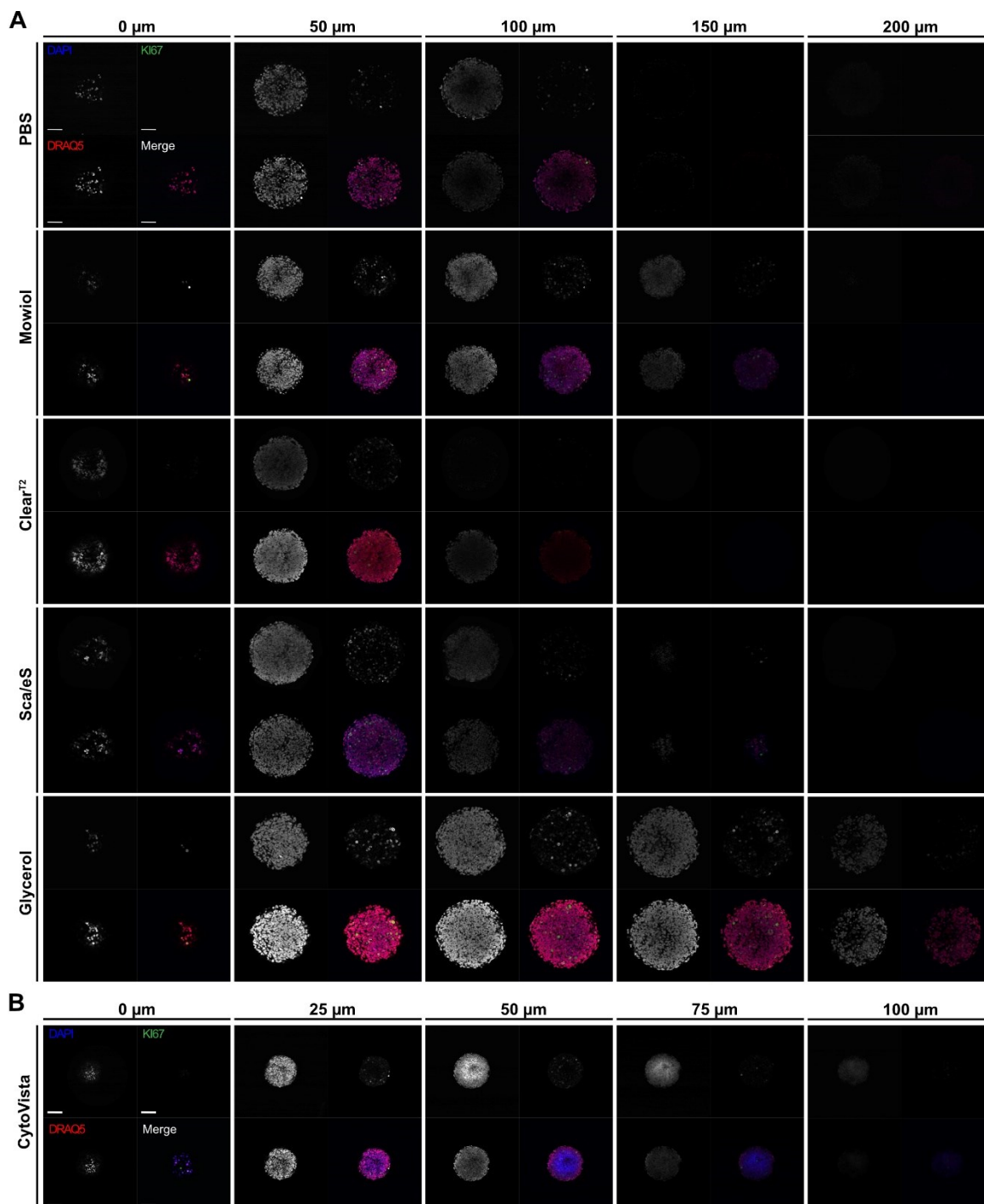


Figure 3-6: Optical tissue clearing with a glycerol performs superior and greatly improves light penetration into spheroids. After seeding B7_033#1NPCs, spheroids were cultured until reaching a diameter of approximately 300 μm and subsequently subjected to fluorescent staining for DAPI (blue), KI67 (green) and DRAQ5 (red), followed by optical clearing or embedding procedure as indicated. (A, B) Images show single optical sections of confocal image stacks at discrete z-depths, each within a distance of 50 μm (A) or 25 μm (B). Scale bars 50 μm . Adapted from Nürnberg et al. (2020)²⁴⁷.

For DRAQ5, which emits fluorescent light at a higher wavelength than DAPI, different effects were observed. Apart from *ScaleS*, fluorescence intensity of DRAQ5 was enhanced in all employed methods compared to PBS controls, with glycerol displaying the biggest increase (Figure 3-6A). Similar to DAPI, DRAQ5 fluorescence was still detectable at a depth of around 150 μm for samples embedded or optically cleared with Mowiol, *ScaleS* and glycerol. With respect to KI67 signal intensity, no visual differences were observed between methods, however, the overall frequency of KI67+ cells differed.

3.2.3 Simple immersion in a high refractive index aqueous solution of glycerol highly improves imaging depth and image quality in B7_033#1NPC1 spheroids

In order to complement the qualitative assessment of in-depth fluorescence signal intensity, quantitative analyses were conducted on confocal image volumes. By manually selecting a defined-size ROI within the central portion of the original image stack and duplicating it, a focused and representative subset of images was generated, refining the original stack for analysis. For all obtained image subsets, the depth-dependent signal intensity and SNR of the nuclear dyes DAPI and DRAQ5 was measured according to chapters 2.5.1 and 2.5.2. (Figure 3-7). To accommodate varying stack volumes and the alterations in sample size following clearing, imaging depth was corrected by normalizing it to the extent of swelling or shrinkage in comparison to untreated controls.

Analysis of the depth-dependent signal intensity of DAPI in optically cleared B7_033#1NPC1 spheroids showed a strongly increased fluorescence for samples optically cleared with CytoVista (Figure 3-7A). In contrast to that, Clear^{T2}-treated samples did not display any significant difference compared to control spheroids embedded in PBS. Embedding in Mowiol and optical clearing with *ScaleS* or glycerol led to a slight increase of DAPI signal intensity, which slowly declined with increasing depth. When evaluating based on a 50% signal loss criterion, CytoVista exhibited the superior performance for nuclear labeling with DAPI (143.5 μm), surpassing PBS controls (76.6 μm), Mowiol (138.2 μm), glycerol (118.9 μm), *ScaleS* (105.4 μm), and Clear^{T2} (83.1 μm) (Table 3-2). However, this trend was observed only when accounting for the substantial sample shrinkage associated with CytoVista clearing. Notably, the optimal absolute imaging depth for a 50% signal loss was achieved by glycerol (133.5 μm), followed by Mowiol (111.0 μm), *ScaleS* (102.0 μm), CytoVista (78.0 μm), and Clear^{T2} (60.0 μm). Interestingly, considering the normalized depth at which 90 % of the initial maximum signal intensity is lost, Mowiol exhibited the highest level of performance among the methods (274.5 μm). In terms of the absolute imaging depth at 90% signal loss, glycerol exhibited superior performance compared to other protocols (237.0 μm). For spheroids embedded in PBS, the signal intensity did not drop below 90 %.

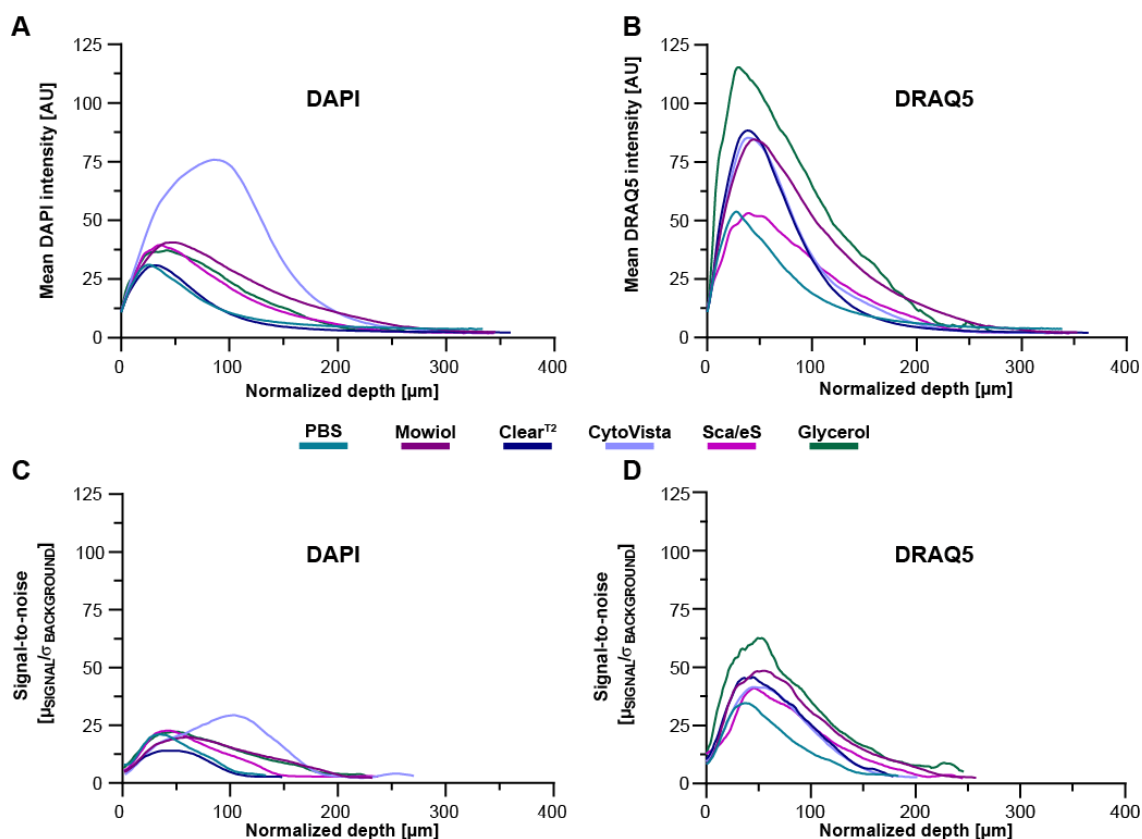


Figure 3-7: Conservation of fluorescent signal intensity, depth-dependent SNR and sample clarity are clearing method-dependent. Upon reaching a diameter of 300 μm , spheroids composed of B7_033#1NPC1 cells were fixed, subsequently stained with DAPI and DRAQ5, and then subjected to optical clearing or embedding as indicated for subsequent confocal wholemount microscopy. To assess depth-dependent signal intensity and SNR, identical-sized ROIs were positioned at the central region of each sample, from which the mean signal intensity across the entire image stack was computed. Similarly, SNR for both dyes was determined by semi-automated thresholding and measuring mean background intensity and standard deviation, as well as mean nuclear signal intensity. SNR was computed as the ratio of mean nuclear signal intensity to the average standard deviation of background intensity ($\mu\text{SIGNAL}/\sigma\text{BACKGROUND}$). To account for clearing-induced volume changes, depth values were normalized according to the corresponding degree of shrinkage or swelling. Graphs depict mean depth-dependent signal intensity of DAPI and DRAQ5 (A, B) and depth-dependent SNR (C, D). Graphs show mean \pm s.d. from $n = 10$ samples per condition. Adapted from Nürnberg et al. (2020)²⁴⁷.

Table 3-1: Summary of depth dependent DAPI signal loss and SNR in optically cleared B7_033#1NPC1 spheroids^x

	Absolute depth [μm]			Normalized depth [μm]		
	50% signal loss	90% signal loss	SNR < 5	50% signal loss	90% signal loss	SNR < 5
PBS	75,0	--	103,5	76,6	--	105,7
Mowiol	111,0	220,5	154,5	138,2	274,5	192,4
Clear^{T2}	60,0	153,0	73,5	81,3	207,2	99,5
CytoVista	78,0	118,5	96,0	143,5	218,0	176,6
Sca/eS	102,0	214,5	133,5	105,4	221,6	137,9
Glycerol	133,5	237,0	201,0	118,9	211,1	179,0

^x Contribution from Roman Bruch, see Table 8-10: Contributions from other persons, p. 117

For the nuclear dye DRAQ5, the maximum fluorescence signal intensity was strongly enhanced by sample immersion in glycerol (Figure 3-7B). Likewise, intensity was also increased for CytoVista, Clear^{T2} and Mowiol, although to a smaller extent. In contrast to that, Sca/eS clearing did not affect the maximum signal intensity of DRAQ5. With respect to the normalized, depth-dependent 50 % signal loss, Sca/eS and Mowiol performed similarly (117.8 vs. 117.7 μm), both outperforming glycerol (109.6 μm) (Table 3-2). Only marginal enhancements compared to PBS embedding were observed in the case of optical clearing using Clear^{T2} and CytoVista (79.6 vs. 87.4 vs 91.1 μm , respectively). With respect to the absolute imaging depth however, simple glycerol immersion exhibited the highest imaging depth for the 50 % signal loss criterion (133.5 μm). Similarly, the highest absolute imaging depth according to the 90 % signal loss was observed for glycerol cleared samples (226.5 μm), followed by Sca/eS (211.5 μm), Mowiol (190.5 μm), Clear^{T2} (117.0 μm) and CytoVista (99.0 μm).

Table 3-2: Summary of depth dependent DRAQ5 signal loss and SNR in optically cleared B7_033#1NPC1 spheroids
xi

	DRAQ5			DRAQ5		
	Absolute depth [μm]			Normalized depth [μm]		
	50% signal loss	90% signal loss	SNR < 5	50% signal loss	90% signal loss	SNR < 5
PBS	78,0	216,0	139,5	79,6	220,5	142,4
Mowiol	94,5	190,5	171,0	117,7	237,2	212,9
Clear^{T2}	64,5	117,0	123,0	87,4	158,4	166,6
CytoVista	49,5	99,0	85,5	91,1	182,1	157,3
Sca/eS	114,0	211,5	187,5	117,8	218,5	193,7
Glycerol	123,0	226,5	265,5	109,6	201,8	236,5

Although the overall signal intensity of fluorescent molecules is of high importance when evaluating optical clearing efficiency, it does not necessarily convey information about the quality of acquired images. A parameter more suitable to express the quality of confocal images is the SNR, which compares the strength of useful information in an image to the level of unwanted noise, such as background fluorescence or the intensity of laterally scattered light. To assess the quality and its decay of confocal images acquired from optically cleared spheroids, the SNR was calculated according to chapter 2.5.2. Results were plotted against the normalized imaging depth and are displayed in Figure 3-7C and D. A commonly applied rule in image processing is the Rose criterion, which states, that a SNR of at least 5 is necessary to still reliably distinguish between noise and meaningful signal²⁵³. This criterion was used to determine the depth of an image stack, beyond which no usable information can be inferred anymore and the results for both nuclear dyes are summarized in Table 3-1 (DAPI) and Table 3-2 (DRAQ5). Apart from CytoVista clearing, the depth-dependent SNR of DAPI in optically cleared spheroids did not exceed a value of 25 and continuously decayed beyond 50 μm of normalized depth. However, despite displaying the highest maximum SNR, the Rose criterion of DAPI in CytoVista-cleared

xi Contribution from Roman Bruch, see Table 8-10: Contributions from other persons, p. 117

samples (176.6 μm) was met at a smaller normalized depth compared to glycerol (179.0 μm) and Mowiol (192.4 μm). Clearing with Clear^{T2} resulted in a reduced image quality, which is reflected by the lowest normalized depth of 99.5 μm for reaching the Rose criterion. Taking the absolute imaging depth into account, immersion in 88 % glycerol superseded all other protocols with an absolute depth of 201,0 μm for reaching a SNR of 5. CytoVista and Clear^{T2} (96,0 μm and 73.5 μm , respectively) performed worse than simple embedding in PBS (103.5 μm).

Analysis of the second nuclear dye DRAQ5 revealed overall higher SNR values compared to results obtained for DAPI. Compared to PBS controls, all clearing techniques increased the normalized depth-dependent image quality, with glycerol clearing displaying the highest maximum SNR and the greatest normalized depth for meeting the Rose criterion (236.5 μm). Taking the absolute imaging depth into account, superiority of glycerol became even more evident, surpassing all other methods with respect to the 50 % and 90 % signal loss (123.0 μm and 226.5 μm , respectively), as well as the depth for meeting the Rose criterion (265.5 μm).

3.2.4 Glycerol-based optical clearing yields superior imaging and segmentation quality in hiPSC-derived neural precursor spheroids

Alongside evaluating depth-dependent fluorescence signal decay and SNR, an assessment was conducted to determine how well optical clearing protocols facilitate the generation of images that are optimized for automated image segmentation. For this, confocal image stacks of optically cleared B7_033#1NPC1 spheroids, stained for KI67 and nuclei with DRAQ5, were processed as little as possible and subsequently subjected to a previously published image segmentation algorithm by Schmitz et al. (2017)^{216, xii}. Pre-processing involved minimal background correction to optimize segmentation for all clearing conditions and conversion into 8bit format. Segmentation parameters were chosen as described in section 2.5.3. Figure 3-8A presents a comprehensive compilation summarizing representative optical sections, accompanied by their corresponding orthogonal views. This summary provides an overview of both raw images and the results of segmentation obtained from the central regions of the spheroids, which were embedded in PBS or Mowiol, or optically cleared with Clear^{T2}, CytoVista, ScaleS or glycerol. For all analyzed conditions, nuclear signals from DRAQ5 fluorescence could be segmented, although the quality of the results varied. For spheroids embedded in PBS, nuclei were only segmented in the upper half of the sample. For central regions, where signal intensities were too low to be successfully registered by seed detection algorithms, no nuclei were detected, thus appearing as a dark area in the center of the sample. While embedding in Mowiol or employing optical clearing techniques led to improved segmentation for both fluorescent stainings, it's worth noting that in the case of Clear^{T2}-treated samples, the segmentation of the lower half of the spheroids was found to be incomplete. Furthermore, separation of overlapping nuclei on the border regions was insufficient,

^{xii} Contribution from Mario Vitacolonna, see Table 8-10: Contributions from other persons, p. 117

leading to undersegmentation and large, clumped label masks. On the contrary, labels from nuclei located in the inner part of the samples were small and fragmented and therefore oversegmented. A similar effect was observed for the segmentation of KI67+ nuclei. Regarding Mowiol-embedded samples, the segmentation of DRAQ5 showed improvement compared to PBS controls, although undersegmentation of closely positioned nuclei persisted. Detection of KI67+ cells was elevated compared to PBS controls, with no prominent over- or undersegmentation of signals observed. Nonetheless, in comparison to optically cleared samples, fewer KI67+ cells were evident in raw image stacks. Similar to Clear^{T2}, detection of both nuclear signals in the lower part of CytoVista-cleared spheroids was not sufficient due to depth-dependent signal loss. Moreover, nuclear signals originating from the lower sections of samples treated with *ScaleS* and glycerol clearing remained discernible even at greater imaging depths. While a slight inclination toward oversegmentation of overlapping DRAQ5 signals was still evident, this tendency was notably less pronounced in contrast to all other techniques employed. For both clearing methods, a high number of KI67+ cells were detected, however the quality of the segmentation of glycerol-cleared samples was slightly improved over *ScaleS*.

Quantification of the label masks resulting from the segmentation of DRAQ5 signals demonstrated a consistent rise in the number of segmented nuclei for all applied methods when compared to the PBS control (Figure 3-8B). Notably, optically cleared samples exhibited a significantly higher count of nuclei in comparison to embedding techniques. The highest number of segmented DRAQ5+ nuclei was measured for optical clearing with *ScaleS* and glycerol. A similar trend was observed for the segmentation of KI67+ nuclei, however, significantly more cells were only detected for optical clearing with *ScaleS* and glycerol. In summary, only the latter two methods consistently and reliably detected nuclear signals from fluorescent labeling across the entire spheroid. However, it is worth noting that *ScaleS* exhibited a slightly more pronounced tendency toward oversegmentation. Taking this observation into consideration, optical clearing using glycerol emerges as the preferred choice among the various clearing techniques in terms of imaging depth, signal-to-noise ratio (SNR), and segmentation quality.

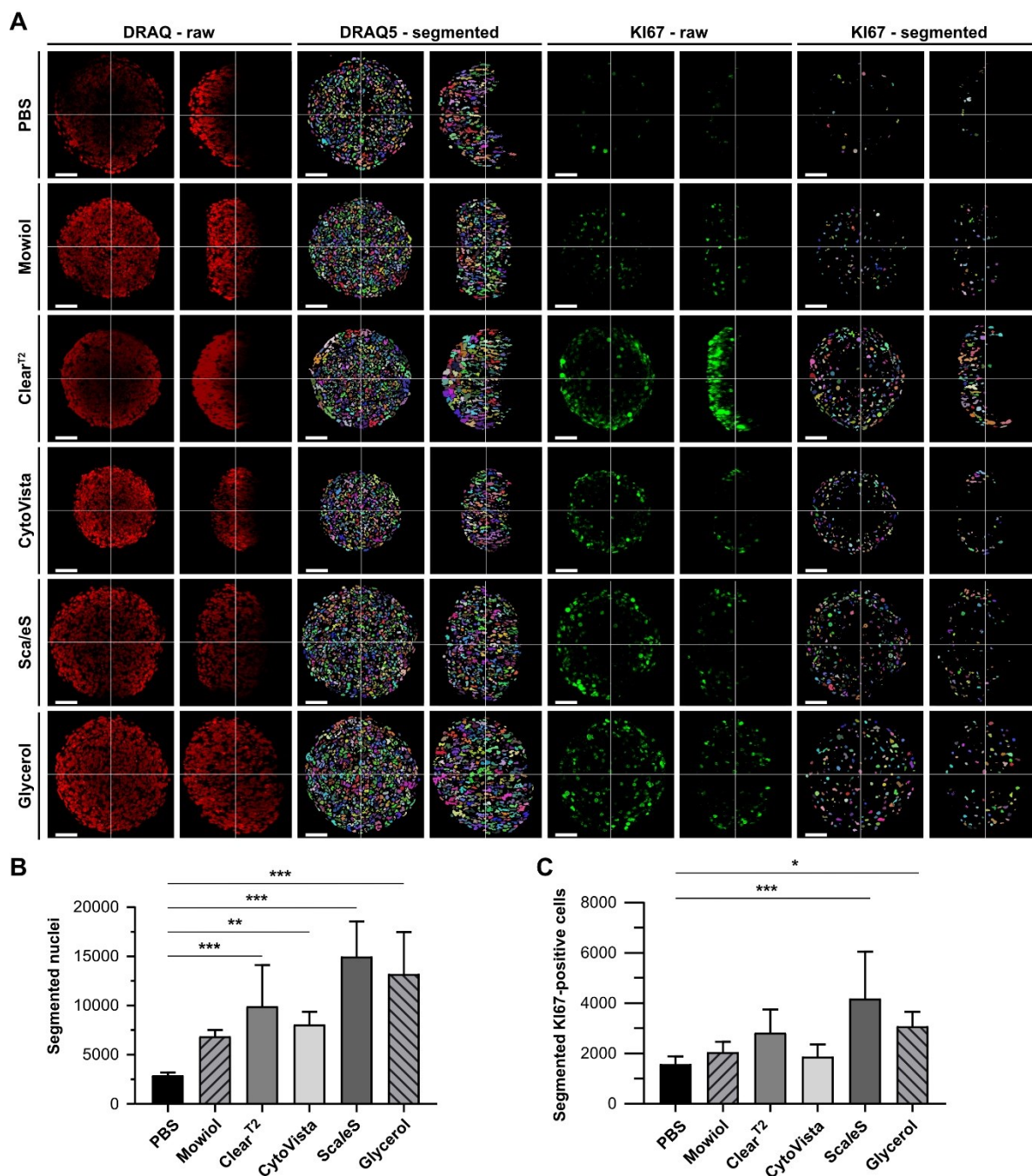


Figure 3-8: Optical clearing of hiPSC-derived neural spheroids enhances detection and quantification of cell nuclei with varying quality. B7_033#1NPC1 cell spheroids, reaching a diameter of approximately 300 μm , were fixed and stained with anti-KI67 and DRAQ5. Subsequent to staining, the spheroids underwent optical tissue clearing or embedding, as indicated, followed by confocal whole mount microscopy. Semi-automated image segmentation was used for the detection and quantification of KI67+ and DRAQ5+ nuclei. (A) Depicted are raw single optical sections alongside orthogonal views from central regions for both markers (KI67 – raw; DRAQ5 – raw), along with their corresponding segmented images (KI67 – segmented; DRAQ5 – segmented). Fluorescence signals for KI67 and DRAQ5 are color-coded as green and red, respectively, in raw images. Distinct colors were assigned to segmented nuclei for enhanced visual discrimination. Scale bars denote 50 μm . B-C: Quantitative analysis of DRAQ5+ nuclei (B) and KI67 (C) as a function of clearing/embedding protocol. Data show mean + s.d.; $n \geq 10$; * $p \leq 0.05$; ** $p \leq 0.01$; *** $p \leq 0.001$. Adapted from Nürnberg et al. (2020).²⁴⁷

3.2.5 Glycerol clearing of differentiated hiPSC-derived neural spheroids reveals intricate networks of neurons and astrocytes

Based on the results obtained in the previous sections, glycerol was determined to be the most suitable optical clearing protocol for B7_033#1NPC1 spheroids. However, those experiments were conducted in non-differentiating samples. To confirm robustness of the method in differentiating spheroids, samples of B7_033#1NPC1 cells were prepared according to section 2.1.2, and spheroids were differentiated after a 2-week cultivation period under presence of FGF2. Differentiation was triggered by FGF2 withdrawal and samples were cultivated for a total of 35 additional days. After 14 days, a part of the samples were PFA-fixed, subjected to nuclear staining with DAPI, followed by optical clearing with glycerol. Visualization was achieved by LSM (Figure 3-9A). Results showed, that with RI matching using glycerol and LSM, the entire spheroid could be visualized across a depth of approximately 600 μm . It has to be noted, however, that LSM is able to achieve higher imaging depths than traditional CLSM, explaining the differences between results obtained during analysis of optical clearing protocols and the application of glycerol clearing shown in this section. To monitor the differentiation state of 3D-cultured B7_033#1NPC1 cells, remaining samples were fixed and immunofluorescence staining for differentiation markers was conducted. Two neuronal markers were chosen to analyze neuronal differentiation: the axonal marker tau, and somatodendritic protein Map2A (Figure 3-9B, left panel). Spatial separation of those proteins indicate polarization of developing neurons and is a process necessary for correct functionality of neurons. To separate neurons from non-differentiating NPCs, the marker nestin was included in the staining panel. After fluorescence labeling, spheroids were optically cleared with glycerol and subsequently imaged with LSM. Results showed a clear separation between neuronal and precursor marker proteins, indicating partial neuronal differentiation of NPCs. While neurons appeared to be mostly located on the surface of the samples, nestin signal spread throughout the whole spheroid. Moreover, fluorescence signals from tau and Map2A were clearly separated in a portion of the neurons. In addition to these markers, samples were also labeled with anti-TUBB3 and anti-GFAP antibodies to analyze spatial localization of developing neurons and astrocytes (Figure 3-9B, right panel). Results obtained for TUBB3 staining confirmed observations gained from Map2A and tau fluorescence, namely neurons being mainly located in the outer regions of the spheroid. GFAP+ cells, however, spread throughout the sample.

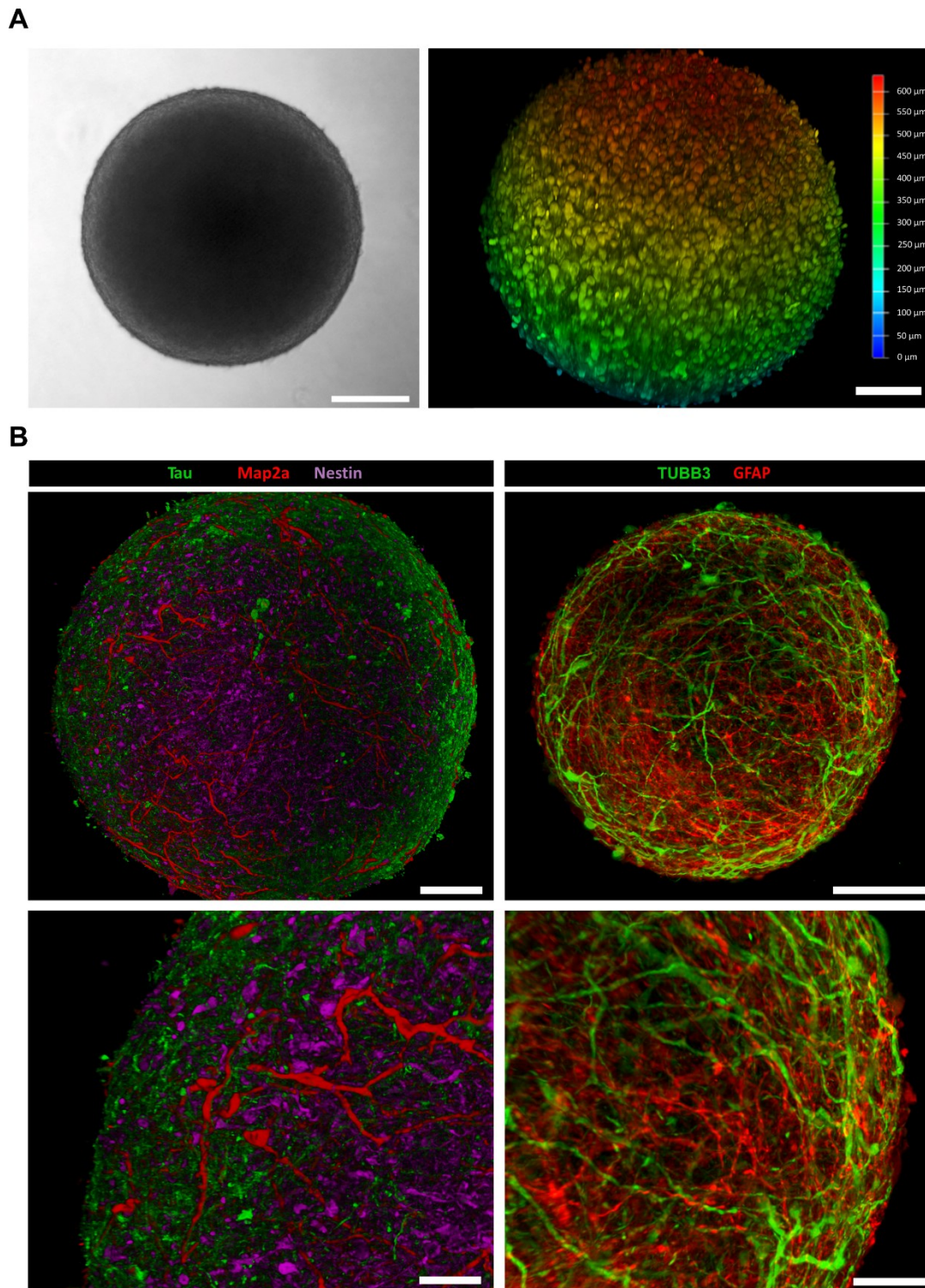


Figure 3-9: Optical clearing of neural spheroids reveals partial polarization and differentiation into neurons and astrocytes. Spheroids of B7_033#1NPC1 cells were differentiated under absence of FGF2 for a period of 14 (A) or 35 (B) days, and subsequently subjected to fixation, fluorescence staining and optical clearing with glycerol. (A) depicts a phase contrast image (left) and a spheroid labeled with DAPI. After clearing, samples were subjected to light sheet microscopy for whole mount imaging (right). Color coding of fluorescent image indicates the depth in z-direction. Scale bars: 200 μm . After three more weeks of differentiation, samples were labeled for either neuronal markers Tau (red), Map2a (green) and NPC marker nestin (magenta, left panel), or neuron marker TUBB3 (green) and GFAP (red) to label astrocytes (right panel). Lower panels depict zoom images. Spatial separation of Tau and Map2A signal indicates neuronal polarization. Scale bars: upper panels 100 μm , lower panels 50 μm .

3.3 Comparison of optical clearing protocols across different 3D-cell culture models

Besides evaluating effective optical clearing methods in hiPSC-derived NPC spheroids of the B7_033#1NPC1 line, additional spheroids from various cell lines were investigated to assess the inter-cell line efficiency of optical clearing. These cell lines were comprised of the human keratinocyte cell line HaCaT, the fibroblast cell line CCD-1137SK, malignant colon carcinoma-derived HT29 cells and the human tongue-cell line HTC8^{xiii}. Additionally, optical clearing was employed to a complex co-culture spheroid model comprised of fibroblasts, keratinocytes, and the malignant melanoma cell line SK-MEL-28, which is referred to as triculture in the context of this work. Confocal images and results of depth-dependent signal intensity and SNR measurements of this co-culture model is provided in section 3.3.3, however, the results on sample size preservation are presented together with data obtained from mono-culture spheroids. Furthermore, to extend 3D-cell cultures beyond spheroid models, a complex microchip-based co-culture prepared from fibroblasts and ECFP-tagged MDA-MB-231 breast cancer cells was included in the analysis (chapter 3.3.3). All models were prepared according to chapter 2.1, and subsequently underwent analogous processing to that of B7_033#1NPC1 spheroids. It has to be noted that *ScaleS* clearing of HT29 spheroids was not conducted due to sample loss.

3.3.1 Cell line dependent sample volume changes are best prevented by *ScaleS* and glycerol clearing

For the assessment of sample size preservation upon immunofluorescence staining and optical clearing, spheroids of the respected cell lines were PFA-fixed, fluorescently labeled and subsequently subjected to either embedding in PBS or Mowiol, or optical clearing with Clear^{T2}, CytoVista, *ScaleS* or glycerol. Before and after fixation, brightfield images were acquired to measure the native sample size, and PFA-induced changes of the spheroid volume. Measurements of embedded or optically cleared samples were obtained from maximum intensity projections of confocal image stacks obtained from confocal whole mount microscopy. Results for all cell lines are summarized in Figure 3-10. Prior to fixation all cell lines displayed a diameter of approximately 300 μm , except for the triculture model, which was significantly larger (Figure 3-10A). For all analyzed conditions, all cell lines showed comparable trends towards shrinkage or swelling induced by the employed methods, although an increase of the sample size was only observed for glycerol clearing of B7_033#1NPC1 spheroids. PFA-fixation appeared to induce minor sample shrinkage, especially in samples from HaCaT, CCD-1137SK and HTC-8 spheroids (Figure 3-10A). However, only the latter displayed a significant reduction of the spheroid size ($-12.3 \pm 2.5 \%$) (Figure 3-10B).

^{xiii} Contribution from Elena von Molitor, Julia Klicks, Mario Vitacolonna and Tiziana Cesetti, see Table 8-10: Contributions from other persons, p. 117

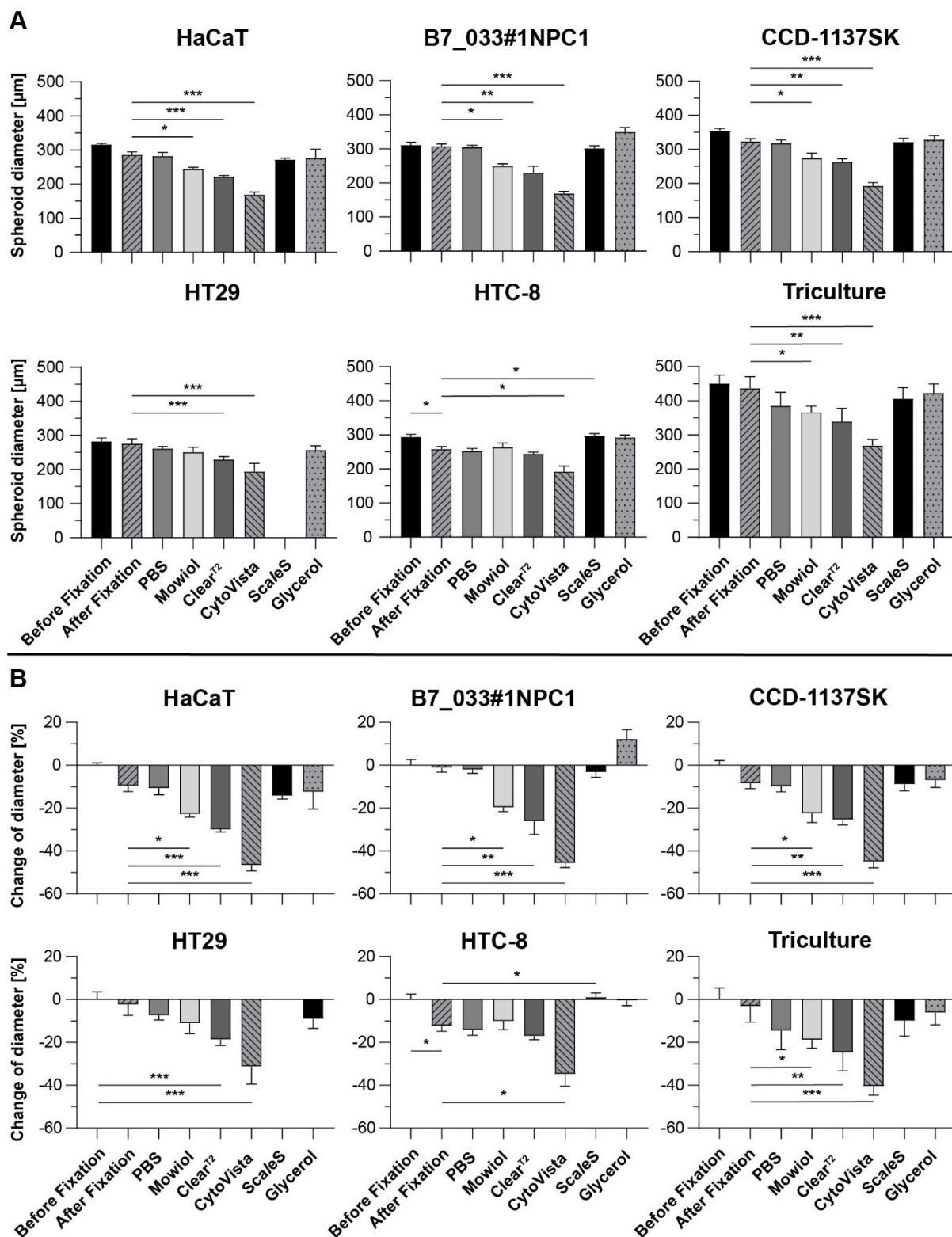


Figure 3-10: Post-fixation sample volume changes are best averted by optical clearing with Glycerol and ScaleS, in a cell line-independent matter. Spheroids of all indicated cell lines were fixed, stained with anti-KI67, DAPI and DRAQ5 and subsequently subjected to optical clearing or embedding methods. For all cell lines, sample diameters were determined from brightfield images before and after fixation, and from confocal image stacks after staining and clearing. Apart from melanoma tri-cultures (approximately 450 µm), all samples were fixed upon reaching a diameter of approximately 300 µm. (A) Quantification of absolute average sample diameter. (B) Quantification of absolute average sample diameter. (C) Change of average sample diameter with respect to the pre-fixation state. Graphs show mean ± s.d. from $n \geq 7$ samples per condition. * $p \leq 0.05$; ** $p \leq 0.01$; *** $p \leq 0.001$. Source: Nürnberg et al (2020)².

Overall, embedding in Mowiol, and optical clearing with Clear^{T2} or CytoVista consistently induced sample shrinkage across all tested cell lines, which was highest in HaCaT spheroids cleared with CytoVista. (-46.6 ± 2.5 %) (Figure 3-10B). In contrast to that, ScaleS and Glycerol performed best in maintaining the post-fixation sample size across all tested clearing protocols.

Comparison of cell line behavior upon individual embedding or clearing techniques showed significant differences between samples of different origins. PFA-induced sample shrinkage was observed in HaCaT, CCD-1137SK and HTC-8 spheroids, whereas B7_033#1NPC1, HT29 and triculture spheroids did not display noticeable reduction of the sample size (Figure 3-11A). Embedding in PBS did not further alter the diameter of most samples, except for HT29 and triculture spheroids (Figure 3-11B). Embedding in Mowiol induced a more pronounced shrinkage of spheroids across all cell lines, however in HT29 and HTC-8 cells, this effect was less pronounced (Figure 3-11C). Among the employed clearing techniques, Clear^{T2} caused substantial reduction of the sample volume, especially in HaCaT, B7_033#1NPC1, CCD-1137SK and triculture spheroids. Similar to effects observed for Mowiol-embedding, HT29 and HTC-8 cells were less prone to Clear^{T2}-induced shrinkage (Figure 3-11D). Overall, smaller sample diameters were observed in all cells cleared with Clear^{T2} when compared to Mowiol. Similarly, although considerably more pronounced, CytoVista induced extensive shrinkage in all spheroids, ranging from 31.2 ± 7.8 % in HT29 cells to 46.6 ± 2.5 % for HaCaT samples (Figure 3-11E). As observed for Mowiol embedding and Clear^{T2}, HT29 and HTC-8 spheroids displayed the least amount of volume reduction compared to other cell lines. Up to this point, all of the employed methods showed similar trends amongst all cell lines and differences were only observed with respect to the strength of volume changes. For ScaleS, however, HaCaT cells and triculture spheroids showed a further decrease of the spheroid diameter, compared to the post-fixation sample size (Figure 3-11E). In contrast to this, the initial decrease of the sample diameter observed after PFA-fixation of HTC-8 spheroids was compensated by ScaleS, almost restoring the sample dimensions of the pre-fixation state (Figure 3-11F). For CCD-1137SK and B7_033#1NPC1 cells, no significant changes compared to the post-fixation diameter were observed. Glycerol clearing yielded the least sample alteration compared to PFA-fixed spheroids. However, B7_033#1NPC1 spheroids exhibited a tendency towards slight sample swelling and the initial volume reduction observed in HTC-8 spheroids upon PFA-fixation was compensated upon glycerol clearing (Figure 3-11G). In summary, concerning the maintenance of the original sample size, Mowiol embedding and optical clearing using Clear^{T2} or CytoVista led to notable reductions in spheroid volume through shrinkage across all cell culture models, albeit with varying degrees depending on the cell line. Only ScaleS clearing and glycerol immersion consistently preserved sample dimensions closely aligned with the pre- or post-fixation size. Overall, HT29 and HTC-8 cells were less prone to sample shrinkage when compared to other cell lines.

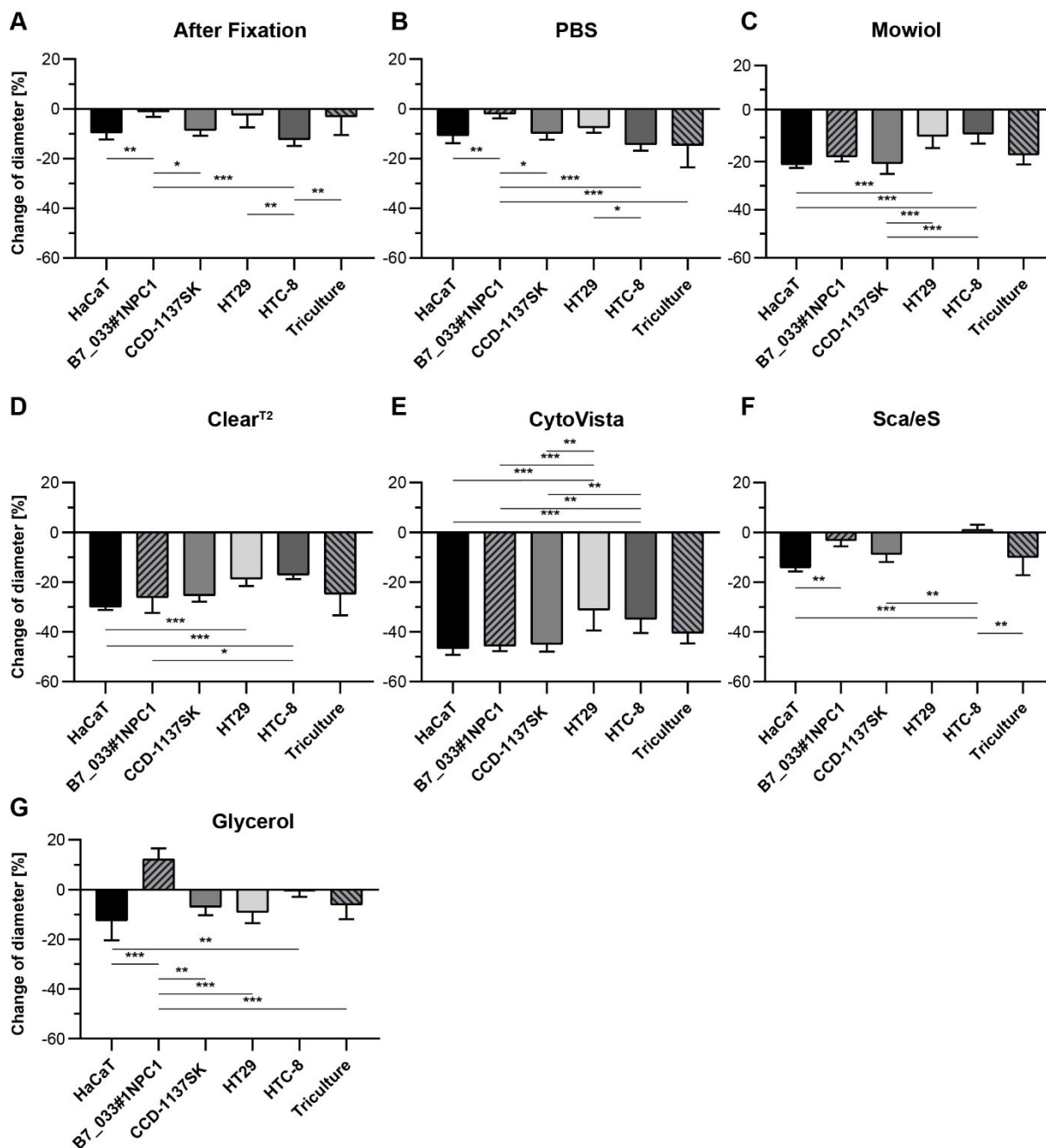


Figure 3-11: Degree of sample volume change induced by clearing varies based on the cell line. Spheroids of all indicated cell lines were fixed, stained with anti-KI67, DAPI and DRAQ5 and subsequently subjected to optical clearing or embedding methods. For all cell lines, sample diameters were determined from brightfield images before and after fixation, and from confocal image stacks after staining and clearing. Apart from melanoma tri-cultures (approximately 450 μm), all samples were fixed upon reaching a diameter of approximately 300 μm . A-G Quantitative analysis of clearing method-dependent change of average sample diameter with respect to pre-fixation state. Graphs show mean \pm s.d. from $n \geq 7$ samples per condition. * $p \leq 0.05$; ** $p \leq 0.01$; *** $p \leq 0.001$. Source: Nürnberg et al (2020)²⁴⁷.

3.3.2 Depth-dependent signal intensity and SNR vary across cell lines, OTC methods and fluorophores.

In addition to sample size preservation, fluorophore stability, depth-dependent signal intensity and SNR were analyzed in mono-culture spheroids of HaCaT, CCD-1137SK, HT29 and HTC-8 cells, in order to complement results obtained for B7_033#1NPC1 spheroids and to evaluate differences between cell lines. For this, spheroids of approximately 300 μm were generated from the respective cell lines and subjected to PFA-fixation and subsequent fluorescent labeling with two nuclear dyes, DAPI and DRAQ5, and antibody for the proliferation marker KI67. Next, labeled spheroids were either embedded in PBS or Mowiol, or optically cleared with Clear^{T2}, CytoVista, Sca/eS or glycerol. Subsequently, image acquisition of stained spheroids was performed by CLSM, and image stacks were used for subsequent analysis.

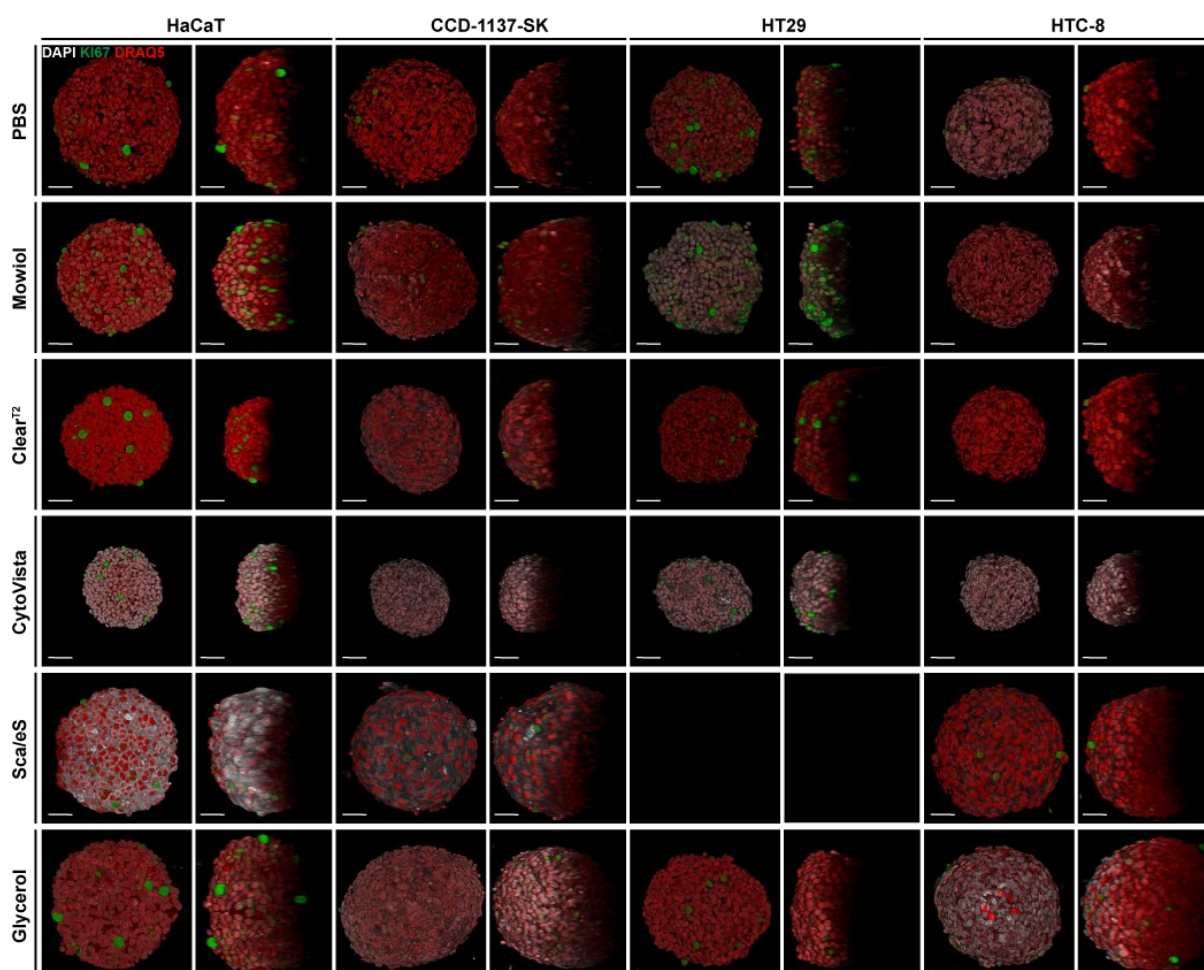


Figure 3-12: Preservation of signal intensity, sample size, and optical transparency through optical clearing varies across different cell types. For the generation of spheroids, various cell lines were used as indicated and cultured until reaching an approximate diameter 300 μm . Subsequently, spheroids were fixed, immunostained for KI67 (green), and the two nuclear dyes DAPI (grey) and DRAQ5 (red), followed by optical tissue clearing or embedding. Images show representative 3D volume projections of single stainings and merged channels for each cell line, acquired by confocal whole mount microscopy in top (left panels) and orthogonal (right panels) orientation. Sca/eS clearing was not performed in HT29-spheroids. Scale bars: 50 μm . Adapted from Nürnberg et al. (2020)²⁴⁷.

An analysis of confocal images demonstrated the presence of detectable fluorescent labels in all spheroids across different conditions. Notably, there were observable differences in the overall signal intensity among various cell lines and staining methods, as shown in Figure 3-12. Additionally, examining orthogonal views of 3D volume projections highlighted variations in the portion of the sample volume captured by CLSM. Analysis of the mean signal intensity across the normalized imaging depth revealed a major increase of the maximum DAPI fluorescence over PBS controls across all cell lines optically cleared with CytoVista (Figure 3-13A-D). In particular, HT29 spheroids displayed the largest increase of DAPI intensity compared to all other employed methods (Figure 3-13C). A similar effect was observed for DRAQ5 in monoculture spheroids of HT29 and CCD-1137SK cells (Figure 3-13 B-C). However, in relation to the 90% signal loss threshold across the normalized depth, all of four tested cell lines exhibited the enhanced effectiveness of glycerol clearing. In the case of spheroids originating from CCD-1137SK, HT29, or HTC-8 cells, the DAPI fluorescence met the 90% signal loss requirement at depths of 351.7 μm , 249.1 μm , and 265.4 μm , respectively (Appendix 8.4., Table 8-4 - Table 8-8^{xiv}). In image stacks obtained from HaCaT spheroids DAPI signal intensity never decreased below 90 % of its maximum in glycerol cleared samples. However, the same was observed for PBS-embedded samples. The absolute depth at which the 90 % signal loss was reached in glycerol cleared samples was calculated to be at 327.0, 151.5, and 264.0 μm for CCD-1137SK, HT29, or HTC-8 cells, respectively (Appendix 8.4., Table 8-4 - Table 8-8). With respect to DRAQ5, measurements were more inconsistent between different cell culture models. Whereas ScaleS performed best at achieving high normalized and absolute imaging depths in HaCaT spheroids (271.2 and 232.5 μm , respectively) and HTC-8 cells (308.5 and 312.0 μm , respectively). For spheroids derived from the fibroblast cell line CCD-1137SK best results were obtained with glycerol immersion (331.5 and 356.6 μm , respectively). In HT29 samples, none of the applied clearing methods achieved a higher depth for the 90 % signal loss threshold than simple Mowiol embedding (224.4 and 133.5 μm , respectively).

In terms of the SNR measurements conducted across the imaged sample volume, the consistently heightened maximum signal intensity of DAPI observed with CytoVista clearing, aligned with elevated SNR values (Figure 3-14A-D). Nevertheless, it's important to note that this heightened SNR becomes discernible only after the imaging depth has been normalized in relation to the alterations in the sample volume. After accounting for the extensive sample shrinkage during CytoVista clearing, the depth at which the Rose criterion of 5 was met was measured to be at 219.3, 190.8, 152.7 and 122.0 μm , respectively for HaCaT, CCD-1137SK, HT29 and HTC8 cells (Appendix 8.4., Table 8-4 - Table 8-8). The absolute depth, however, was much lower compared to other clearing methods (117.0, 105.0, 70.5, and 79.5 μm , respectively).

^{xiv} Contribution from Roman Bruch, see Table 8-10: Contributions from other persons, p. 117

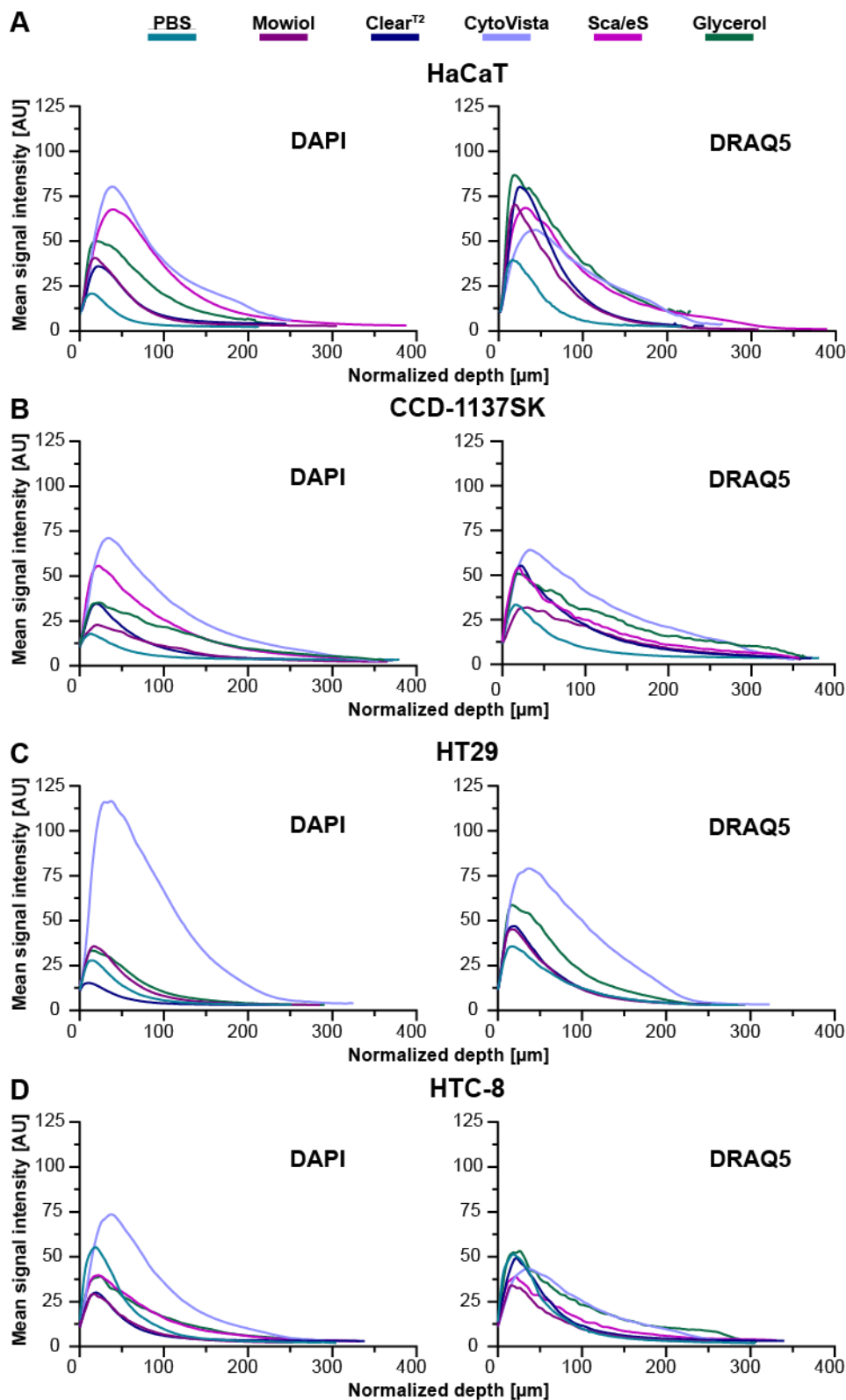


Figure 3-13: Optical clearing with CytoVista consistently preserves high fluorescence intensity of DAPI, independent of the cell line. Upon reaching an approximate diameter of 300 μm , spheroids of all indicated cell lines were fixed, stained with the two nuclear dyes DAPI and DRAQ5 and subsequently subjected to optical clearing or embedding methods as indicated. In order to analyze depth-dependent signal intensity, equally sized ROIs were placed in the center of each sample, from which the mean signal intensity throughout the entire image stack was measured. For compensation of clearing-induced volume changes, depth values were normalized to the corresponding degree of shrinkage or swelling. In addition to NPC-derived spheroids, measurement was performed for HaCaT (A), CCD-1137SK (B), HT29 (C) and HTC-8 (D) spheroids. Adapted from Nürnberg et al. (2020)²⁴⁷.

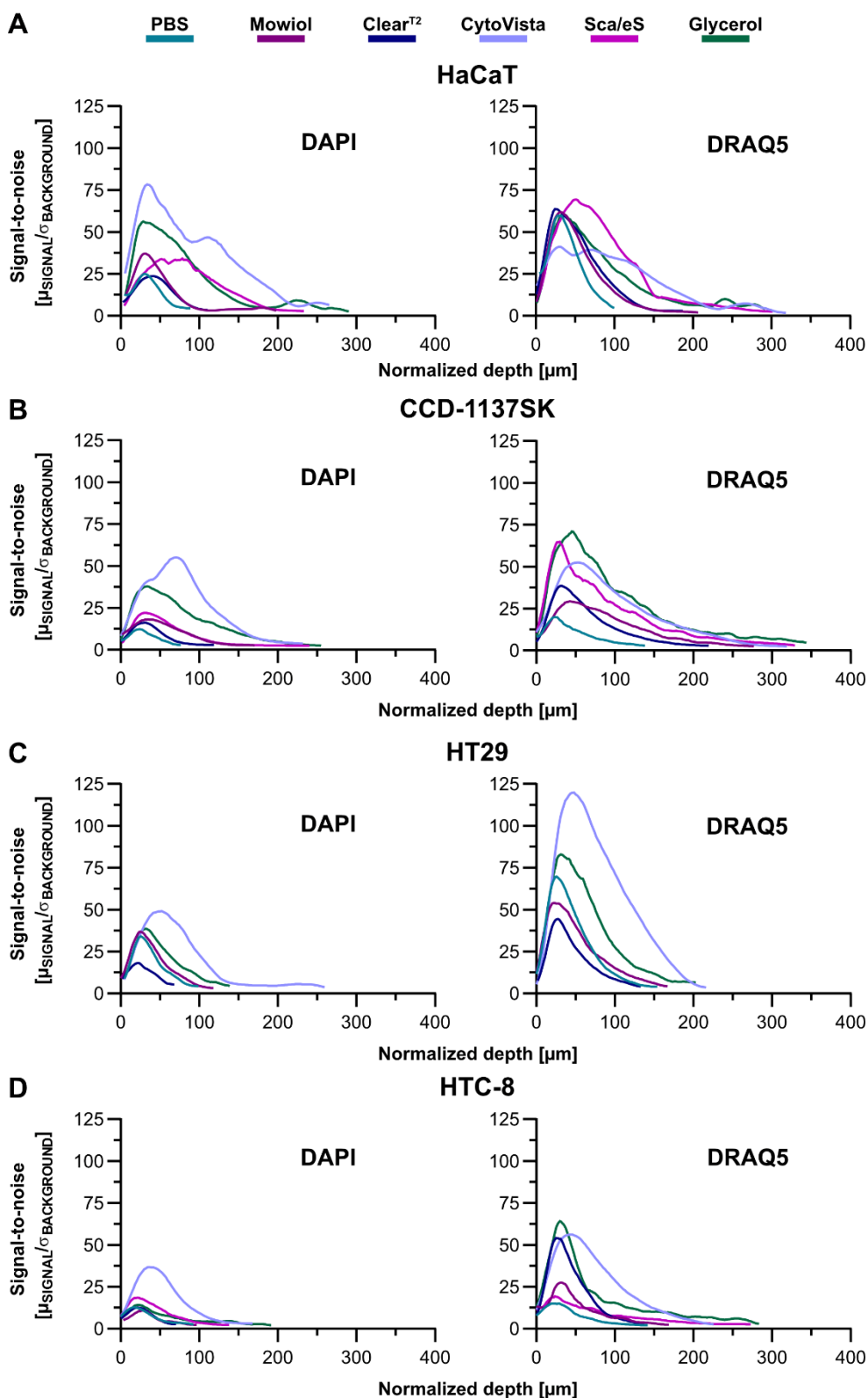


Figure 3-14: Preserved high fluorescence intensity of DAPI upon CytoVista clearing is accompanied by increased depth-dependent SNR. Upon reaching an approximate diameter of 300 μm , spheroids of all indicated cell lines were fixed, stained with nuclear dyes DAPI and DRAQ5 and subsequently subjected to optical clearing or embedding methods, as indicated. To analyze the depth-dependent SNR, equally sized ROIs were placed in the center of each sample, from which the signal intensities throughout the entire image stack were measured. SNR was determined via semi-automatic thresholding and measurement of mean background intensity and standard deviation and mean nuclear signal intensity. SNR was calculated as the ratio of mean nuclear signal intensity to the average standard deviation of background intensity ($\mu_{\text{SIGNAL}}/\sigma_{\text{BACKGROUND}}$). For compensation of clearing-induced volume changes, depth values were normalized to the corresponding degree of shrinkage or swelling. In addition to NPC-derived spheroids, measurement was performed for HaCaT (A), CCD-1137SK (B), HT29 (C) and HTC-8 (D) spheroids. Adapted from Nürnberg et al. (2020)²⁴⁷.

Optical clearing with Clear^{T2} did not lead to an SNR improvement over PBS-embedding across the absolute depth for any of the cell lines. In fact, in HT29-derived spheroids, the Rose criterion was met at a smaller depth compared to PBS controls (37.5 vs. 53.5 μm). Best results with respect to the depth-dependent SNR of DAPI in HaCaT and HTC-8 spheroids were achieved with ScaleS (153.0 and 88.5 μm , respectively), while glycerol clearing performed best for CCD-1137SK and HT29 cells. For DRAQ5 glycerol achieved consistently superior results over other clearing techniques (232.5 – 309 μm), except for spheroids prepared from HaCaT cells, which were best cleared with ScaleS (239.7 μm) (Appendix 8.4., Table 8-4 - Table 8-8). In general, the deterioration of image quality with increasing depth exhibited a more pronounced trend for DAPI. The calculated average depth to fulfill the Rose criterion was approximately 90 μm for DAPI, notably contrasting with DRAQ5's average depth of around 178 μm .

3.3.3 Efficiency of optical clearing is influenced by the complexity of 3D-cell culture models

In addition to monoculture spheroids, the performance of optical clearing protocols was assessed in two more 3D-cell culture models of higher complexity. The first model consisted of a spheroid triculture model of skin cancer and was comprised of fibroblasts, human keratinocytes, and malignant melanoma cells, according to Klicks et al. (2019)^{38,xv}. Briefly, a core spheroid of CCD-1137SK fibroblasts was prepared by seeding singularized cells onto ULA mutliwell plates. After three days of cultivation, a mixture of HaCaT keratinocytes and SK-MEL-28 melanoma cells was added to fibroblasts spheroids and cultivated for two additional days. During this time, singularized cells engulfed the core spheroid by a self-driven mechanism, forming a compact structure, with CCD-1137SK fibroblasts in the center, followed by surrounding layers of HaCaT cells, and SK-MEL28 in the periphery. Prior to seeding of keratinocytes and melanocytes, cells were labeled with CellTracker Red and CellTracker green, respectively. The two cellular dyes are frequently used to label live cells in culture for subsequent fluorescence microscopy. After formation of tricultures was achieved, samples were PFA-fixed, fluorescence labeled with the nuclear dye DAPI and anti-KI67 antibody. Subsequently, tricultures were either embedded in PBS or Mowiol, or optically cleared with either Clear^{T2}, CytoVista, ScaleS or 88 % glycerol. Following whole mount CLSM, acquired image volumes were used to evaluate optical clearing efficiency and compatibility with fluorescence labels. Analysis of depth-dependent signal intensities and SNR was performed in analogy to monoculture spheroids. Representative images and results of image analyses are summarized in Figure 3-15. As previously described, triculture samples exhibited similar post-fixation volume changes as monoculture spheroids, in particular a significant sample shrinkage for Mowiol embedding and optical clearing with Clear^{T2} and CytoVista (Figure 3-10 and Figure 3-11).

^{xv} Contribution from Julia Klicks, see Table 8-10: Contributions from other persons, p. 117

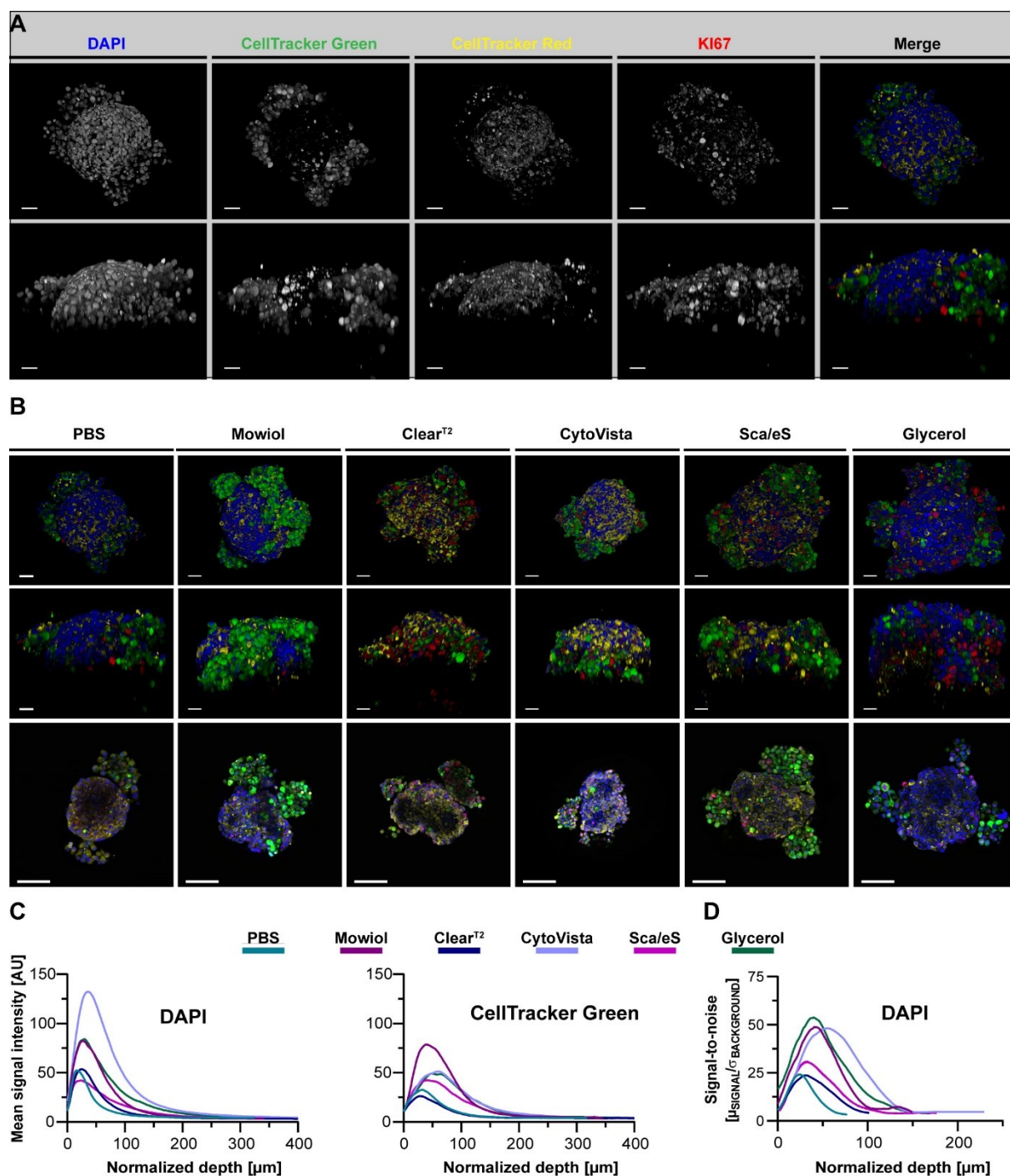


Figure 3-15: Optical clearing efficiency is affected by complexity of a spheroid-based tri-culture model. Melanoma tri-culture spheroids were generated by initiating the formation of a central spheroid composed of CCD-1337SK fibroblasts. After a 72-hour incubation period, HaCaT keratinocytes labeled with CellTracker Red and SK-MEL-28 melanoma cells labeled with CellTracker Green were simultaneously introduced. Following an additional two days of cultivation, the spheroids underwent fixation and subsequent staining using anti-KI67 and DAPI. These spheroids were then either embedded or subjected to clearing procedures as specified. Confocal 3D imaging of the entire spheroid cultures was conducted. (A) Representative 3D-volume projections from top (upper panel) and orthogonal (lower panel) orientation of fluorescence signals of a PBS-embedded spheroid (blue: DAPI, green: CellTracker Green, yellow: CellTracker Red, red: KI67). Scale bars: 50 μm . (B) Representative images of tri-culture spheroids after embedding/clearing as indicated. Upper and middle panels show volume projections from top and side views. Lower panels show single optical sections at 75 μm of imaging depth. Scale bars: 50 μm in (top and middle row), 100 μm (bottom). Quantitative analysis of the normalized, depth-dependent mean signal intensity of DAPI and CellTracker Green (C) and SNR of DAPI signals (D). Mean of $n = 10$ spheroids per condition. Source: Nürnberg et al. (2020)²⁴⁷.

For all tested conditions, fluorescence of all labels was preserved, however, as observed for monoculture spheroids, CytoVista clearing displayed the highest maximum intensity for DAPI, followed by Mowiol embedding and glycerol. Regarding the SNR, glycerol achieved the best results with an absolute depth for meeting the Rose criterion of 88.5 μm (Appendix 8.5, Table 8-9). Compared to monoculture spheroids, however, none of the employed methods caused sufficient optical transparency, emphasized by depths for the 50 % signal loss of 22.5 – 49.5 μm . Furthermore, if HaCaT or CCD-1137SK were cultured separately as monoculture spheroids, considerably higher imaging depths were achieved for DAPI staining (142.5 μm and 175.5 μm , respectively, chapter 3.2.4). In comparison to DAPI, CellTracker Green appeared to be best conserved with Mowiol, with no evident improvement of the imaging depth for optical clearing methods. However, it is important to highlight that the spatial localization of CellTracker Green was primarily concentrated in the sample's periphery, with significantly lower to negligible presence in the central region where the measurements were conducted. All the preceding results were conducted with spheroids, which are often a preferred model in 3D-cell culture. To complement the examination of optical clearing efficiency within 3D-cell culture models, a microchip-based approach was incorporated to assess OTC protocols in contexts beyond spheroids^{xvi}. For this purpose, a co-culture of CCD-1137SK fibroblasts and ECFP-expressing MDA-MB-231 cells was prepared and cultured on small transparent polymer chips (Dynarrays). These chips were equipped with evenly distributed cavities of uniform size, with a diameter of 300 μm and a depth of 200 μm . Within these cavities, cells could be cultured in a 3D manner, facilitating a substantial number of replicates with minimal source material. Samples of co-cultures on Dynarray chips were prepared according to Keller et al. (2020)²⁵¹. In brief, singularized MDA-MB-231 and CCD-1137SK cells were simultaneously seeded onto collagen 1 coated Dynarray chips and allowed to adhere to the cavities for three hours. Subsequently, medium was added to cells and the chips were continuously cultured for a total of nine days. Prior to seeding, fibroblasts were labeled with CellTracker Red to distinguish cell types during image analysis. After the cultivation period, whole chips were fixed with PFA, followed by carefully cutting Dynarrays into equally sized sections. Subsequently, individual sections were fluorescently labeled with DRAQ5 and anti-KI67 antibody and subjected to either direct embedding in Mowiol, or optical clearing with Clear^{T2}, CytoVista, ScaleS or glycerol. After CLSM, image stacks were analyzed in analogy to the spheroid models, however, an analysis of clearing-mediated sample volume change was not conducted due to the spatial restrictions exerted by the chip material. For the same reason, normalization of imaging depth was omitted. Representative images of single cavities are summarized in Figure 3-16A and B. Analysis of the overall signal intensity revealed a particularly high sensitivity of ECFP to optical clearing. While Mowiol and glycerol were able to maintain a high signal intensity, all other employed methods caused a major decrease of the fluorescence intensity. Especially Clear^{T2} treatment of samples caused a profound loss of ECFP signal (Figure 3-16C).

^{xvi} Contribution from Florian Keller, see Table 8-10: Contributions from other persons, p. 117

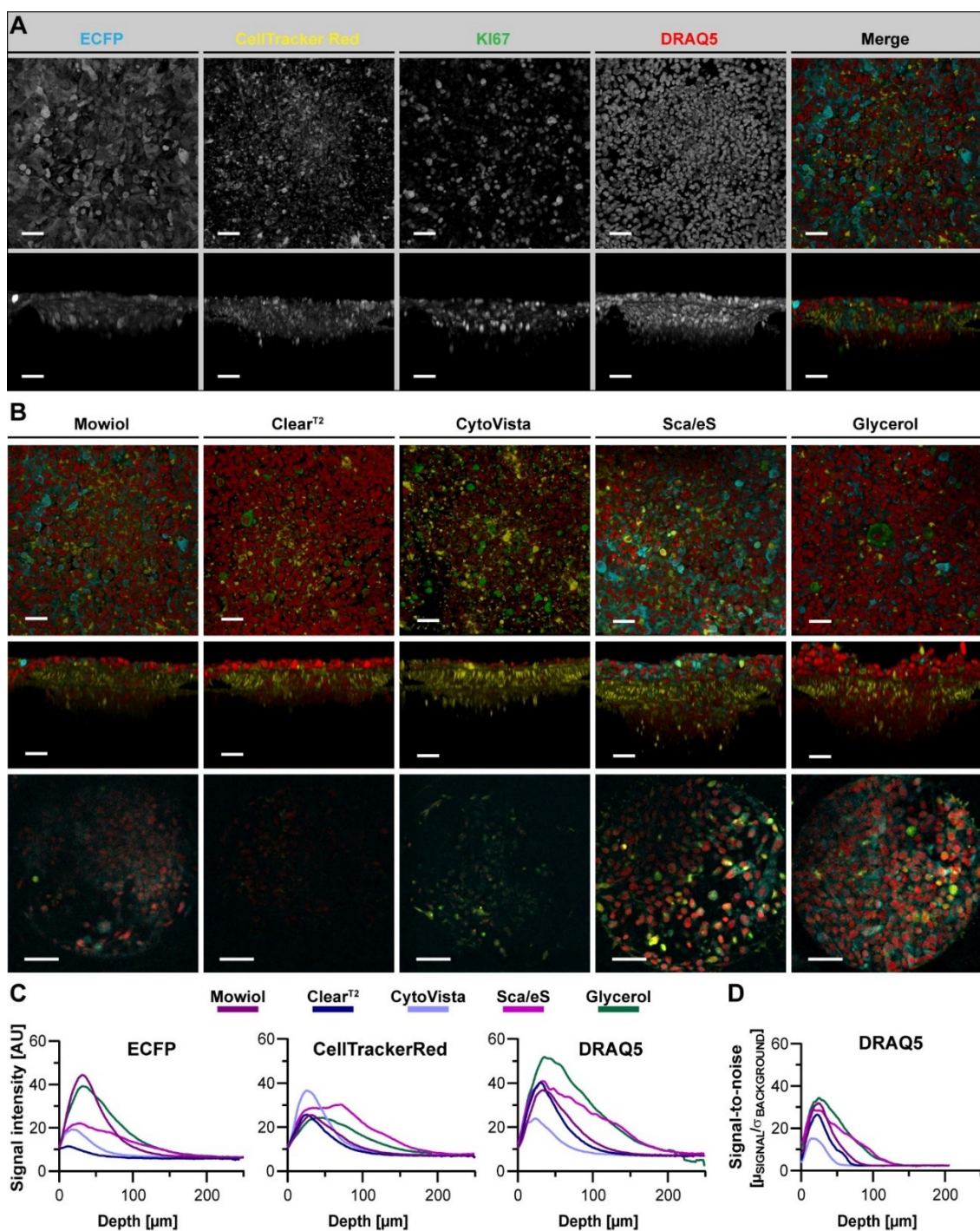


Figure 3-16: ECFP fluorescence is preserved by optical clearing with glycerol and quenched by Clear^{T2} in a chip-based co-culture model of breast cancer cells and fibroblasts. ECFP-expressing MDA-MB-231 breast cancer cells were co-seeded with CellTracker Red labeled CCD-1375K fibroblasts into Dynarray chips with 300 μm wide cavities. After 9 days of cultivation, chips were fixed, stained with anti-KI67 and DRAQ5, and then embedded or cleared as indicated. (A) Representative top and orthogonal 3D-volume projections of fluorescence signals (indicated) of Mowiol-embedded chip cavities are shown in upper and lower panels, respectively. In the merge, ECFP appears in cyan, CellTracker Red in yellow, KI67 in green, and DRAQ5 in red. Scale bars, 50 μm . (B) Depicted are representative images of chip cavities after different types of embedding/clearing, as indicated. Top and side view maximum projections are shown in upper and middle panels. Lower panels show single optical sections at 75 μm of imaging depth. Scale bars, 50 μm in upper and middle row, 100 μm in lower row. (C, D) Quantitative analysis of mean signal intensity of ECFP, CellTracker Red, and DRAQ5 (C) and SNR of DRAQ5 signals (D) as a function of depth. Mean of $n = 10$ cavities per condition. Source: Nürnberg et al. (2020)^{247, xvii}.

^{xvii} Contribution from Florian Keller, see Table 8-10: Contributions from other persons, p. 117

Although Mowiol was able to preserve ECFP fluorescence, it displayed a rapid signal loss in greater depth. Only Sca/eS and glycerol were able to maintain sufficient ECFP signal at deeper regions of the cavities. Comparable results were observed for DRAQ5 and CellTracker Red upon Sca/eS and Glycerol clearing. Compared to ECFP, CellTracker Red displayed high maximum signal intensity upon CytoVista clearing, but a rapid decrease with increasing depth to the level of Clear^{T2} and Mowiol. SNR measurements over the imaging depth showed no improvement of image quality for Clear^{T2} (44.5 μm) and CytoVista (64.5 μm) over Mowiol (74.5 μm) embedding with respect to the Rose criterion (Figure 3-16D, Appendix 8.5, Table 8-9). Furthermore, only Sca/eS and glycerol clearing were able to reach higher depths for the SNR cutoff (115.5 and 112.5 μm , respectively). Taken together, results obtained from complex 3D-cell culture models revealed an overall decrease of clearing efficiency compared to monoculture spheroids.

3.3.4 Optical clearing with glycerol consistently improves nuclear segmentation across cell culture models.

Alongside evaluating depth-dependent fluorescence signal decay and SNR, assessments were conducted to determine the effectiveness of optical clearing protocols in producing images optimized for automated image segmentation across multiple cell lines and cell culture methods. To achieve this, monoculture spheroids were created using HaCaT keratinocytes, CCD-1137SK fibroblasts, HT29 carcinoma cells, and HTC-8 tongue cells. Additionally, the analysis included melanoma tricultures and Dynarray cocultures composed of breast cancer cells and fibroblasts. All samples derived from the different cell lines and culture methods were fixed with PFA and subsequently stained with the nuclear dye DRAQ5 and an anti-KI67 antibody. Afterwards, samples were either embedded in PBS or Mowiol, or optically cleared with Clear^{T2}, CytoVista, Sca/eS or glycerol. Subsequent to whole mount CLSM, acquired image stacks underwent minimal processing, including background correction, to enhance segmentation outcomes. Segmentation was accomplished using a 3D-seeded watershed algorithm previously described by Schmitz et al. (2017)²¹⁶, with parameters chosen according to section 2.5.3^{xviii}. The total counts of both nuclei and KI67+ were determined for all cell culture models and results are summarized in Figure 3-17. Quantitative analysis revealed a high variance between different OTC protocols and cell lines. Overall, the total number of segmented cells varied between cell lines, which can be, in part, attributed to different seeding numbers during sample generation. While Mowiol embedding was sufficient to significantly improve segmentation results in monoculture spheroids from HaCaT cells, fibroblasts, HTC-8 cells and tricultures, this effect was not observed in HT29 and Dynarray samples. In monoculture spheroids, all optical clearing techniques achieved a significantly higher count of DRAQ5 positive nuclei, except for CytoVista clearing of HaCaT spheroids. Overall, highest cell counts across cell culture models were consistently observed for glycerol clearing. With respect to complex 3D-cell

^{xviii} Contribution from Mario Vitacolonna, see Table 8-10: Contributions from other persons, p. 117

culture models, Clear^{T2} was not able to improve nuclear segmentation and CytoVista only marginally increased the number of nuclei detected by the algorithm. In both co-culture models, glycerol clearing showed to be superior to other clearing techniques. Segmentation of KI67⁺ cells revealed high variation among cell lines, which can be attributed to differences between proliferation rates of the respective cell lines. Amongst all the tested embedding and clearing techniques, only glycerol was able to significantly increase the count of KI67⁺ cells, consistently across all cell lines. For other employed clearing techniques, Sca/eS clearing displayed different trends. In spheroid models, more proliferating cells were detected upon Sca/eS clearing compared to controls, however, this was not the case for the Dynarray coculture model. In fact, significantly fewer cells were identified to be KI67⁺.

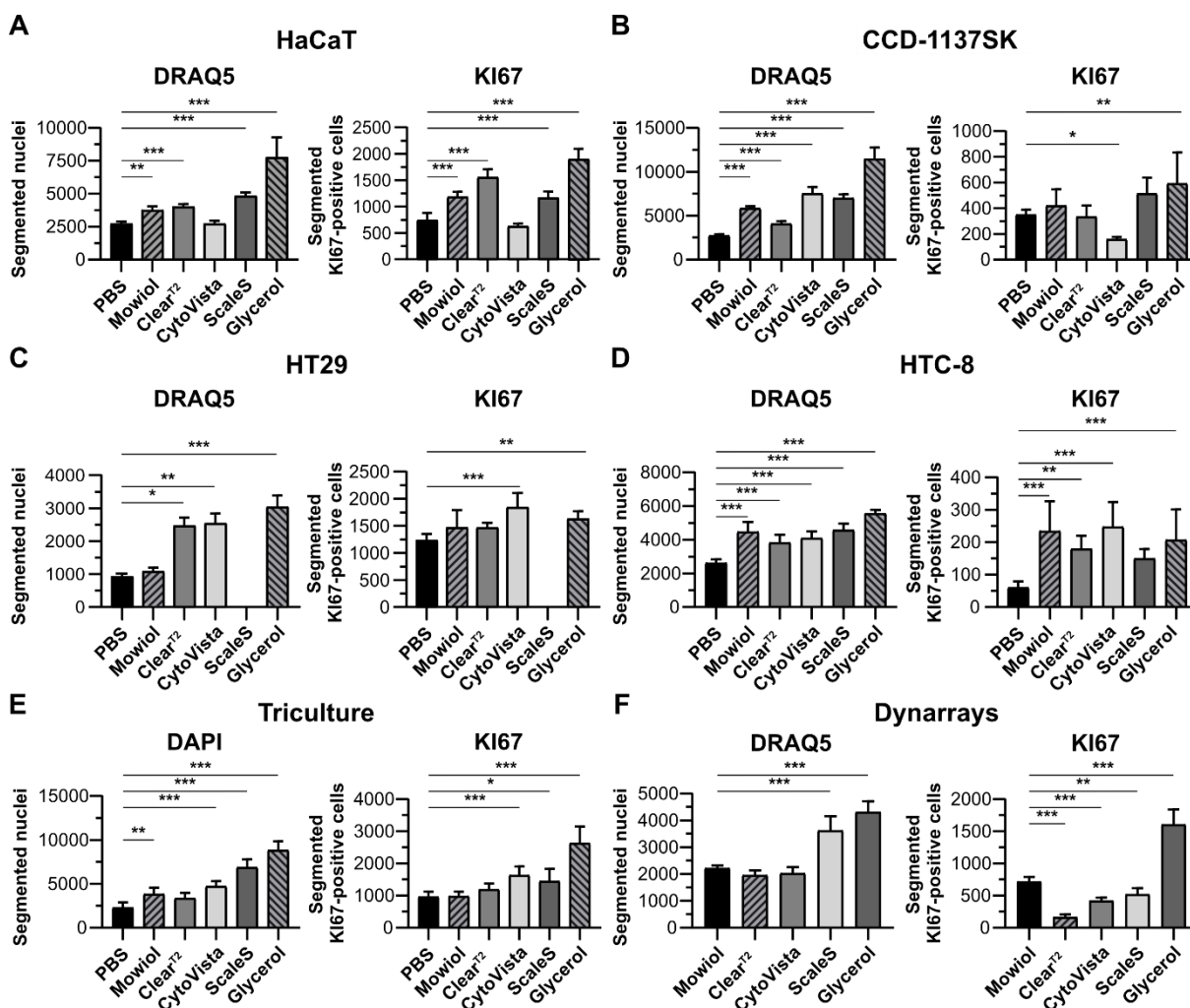


Figure 3-17: Optical clearing with glycerol consistently improves nuclear segmentation across cell lines. 3D-monoculture spheroids and complex models as indicated were PFA-fixed, fluorescently labeled with DRAQ5 and anti-KI67 antibody. Subsequently, samples were embedded in PBS or Mowiol, or optically cleared with Clear^{T2}, CytoVista, Sca/eS, or glycerol. After confocal whole mount imaging, semi-automated image segmentation was performed to detect and count DRAQ5⁺ and KI67⁺ nuclei. A-F: Quantitative analysis of DRAQ5⁺ and KI67⁺ nuclei as a function of clearing/embedding protocol. Data show mean + s.d.; n ≥ 7; *p ≤ 0.05; **p ≤ 0.01; ***p ≤ 0.001. Adapted from Nürnberg et al. (2020)²⁴⁷.

A similar effect was observed for CytoVista clearing of CCD-1137SK spheroids. In contrast to this, the same method performed best with respect to KI67 counts in HT29 samples, and equally well compared to glycerol and Mowiol for HTC-8 cells. Overall, in line with the results obtained for the depth-

dependent signal intensity and SNR measurements, glycerol clearing achieved consistently good results for all monoculture spheroids and complex 3D-cell culture models.

3.3.5 Application of z-compensation significantly improves image segmentation in glycerol cleared spheroids.

As revealed by the results shown in the previous chapters 3.2.2 - 0, optical clearing with glycerol consistently improved optical transparency and fluorescence signal intensity and SNR in depth, as well as nuclear segmentation across all tested 3D-cell culture models. However, even glycerol clearing displayed varying efficiency between cell culture models. Therefore, an attempt was made to further improve the image quality in depth by rather adjusting imaging conditions than the staining and clearing methodology. Previously analyzed confocal image stacks were acquired with constant settings and laser energy through the spatial range of the samples to ensure comparability of the obtained results. In many microscopic setups, however, imaging conditions can be dynamically adjusted to meet the requirements for generating good quality images in deeper regions. One of those settings is the z-compensation, which enables dynamic adjustment of the excitation laser energy across the imaging range. To analyze the effect of z-compensation on the in-depth image quality and subsequent nuclear segmentation, monoculture spheroids prepared from HaCaT cells were generated according to section 2.1.2, followed by fluorescent labeling with the nuclear dye DRAQ5 and anti-KI67 antibody, followed by optical clearing using glycerol immersion. Subsequently, cleared samples were subjected to confocal whole mount microscopy, where two rounds of imaging were conducted on the same samples. In the first round, non-dynamic imaging conditions were chosen, in line with the previous conducted experiments. In the second round, z-compensation was applied by linearly increasing the laser intensity with increasing imaging depth. Follow-up image quantification was performed by analyzing the depth-dependent signal intensity and SNR for both imaging conditions.

Summarized in Figure 3-18 are the results for both settings. Generated 3D-volume projections show, that even without z-compensation, good results were obtained after glycerol clearing of HaCaT spheroids (Figure 3-18A, upper panel). However, the lowest part of the sample still appeared dark and orthogonal slicing through the sample revealed incomplete capturing of the whole sample volume in deeper regions. By applying z-compensation across the imaging range, this effect was remedied across the entirety of the sample (Figure 3-18A, lower panel). Furthermore, analysis of the depth-dependent fluorescence signal intensity of DRAQ5 showed considerably less intensity loss in samples image with z-compensation across the normalized depth. In fact, intensity levels were almost constant throughout the image stack (Figure 3-18B). Similarly, the calculated SNR displayed a comparable stabilization, indicating an improved image quality in the deeper regions of the spheroids (Figure 3-18C).

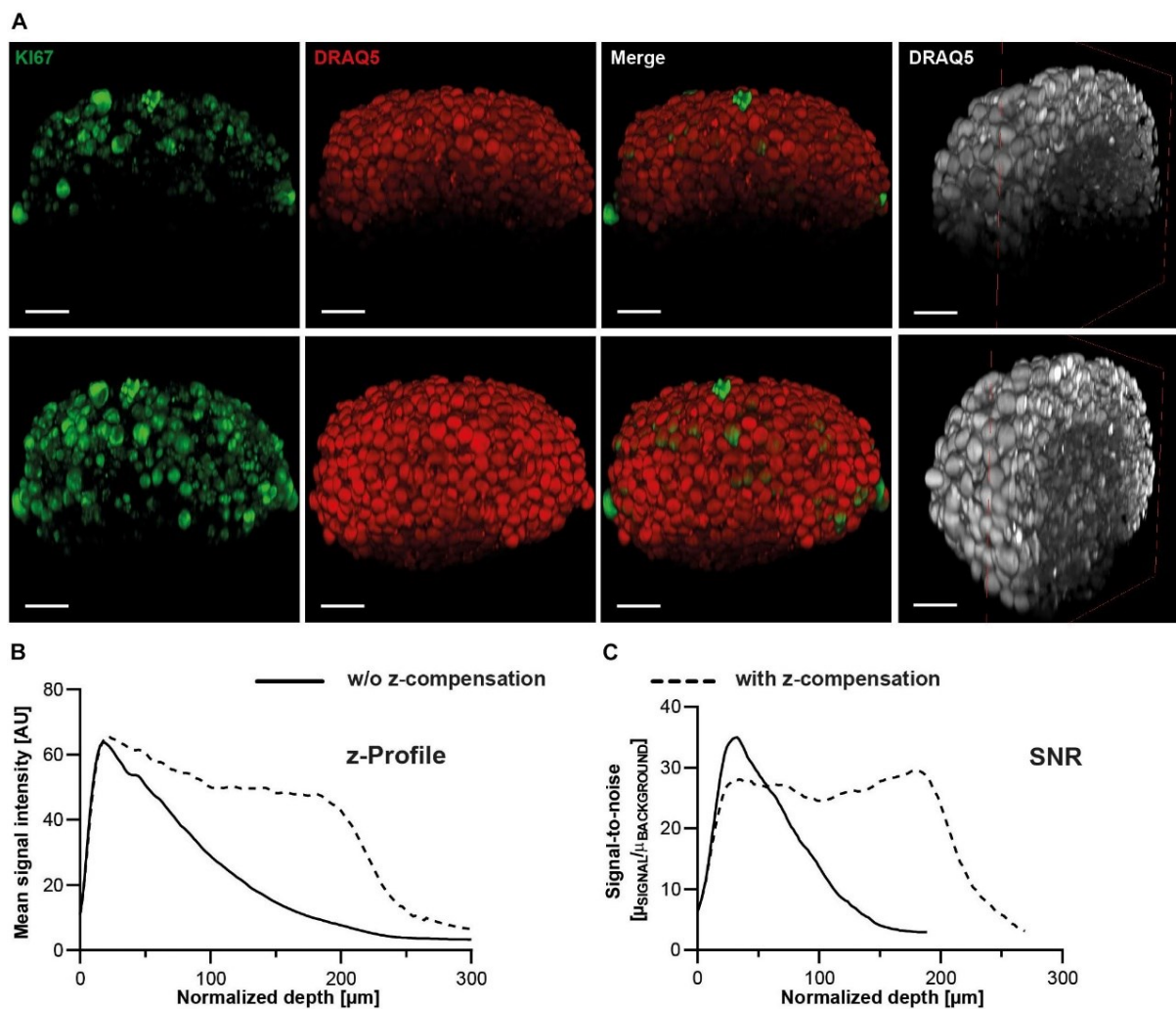


Figure 3-18: Stability of signal intensity and SNR profiles remains higher with z-compensation. U After reaching a diameter of approximately 300 μm , spheroids composed of HaCaT keratinocytes were fixed and then stained using anti-KI67 and DRAQ5. Subsequently, optical tissue clearing was performed using Glycerol, followed by whole mount microscopy using CLSM. (A) Orthogonal maximum projections (left three columns) and a clipped projection for visualizing the spheroid's core (right column) from the same spheroid, captured both without (upper panels) and with z-compensation (lower panels). In the left panels, KI67 and DRAQ5 fluorescence signals are displayed in green and red, respectively. The right panels depict DRAQ5 signals in grayscale. Scale bars 50 μm . Graphical representations of z-profiles illustrate signal intensity (B) and SNR (C) for the DRAQ5 channel the center of the spheroid. Source: Nürnberg et al. (2020)²⁴⁷.

To confirm this observation, acquired image stacks with and without z-compensation were subjected to nuclear segmentation of DRAQ5 and KI67+ cells as previously described in chapter 3.2.4 and 0^{xix}. For the purpose of comparing the two imaging conditions, the image and segmentation quality were assessed at three different depths (Figure 3-19A): firstly, results were compared at the depth where image stacks achieved their mean maximum SNR ($z = 57 \mu\text{m}$, $\text{SNR} = 27$). Secondly, an evaluation was carried out at the depth where images acquired with constant laser energy reached a Rose criterion of five ($z = 145 \mu\text{m}$), and lastly, where the SNR dropped below the cutoff value (189 μm). Results showed, that while image quality decreased with constant imaging conditions, application of z-compensation led to almost constant SNR values ($\text{SNR} = 5$ vs. $\text{SNR} = 26$, without and with z-compensation, respectively).

^{xix} Contribution from Mario Vitacolonna, see Table 8-10: Contributions from other persons, p. 117

Moreover, at a depth of 189 μm , images acquired without z-compensation displayed a dark center with few to no visible nuclei, whereas the corresponding optical sections from stacks acquired with z-compensation still displayed a SNR equal to the respective maximum. The label masks obtained from nuclear segmentation reflected the results obtained from SNR measurements. Without z-compensation and beyond 145 μm depth, nuclei located in the center of the optical section escaped the segmentation algorithm, which was not the case, when z-compensation was applied.

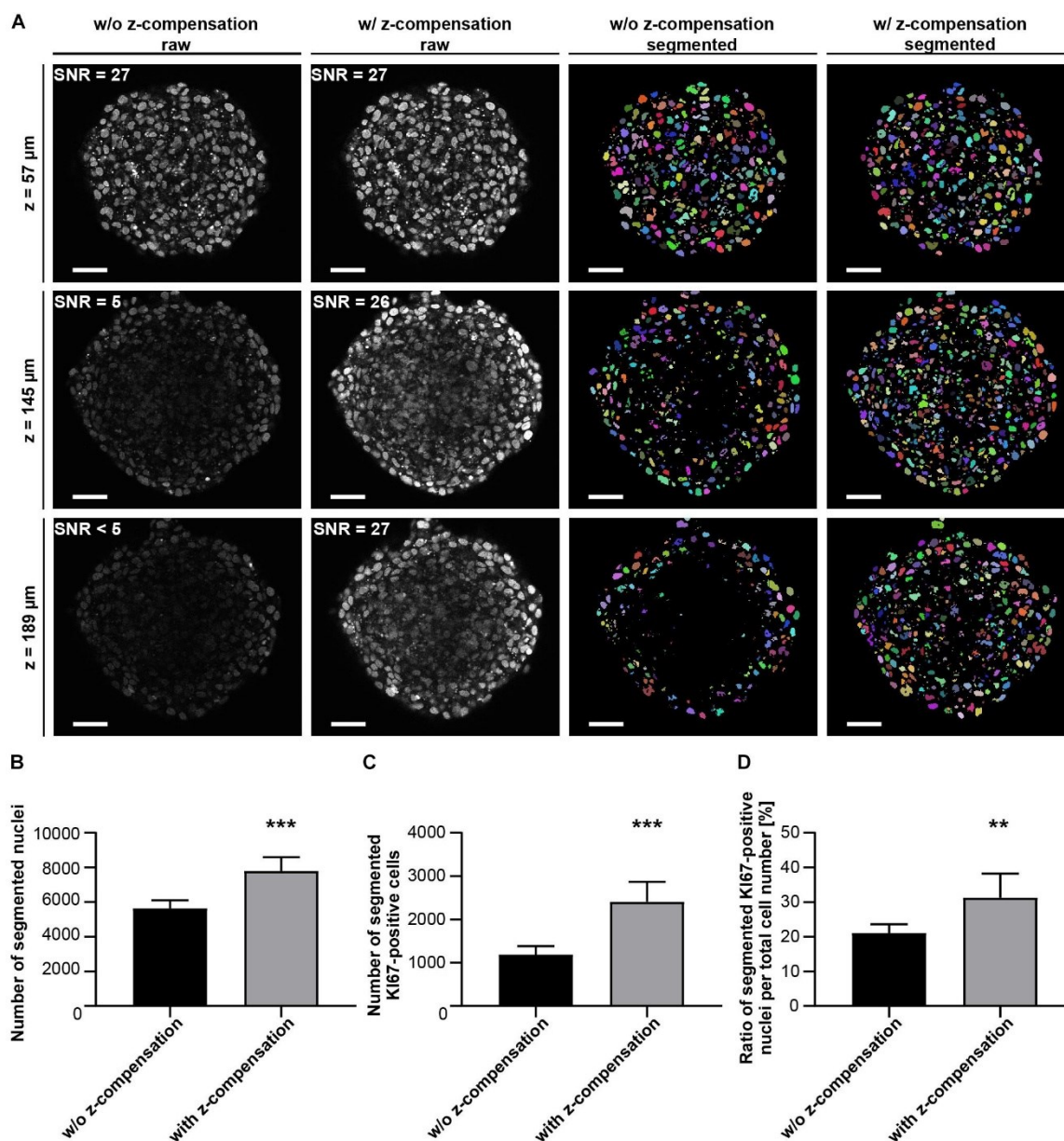


Figure 3-19: Z-compensation improves semi-automated segmentation of nuclei in glycerol cleared spheroids. After reaching a diameter of approximately 300 μm , spheroids composed of HaCaT keratinocytes were subjected to PFA-fixation and fluorescence labeling with DRAQ5 and anti-KI67 antibody. Subsequently, optical tissue clearing using Glycerol was performed, followed by confocal whole mount microscopy. (A) Figure presents individual raw confocal images (left two columns) and the corresponding segmented nuclei (right two columns) captured at various z-depths, where DRAQ5 signals are represented in grayscale, and segmented nuclei are color-coded. The image stacks were acquired with and without z-compensation, as indicated. Signal-to-Noise Ratio (SNR) values for the raw images are provided in the upper left corners. Scale bars: 50 μm . Quantitative analyses were conducted for Draq5+ nuclei (B), KI67+ nuclei (C), and the ratio of KI67+/DRAQ5+ nuclei (D) under conditions with and without z-compensation. Data show mean + s.d.; $n \geq 9$; ** $p \leq 0.01$; *** $p \leq 0.001$. Source: Nürnberg et al. (2020)²⁴⁷.

Comparing the absolute counts of segmented nuclei, quantification showed that by applying z-compensation, significantly more cells were detected by the algorithm for both DRAQ5+ (5642 vs. 7790 cells, respectively) and KI67+ cells (1188 vs. 2407 cells, respectively) (Figure 3-19B + D). More importantly, what significantly increased when applying z-compensation during confocal scanning, was the ratio of KI67+ cells to the absolute number of segmented nuclei. (21 % vs. 31 %).

4 Discussion

In recent years, the field of cell biology and biomedical research has witnessed a paradigm shift in the way we understand and study cellular behavior and responses. 2D-cell culture models, while invaluable in many respects, often fall short in replicating the complex 3D-microenvironments that cells encounter within the human body⁴⁻⁷. Features, such as increased intercellular contacts, a surrounding ECM, or chemical gradients, are not sufficiently represented by classic 2D-culture methods. To bridge this gap and gain a more accurate representation of *in vivo* conditions, 3D-cell culture models have emerged as pivotal tools in modern research⁸. These models, designed to mimic the intricate spatial and biochemical cues present in native tissue, offer a unique platform for investigating various cellular processes, disease mechanisms, drug responses, and tissue development. Moreover, the significance of 3D cell cultures becomes even more pronounced when coupled with the remarkable capabilities of hiPSCs and neuronal differentiation^{239,254-256}. Prior to the discovery of iPSC technology, *in vitro* studies on human brain cells were difficult to conduct due to the limited availability of human primary material and ethical restrictions for the use of embryonic stem cells. Human iPSCs can be derived from adult somatic cells and have the unique potential to differentiate into virtually any cell type in the human body, including cell types of the brain²⁵⁷⁻²⁵⁹. When iPSCs are directed towards neuronal differentiation within 3D culture systems, they can form complex neural networks that closely resemble the intricacies of human brain development. These 3D neuronal cultures, often called brain organoids or “mini brains”, provide an unprecedented opportunity to investigate neurodevelopmental processes, model neurological disorders, and screen potential drug candidates for their efficacy and safety^{254,255,258,259}. However, hiPSC cultivation, especially when performed in 3D, is cost-intensive, time-consuming and requires special training and high experience for cultivation^{260,261}. iPSC experiments often exhibit substantial batch-to-batch variation stemming from the intricacies of timing and cell densities required, as well as significant variability between cell lines attributed to the distinct genetic backgrounds of individual donors^{260,261}. One method to reduce experimental costs and variability, are stable hiPSC-derived NPC lines. Although these cells exhibit a more limited differentiation potential compared to iPSCs, as they primarily give rise to neurons and astrocytes, NPCs are more cost-effective to maintain and generally entail lower batch-to-batch variation in experimental outcomes^{248,252,262,263}.

However, the utilization of 3D-cell culture models in research is not without its challenges, particularly in the context of microscopy. One major obstacle is the presence of light scattering within dense 3D samples, which can obscure clarity, reduce the resolution of acquired image stacks and therefore the accuracy of quantitative measurements¹¹⁴. Optical tissue clearing is a powerful tool in modern microscopy, which aims to reduce light scattering within tissue samples. This is achieved by using specialized solutions or reagents, that homogenize the RI across the entire specimen and thereby reduce light scattering and allowing for deeper penetration of light into the sample^{114,115}. However, this technique has been predominantly applied to native tissue samples and in fact, the large variety of

protocols, which exist nowadays, have been exclusively developed for these specific types of specimens. While several studies have utilized OTC in the context of 3D cell culture models, only a limited few have focused into the diverse efficiency levels of clearing methods, with even fewer addressing variations among different cell lines within a single clearing protocol^{158,230,241,246}. Therefore, the goal of this thesis was to achieve three major objectives:

- (i) To develop a 3D-spheroid model using hiPSC-derived NPCs capable of differentiation into a diverse population of neural cells.
- (ii) To establish an effective optical clearing protocol chosen from several available procedures, enabling the analysis of these spheroids within a 3D-context.
- (iii) To apply selected OTC methods to various 3D-cell culture models of varying complexities, to gain insight into methodological variations and differences across cell lines.

The findings of this investigation and their implications will be discussed in the subsequent sections.

4.1 Generation of a 3D-spheroid model from hiPSC-derived NPCs

4.1.1 hiPSC-derived NPCs form spheroids by a self-driven mechanism

For the generation of 3D-*in vitro* models, a large variety of different methods exist in literature, ranging from simple scaffold-free techniques, like the hanging drop method or use of culture vessels with chemically modified surfaces to prevent cell adhesion (ULA plates), to complex chip-based applications, like OOACs. In the context of this project, the criteria for an appropriate cultivation method included simplicity, potential compatibility with high-throughput screening (HTS), and the capability for long-term cultivation. As previously reported, hiPSC-derived neurons require a prolonged timeframe of at least 35 – 50 days to mature and achieve a reasonably high level of functionality, which is more closely related to neuronal maturation in fetal brain development^{263,264}. During this time, frequent medium changes have to be carried out to ensure a constant nutrient supply and proper neuronal development. Therefore, microchip-based methods were not considered to be a suitable culture vessel in this project. Instead, a straightforward approach was chosen to determine whether simple scaffold-free cultivation would be sufficient to induce aggregation of B7_033#1NPC1 cells into spheroids, and whether prolonged cultivation could be carried out. Results showed that upon seeding of NPCs into ULA plates, spheroids spontaneously formed by a self-driven mechanism, independent of the seeded cell number. Furthermore, cultivation under non-differentiating conditions showed continuous growth of the spheroids with no evident disintegration of samples. Upon triggering differentiation by FGF2 withdrawal, spheroids ceased to grow and maintained an almost constant size throughout the differentiation period of 50 days. This is in concordance to findings obtained for 2D-differentiation of NPCs, where cell proliferation is strongly reduced when cells enter the post-mitotic state during differentiation²⁵². This contrasts findings by Kobolak et al. (2020)²⁶⁵. In their study, 3D-cultivation of hiPSC-derived spheroids, which were generated using the same protocol as the cell line used in this

work, continued to grow upon growth factor withdrawal over a period 42 days. In their experiments, spheroids more than doubled in size over the analyzed period of time. However, this study did not include a 3D-cultivation period prior to FGF2 withdrawal. Furthermore, although though the initial seeding numbers were identical, Kobolak et al. (2020) reported a larger spheroid size at the start of 3D-cultivation. In a study conducted by Pamies et al. (2016)²⁶⁶, NPC-derived spheroids were generated and maintained in an agitate suspension culture. Their results showed an initial growth of spheroids over a course of 17 days after changing to differentiation medium. However, in their case, spheroids maintained their size beyond this time point and did not continue to increase their size. The observed timeframe in which the spheroids grew larger is in fact comparable to the behavior displayed by B7_033#1NPC1 spheroids during the first two weeks of 3D-cultivation. This raises the question, whether the growth behavior observed in B7_033#1NPC1 spheroids was influenced by factors other than the mere removal of FGF2 from the medium. To answer this question, further experiments should be conducted. First, the sample growth should be monitored in samples, where FGF2 is removed from the culture medium directly after formation of a compact spheroid, which means on the first day after seeding. Second, spheroids should be cultured under the presence of FGF2 for an extended period of time to investigate whether continuous exposure of the growth factor affects the spheroid size in the long term. Although results on the influence of FGF2 withdrawal on spheroid growth are inconclusive, other factors can come into play with respect to the referenced studies by Kobolak et al. (2020)²⁶⁵ and Pamies et al. (2016)²⁶⁶, such as the passage number of NPCs, known to influence differentiation potential, slight variations in NPC generation protocols, and the distinct donor-specific backgrounds of iPSCs.

With respect to KI67 expression, a marker present in proliferating cells, both studies reported constant levels of KI67 throughout the first two weeks of 3D cultivation, which was followed by a rapid decrease of the marker protein. Analysis of KI67 levels in cryosections of 3D-cultured B7_033#1NPC1 spheroids revealed a similar trend, although a significant increase was measured after the first seven days. Compared to Kobolak et al. (2020)²⁶⁵, where the first analyzed timepoint was two days after spheroid formation, the earliest analysis in B7_033#1NPC1 was conducted on the first day after seeding. It is possible that aggregation and recovery of the cells from enzymatic detachment was not completed, when the samples were fixed for fluorescence labeling. Furthermore, if aggregation was insufficient, cells could have been lost during the experimental procedure.

4.1.2 3D-cultured hiPSC neural spheroids maintain constant levels of SOX2+ NPCs throughout differentiation

Human iPSC-derived NPCs, like the B7_033#1NPC1 cell line, which were generated with the method published by Falk et al. (2012)²⁶³, have been shown to differentiate into neurons of different subtypes as well as astrocytes when cultured 2D in Matrigel-coated culture dishes. To confirm whether this differentiation potential is maintained under 3D-conditions, spheroids derived from B7_033#1NPC1

cells were generated, cultivated with FGF2 over a period of two weeks, followed by a 50-day cultivation period without FGF2. Analogously to monitoring of KI67 levels, progression of neural differentiation was monitored in a weekly manner by fluorescence staining of cryosections with antibodies targeting representative marker proteins. TUBB3-expressing cells, indicating the presence of developing neurons, constituted ~25% of the total cell count within the first day after seeding, where FGF2 was still present in the medium. This ratio increased only marginally, and from d7 after growth factor withdrawal TUBB3 ratios continuously decreased. A similar trend was observed in 2D-differentiated hiPSC-derived NPCs by Horschitz et al. (2015)²⁵², however the initial fraction of TUBB3 expressing neurons was much higher (~80 – 90 %) compared to 3D-differentiated cells. In the context of 3D-differentiation of NPCs, Pamies et al. (2016)²⁶⁶ observed a similar proportion of TUBB3+ (~20 %) cells at the initiation of differentiation as observed in B7_033#1NPC1 spheroids. However, in their study, TUBB3 levels increased to ~80 % within the first two weeks of differentiation as identified by flow cytometry. Similarly, Kobolak et al. (2020)²⁶⁵ showed a time-dependent increase in the ratio of TUBB3+ pixels compared to DAPI+ pixels. However, through this quantification method, the results may not exclusively correlate with a higher count of TUBB3-expressing cells. Alternatively, they could also be attributed to an enhanced outgrowth of neurites during neuronal development. Regarding the observation of decreasing ratio of TUBB3+ cells in B7_033#1NPC1 spheroids, a possible explanation could be a time-dependent downregulation of the marker protein during maturation of neurons, as reported for cultured primary hippocampal neurons and hiPSC-derived neural spheroids^{267,268}. However, the latter study by Park et al. (2023) analyzed TUBB3 levels by RT-PCR and found a decrease of relative TUBB3 expression between week 2 and week 3 of differentiation²⁶⁸. In order to confirm whether the decreasing numbers of TUBB3+ cells was related to advanced maturation of neurons, additional marker proteins, such as NeuN, should be included in further analyses.

In contrast to TUBB3, the astrocyte marker GFAP was not observed until two weeks of differentiation and from then on, the ratio of GFAP+ cells continuously increased to a final proportion of ~22 %. This time-dependent increase is in line with findings of 2D-differentiated NPCs by Horschitz et al. (2015)²⁵², although the percentage of GFAP-expressing cells was higher towards the end of the analyzed period of time. In this study, astrocytes appeared to eventually overgrow neurons. Similarly, Kobolak et al. (2020)²⁶⁵ and Pamies et al. (2016)²⁶⁶ both reported increasing relative expression of GFAP within two to three weeks of 3D-differentiation of NPCs.

Interestingly, while the ratio of neuronal cells appeared to decrease over time, and astrocytes started to emerge at later stages of differentiation, the proportion of SOX2-positive cells did not change throughout differentiation. Instead, almost constant numbers of SOX+ cells were found, which were evenly distributed throughout the spheroid. Contrasting this, TUBB3 expression was predominantly observed in border-regions. Although a similar pattern was observed in subventricular zone-like structures of brain organoids, neural spheroids derived from NPCs display a much lower differentiation potential and level of organization.^{44,239} Considering the observed decrease in cell proliferation within 3D-cultured

NPCs, as evidenced by a lower count of KI67+ cells, the consistent ratios of SOX2+ cells suggest the presence of a steady population of quiescent cells, which neither enter neural differentiation nor engage in an active cell cycle. In literature, reports of a quiescent neural stem cell population expressing SOX2 have been documented, although it is worth noting that these findings primarily stem from studies conducted on the post-natal or adult brain^{269–271}. It is more likely, that the inactive state of SOX2+ cells residing inside the spheroids can be attributed to quiescent, nutrient-deficient zones frequently observed in spheroid structures⁵.

With respect to the phenotypic identity of the neurons in differentiated B7_033#1NPC1 spheroids, no statement can be made based on experiments conducted within the framework of this study. Studies performed on NPC lines generated based on the same protocol, however, report differentiation in to a mixture of mainly glutamatergic and GABAergic neurons, as indicated by expression levels of the vesicular glutamate transporter vGLUT1 and glutamate decarboxylase 1 (GAD1), respectively^{252,263,272}. In order to investigate whether this remains true for 3D-cultivation, further analyses of marker proteins could be conducted. The same holds true for the functionality of neurons. To confirm whether 3D-differentiated B7_033#1NPC1 cells exhibit neuronal activity, one may undertake further investigations, including electrophysiological assessments and complementary microscopy techniques such as calcium imaging or the assessment of fluorescent dye release upon high potassium depolarization^{252,273,274}.

To conclude, it has to be noted that quantitative results were obtained from fluorescently labeled cryosections, which can be prone to errors, as discussed in section 0. Especially with respect to neural cells, which exhibit a highly branched structure across larger distances, it is not possible to uniquely assign fluorescence signals from cell outgrowth to one particular cell soma. Furthermore, TUBB3+ cells were identified from label masks obtained from nuclear segmentation. However, TUBB3 is predominantly expressed in the cytoplasm. Despite the dilation of the label masks by a factor of two to encompass perinuclear regions, it is possible that some neuronal cells evaded comprehensive quantitative analysis and therefore the proportion of TUBB3+ cells might have been underestimated.

4.2 Optical clearing of hiPSC-derived neural spheroids for whole mount microscopy

Obtaining quantitative data on neural cells from cryosections can be a challenging endeavor, as mentioned in the previous section. The highly branched structures of cell protrusions and neurites can span large distances, leading to uncertainty regarding the origin of a fluorescent signal in one cryosection, which may belong to a cell body located in a different section. While computational realignment of image stacks from adjacent sections can partly reconstruct the sample volume, this process is laborious and time intensive. An alternative approach, *in toto* imaging of samples, is limited by the rapid deterioration of signal intensity and image quality as imaging depth increases. This phenomenon primarily results from the heterogeneous RIs of biological sample components, leading to substantial lateral light scattering and, consequently, reduced image resolution. To homogenize the RI of scatterers, OTC can be applied to increase the transparency of samples and therefore image quality

within deep tissue regions. However, not all available techniques are equally suited for every purpose, especially since protocols were almost exclusively developed for optical clearing of tissue. Within the framework of this thesis, the goal was to identify a suitable OTC protocol which fulfilled the following criteria: first, the method should be easy to implement into existing staining procedures without the need for specialized equipment. Therefore, simple immersion procedures were favored over tissue transformation techniques, such as CLARITY. Secondly, the method should preserve the sample integrity with minimal changes to its size. Third, the selected method should demonstrate compatibility with fluorescent dyes, antibodies, and expressed fluorescent proteins, thus guaranteeing the accurate preservation and detection of fluorescent molecules across a wide spectrum. Furthermore, the quality and resolution of acquired image stacks should be sufficient for semi-automated image segmentation. Lastly, the protocol should not include harsh chemicals, which can be hazardous to microscopes and objectives, to enable application in confocal and light sheet microscopy. Based on these criteria, Clear^{T2} ($n = 1.44$), CytoVista ($n = 1.53$), ScaleS ($n = 1.439$) and 88 % glycerol ($n = 1.459$) were chosen for evaluation of optical clearing efficiency in B7_033#1NPC1 spheroids. Clear^{T2} and ScaleS belong to the family of hyperhydrating OTC protocols^{117,157}. Where Clear^{T2} relies on a combination of formamide and PEG, without further use of detergents, ScaleS clearing is based on a series of solutions made from sorbitol, DMSO, glycerol and urea^{193,203}. Also, the latter includes Triton X-100 as a detergent to enhance clearing. CytoVista, a commercially available clearing solution, falls within the category of organic solvent-based clearing agents^{117,157}. Despite the historical challenges associated with the partial compatibility of this group of protocols with fluorescence proteins, it was included in the panel of clearing protocols due to its user-friendly nature and the manufacturer's claimed compatibility with fluorescent molecules^{179,180}. Finally, despite demonstrating only modest optical clearing capabilities, an 88% glycerol solution with adjusted refractive index was chosen, primarily because of its versatility in accommodating a wide range of fluorescent molecules and its frequent utilization as an immersion medium in microscopy^{189,190}.

4.2.1 Aqueous hyperhydration with ScaleS preserves sample dimensions

Alterations in sample volume induced by clearing can serve specific purposes. For instance, techniques like expansion microscopy rely on increasing sample dimensions to resolve objects that typically fall below the optical resolution limit²⁷⁵. However, this approach comes with significant increases in the time, resources, and storage space required for imaging and data processing. Moreover, expansion microscopy may potentially impact sample or epitope integrity. Conversely, sample shrinkage may offer advantages in terms of saving time in scanning and image processing¹⁷⁶. Nevertheless, it carries the risk of compromising spatial resolution and making automated quantification of densely packed structures more challenging²⁷⁶. Hence, in most scenarios, preserving the original sample volume is the preferred choice, prioritizing considerations such as quantification accuracy, reproducibility, and sample integrity. Analysis of sample size preservation upon optical clearing revealed substantial differences between

OTC protocols. While PFA-fixation and PBS-embedding did not affect the original sample volume, embedding in Mowiol caused significant shrinkage of the spheroids. This was not unexpected, since Mowiol is a PVA-based medium, which hardens over time and causes dehydration of the sample^{277,278}. Surprisingly, Clear^{T2} caused extensive sample shrinkage compared to PBS-embedded controls, which was not expected, since hyperhydration-based clearing techniques are known to usually perform well with respect to sample size preservation. In fact, the development of these protocols were initially driven by the motivation to keep sample changes to a minimum^{114,117,157}. Furthermore, the comparative study by Boutin et al. (2014)¹⁵⁸ in primary neural stem cell spheres (~100 μm) showed no significant difference in size upon Clear^{T2} clearing to controls. Similar results were obtained by Kabadi et al. (2016)²³², where no effect of Clear^{T2} on sample size was detected for spheroids of a human lung epithelial cell line (~100 μm). Silva et al. (2021)²⁷⁹ tested the influence on agitation conditions during clearing of spheroids of human dermal fibroblasts (~390 μm) and reported no significant changes upon Clear^{T2} clearing. However, the phase contrast images presented in the study did not match the presented quantification data. Instead, they rather imply a tendency towards sample shrinkage. Contradicting these studies, Diosdi et al. (2021)²⁴⁵ reported shrinkage upon Clear^{T2} clearing for three different human cancer cell lines (~250 μm), although it was not reported to which extent this change of sample size was observed. Overall, since the size and type of samples used in these studies all varied, differences in sample preservation can likely be attributed to cell-line dependent differences. The strongest impact of clearing on sample size was observed upon CytoVista clearing, with a shrinkage of more than 40 % compared to PBS-embedded samples. Such an effect has not been reported before. However, previous studies utilizing CytoVista predominantly did not place a significant focus on evaluating the effects of the clearing process on the sample, resulting in a lack of reported information regarding alterations in sample size²⁸⁰⁻²⁸². The highest degree of spheroid size preservation was observed upon Sca/eS clearing. According to literature, this protocol was not applied previously to 3D-cell culture models, however, related protocols using simple immersion in Sca/eS4 suggest similar performance of the method with respect to sample size preservation²⁸³. For glycerol clearing, no significant changes compared to PBS-controls were detected, although a small trend towards swelling was measured. However, glycerol is generally included in protocols to counteract hyperhydration, due to its dehydrating properties and therefore this trend can most likely be attributed to statistical variations^{114,196}.

4.2.2 Optical clearing with glycerol enhances light penetration into hiPSC-derived neural spheroids and image quality in depth

As mentioned in the previous section, alterations of the sample size are not imperative to insufficient optical clearing. Therefore, confocal image stacks from embedded and optically cleared B7_033#1NPC1 spheroids were subjected to a more detailed examination of fluorescence signal intensity and SNR with respect to the imaging depth. For this, pixel intensities of two nuclear dyes were analyzed through the center of the spheroids and plotted against the imaging depth. However, due to the

observed shrinkage upon Mowiol embedding, Clear^{T2} and CytoVista clearing, depth values had to be normalized to the percentage of sample volume change. Otherwise, differences between the intensity profiles could have been obscured by the spatial dimension of the samples. For this reason, both, the absolute and normalized imaging depth, were considered for protocol evaluation. Evaluation was made according to the following criteria: the depth at which 90 % of the maximum signal intensity is lost (90 % signal loss) and the depth for reaching a SNR of 5, which corresponds to the Rose criterion.

Regarding the preservation of nuclear dyes and anti-KI67 staining, all the protocols successfully maintained the fluorescence and results were comparable between DAPI and DRAQ5.

For DAPI, which has a short excitation wavelength in the UV range, the normalized signal decay revealed no major differences between clearing methods, although a strong increase of the maximum signal intensity was detected upon CytoVista clearing. For the far-red emitting dye DRAQ5, such an effect was not observed. For all clearing protocols, the normalized depth for the 90 % signal loss cutoff was determined to range between 208 – 222 μm (DAPI) and 158.2 – 237.2 μm (DRAQ5). With respect to the absolute imaging depth however, glycerol showed the highest degree of sample transparency, resulting in an absolute imaging depth for DAPI of 237 μm and 227 μm for DRAQ5. CytoVista clearing displayed the strongest decay of signal intensity across the absolute depth. However, considering sample shrinkage, which led to an average size of ~ 170 μm , and an absolute depth for the 90 % signal loss criterion of ~ 120 μm , CytoVista still performed well in comparison to other methods. Calculated SNR values were overall lower for DAPI than for DRAQ5, which can be attributed to a lower background fluorescence in the longer wavelength range. In contrast to the pure depth-dependent signal intensity, the SNR can give additional information on the image quality and resolution inside the sample. Calculation of the SNR confirmed superiority of glycerol clearing over other OTC protocols, displaying an absolute depth for meeting the Rose criterion of 201 μm and 266 μm , for DAPI and DRAQ5, respectively.

Overall, results obtained from fluorescence decay analyses were in line with the available literature, although a comparison has to be made carefully, since cell lines and sample sizes vary across studies.

Clear^{T2} has been applied in a variety of *in vitro* studies^{158,230,231,233}. Boutin et al. (2014) analyzed primary neural stem cell spheres of ~ 100 μm size and showed fluorescence signals upon Clear^{T2} clearing across the whole range¹⁵⁸. Although other studies by the same group applied Clear^{T2} to larger spheroids (~ 200 – 300 μm), only maximum projections of image stacks were shown, which does not allow for direct comparison of depth-dependent signal intensities^{230,231}.

The protocol of ScaleS clearing, which was used within the framework of this thesis, had not been previously applied to *in vitro* samples according to the literature. However, modified versions have been used to clear samples of different cell types with sample sizes between 100 – 150 μm . In the previously mentioned study by Boutin et al. (2014)¹⁵⁸, ScaleA2 was included in their selection of clearing protocols. Much like Clear^{T2}, ScaleA2 substantially enhanced sample transparency, enabling the detection of fluorescence signals throughout the entire depth. However, according to their criteria ScaleA2 was not

considered for further experiments due to induced sample swelling. In a later study, Boutin et al. (2018) used optical clearing with *ScaleS4*, which is the final solution used for imaging in the *ScaleS* protocol, in T47D and U87 spheroids (~ 150 - $300 \mu\text{m}$)²⁸³. Here, simple immersion in *ScaleS4* solution achieved imaging depths of $\sim 150 \mu\text{m}$. Observations made in B7_033#1NPC1 spheroids cleared with the original *ScaleS* protocol, show a higher absolute depth of $215 \mu\text{m}$ according to the 90 % signal loss cutoff. This indicates that optical transparency is not only influenced by the RI-matching solution, but also by the preceding staining protocol and cell line.

According to my results as presented here, clearing with 88 % glycerol showed to be the most effective protocol among the tested methods, with respect to the absolute imaging depth. This is supported by Steinberg et al. (2020), who tested different glycerol-based immersion protocols on pancreatic cancer spheroids²²⁸. Among the tested methods were 100 % glycerol, 85 % glycerol and RapiClear, which is a commercially available clearing solution with a RI close to that of pure glycerol ($n = 1.47$). Their results show a comparable imaging depth of $\sim 200 \mu\text{m}$ for all the tested methods. However, due to its lower cost and reduced viscosity compared to pure glycerol, they deemed 85% glycerol to be the most suitable option.

It has to be noted that although a clear trend among the applied clearing protocols emerged regarding intensity and SNR measurements, a rapid decay of both parameters across the imaging depth was still evident. Especially the latter indicates a rapid decrease of image quality, which can affect downstream quantitative analysis. In this work, this problem was addressed by adjusting imaging conditions by linear z-compensation, and it will be discussed in detail in section 4.3.3.

4.2.3 Optical clearing with glycerol and *ScaleS* enable semi-automated segmentation of entire hiPSC-derived spheroids

Analyzing the extent to which clearing protocols enhance imaging depth and quality is equally significant as testing whether these improvements translate into enhanced segmentation. Ultimately, whole mount microscopy should not only be used to generate representative images, but also quantitative information in a 3D-context. Yet, manual image segmentation in 3D remains a time-consuming process, and its consistency can vary when multiple researchers perform the same analysis. Automated segmentation algorithms are therefore the preferred method of choice. However, these algorithms need a high degree of image quality in order to detect fluorescent signals reliably and accurately. Ultimately, OTC serves to enhance sample transparency to a degree, where meaningful biological information can be obtained in a 3D-context. Therefore, whole mount image stacks obtained from optically cleared B7_033#1NPC1 samples were subjected to a semi-automatic segmentation algorithm previously published by Schmitz et al. (2017)²¹⁶. This particular method was chosen because it incorporates a user-friendly GUI, making it accessible to researchers who may not have a robust programming background.

Overall, segmentation results of optically cleared hiPSC-derived NPCs matched the previously acquired data from depth-dependent intensity and SNR analysis. Among protocols, glycerol immersion and *ScaleS* clearing displayed the most promising outcomes, showing the highest count of segmented nuclei and KI67+ cells. Nevertheless, both methods exhibited substantial variability in the segmentation of DRAQ5, while *ScaleS* displayed notable variation between samples in terms of KI67 segmentation. However, in all tested conditions, a decrease in segmentation quality was observed with increasing depth, even at SNR values above the Rose criterion. This was especially prominent in the core region of the spheroids. Here, label masks appeared fragmented and oversegmented with increasing depth. One reason for this is the round shape of the samples, leading to thinner layers of scattering material covering the peripheral areas compared to the core regions. The 3D-seeded watershed algorithm used for segmentation operates on variations in signal brightness. Diffuse and incomplete edges arising from poor image quality, as observed in B7_033#1NPC1 spheroids, can hinder precise and consistent object detection, particularly when nuclear staining is not uniformly distributed^{247,284,285}. Moreover, the settings applied during segmentation were fine-tuned to ensure robust segmentation in the upper levels of the samples, where SNR values and intensities were considerably higher. Therefore, with increasing depth and decreasing SNR, the same settings exhibited diminished performance²⁴⁷. To enhance image segmentation within these regions, one can employ mathematical operations like adaptive histogram equalization during pre-processing. Additionally, the implementation of deep learning methods, which depend on signal intensity to a lesser degree compared to the approach utilized in this study, has the potential to significantly enhance image segmentation across the z-range²⁸⁶⁻²⁸⁸. For a thorough evaluation of segmentation quality, it is advisable to contrast the obtained results with manually segmented ground truth data. This comparative analysis facilitates the calculation of more precise metrics such as precision, recall, and F-Score, which greatly assist in assessing the overall quality of segmentation^{246,283}. Another method to remedy intensity and SNR variations across image stacks, is the application of z-compensation during imaging, which will be discussed in section 4.3.3.

4.2.4 Combining optical clearing with glycerol and LSFM enables 3D-microscopy of entire neural spheroids

To conclude investigations on suitable optical clearing protocols for spheroids made from hiPSC-derived spheroids, optical clearing of glycerol was applied to differentiating spheroids. Previous analyses performed in this study revealed decreasing counts of TUBB3+ cells over time and a delayed increase of GFAP+ cells. Therefore, an intermediate timepoint (d35 of differentiation) was chosen to visualize both cell types. Additionally, the axonal marker tau, somatodendritic marker Map2a and NPC marker nestin were included in the staining panel. Differing from previous experiments, images were acquired with LSFM instead of CLSM owing to its superior imaging capabilities and suitability for larger sample sizes. Results showed that by combining glycerol clearing with LSFM, visualization of DAPI fluorescence was possible across a range of ~600 μm . Furthermore, all antibodies tested were

compatible with glycerol clearing and did not display substantial signal loss. Regarding the signal distribution of TUBB3 and GFAP observed in cryosections, whole mount microscopy confirmed enhanced TUBB3 localization in the periphery and a more uniform distribution of GFAP⁺ cells throughout the spheroids. Moreover, imaging revealed the intricate, highly branched networks of the two cell types, which was not visible in cryosections. Similarly, stainings of tau, Map2a and nestin showed extensive network formation across the surface of the samples. Moreover, partial separation of tau and Map2a signals imply polarization of cells and progressing maturation of developing neurons^{289,290}.

4.3 Comparison of OTC protocols across cell lines

To further investigate whether comparable results can be achieved with glycerol clearing in other *in vitro* systems or if similar variability as observed with optical clearing across different tissues is displayed, the analysis pipeline employed for optical clearing of hiPSC-derived spheroids was also applied to additional 3D-cell culture models. In more detail, four monoculture spheroid models were investigated, which were prepared from keratinocytes, human fibroblasts, colorectal cancer cells or a human tongue cell line. Furthermore, a larger, more complex triculture model of skin cancer was included, as well as a chip-based coculture model of breast cancer cells and fibroblasts. Additionally, fluorescent CellTracker dyes and an ECFP-expressing cell line was included to extend analyses of dye compatibility with clearing protocols.

4.3.1 Sample size preservation, optical transparency and image quality vary across cell lines

With respect to sample size preservation, all spheroid models displayed a similar trend among the tested clearing and embedding methods. In more detail, sample shrinkage was observed upon Mowiol embedding, and optical clearing with either Clear^{T2} or CytoVista, whereas good preservation of the sample size was observed for ScaleS and glycerol clearing. An increase of the sample volume, as observed in B7_033#1NPC1 spheroids, was not detected in any other cell culture model, supporting the interpretation of sample swelling upon glycerol clearing as random fluctuations. The strongest effect across all cell lines was consistently observed upon CytoVista clearing. Although the overall trend upon optical clearing appeared to be comparable across monoculture spheroids, the degree of swelling or shrinkage varied between cell lines. In particular, the colorectal cancer cell line HT29 and human tongue cell line HTC-8 were less prone to shrinkage, compared to other spheroids. The same two cell lines showed only minor improvement of sample transparency and depth-dependent SNR with respect to the nuclear dye DAPI. With respect to the Rose criterion, all tested protocols reached SNR < 5 at depths less than 90 μm in these spheroids. In contrast to this, fluorescence signal intensity and SNR of DRAQ5 was not observed to suffer from the same loss. Overall, CytoVista clearing enhanced the maximum DAPI signal intensity, as observed in B7_033#1NPC1, independent of the cell line. Regarding fluorescence intensity and SNR profiles, while minor variations were noted among the cell lines and

protocols, still the most favorable outcomes were consistently obtained using either *ScaleS* or glycerol. This observation indicates that these two methods can serve as reliable starting points when assessing optical clearing in 3D cell culture models. Although, given that optical clearing with *ScaleS* involves considerably more reagents and incubation times, glycerol clearing might be preferred due to the simplicity of the method. Upon evaluation of the findings in this study, it can be concluded that there is no single superior protocol for optical clearing of 3D-cell culture models. Much like how protocols are selected for optical clearing of tissue, considering factors like tissue type, size, and fluorescent labels, the same thoughtful considerations should be applied when working with 3D *in vitro* models. With respect to current literature, similar effects have been reported regarding the variability of optical clearing protocols across 3D-cell cultures of different origin. Unfortunately, although several studies report these variations in their data, only few of them address this observation^{116,158,225,228,241}. The most comprehensive study on this topic was published by Diosdi et al. (2020 and 2021)^{245,246}. Their results on three different cell lines and five clearing techniques clearly support the observations made within the framework of this thesis, that there does not seem to be a gold standard for optical clearing of 3D-cell culture models. Instead, OTC protocols should be evaluated for each cell line and experimental setting with respect to the research question.

Nuclear segmentation of whole mount images show strong variations between cell lines and clearing protocols. While overall, high counts of DRAQ5+ and KI67+ nuclei were detected upon glycerol clearing, all results have to be interpreted with caution. As previously discussed in section 4.2.3, intensity-based segmentation algorithms, like the 3D-seeded watershed algorithm applied in this study, are prone to error, when image stacks suffer from non-uniform intensity and SNR in x-, y-, and z-direction. This effect can be even more pronounced in densely packed structures, such as spheroids, where spatially close nuclei often appear as overlapping structures, potentially resulting in inadequate separation at nuclear borders leading to undersegmentation^{248,285,286}. Furthermore, this effect becomes even more pronounced in the presence of sample shrinkage. Consequently, the reduced number of detected cells following Clear^{T2} or CytoVista clearing, as observed in some of the tested cell lines, is likely attributable to this phenomenon. One way to improve the uniformity of signal intensity and SNR across dimensions is the implementation of linear z-compensation into the imaging process and it will be discussed in section 4.3.3.

4.3.2 Optical tissue clearing efficiency is challenged by the complexity of 3D-cell culture models

Among the analyzed 3D-cell culture methods, two *in vitro* systems of higher complexity were included to extend analyses beyond monoculture spheroids. First, evaluation of a triculture model of skin cancer, which was comprised of fibroblasts, CellTracker Red-labeled keratinocytes, and CellTracker Green-labeled melanoma cells was performed. While the maximum intensity values of DAPI exhibited variations similar to those in monoculture spheroids, it was notable that the absolute depths at which the 90% signal loss and Rose criterion were met were considerably lower. In terms of SNR profiles, none

of the applied clearing techniques reached values exceeding a depth of 90 μm . Notably, two of the three cell lines within the triculture model were also individually analyzed as monoculture spheroids, and in this context, significantly greater cutoff depths were attained. Similarly, in a chip-based Dynarray coculture of ECFP-expressing breast cancer cells and human fibroblasts, none of the clearing methods achieved a depth for reaching the Rose criterion beyond 116 μm . Although ScaleS and glycerol clearing again performed better than other protocols in both complex models, optical clearing was overall impaired. With respect to fluorophore preservation, all methods appeared to affect fluorescence intensity of CellTracker Green, while CellTracker Red did not display major differences. Fluorescence of ECFP was decreased for all clearing methods, with the exception of glycerol and Mowiol embedding. In particular upon Clear^{T2} clearing, fluorescence was almost completely abolished, leading to the conclusion, that this method is incompatible with ECFP. A similar impact of Clear^{T2} on fluorescent proteins has been previously documented in the literature for tissue sections and has been attributed to the high formamide concentrations inherent to this technique^{291,292}.

In conclusion, analysis of the two models revealed that the complexity of a model is an additional factor which has to be considered when selecting a clearing protocol for a particular *in vitro* system²⁴⁷.

4.3.3 Implementation of z-compensation into the imaging process improves data segmentation in optically cleared spheroids

As previously described in section 4.2.3 and 4.3.2., semi-automated image segmentation applied in this study was impaired by rapidly declining signal intensities and SNR values beyond a certain depth. Furthermore, optimizing segmentation parameters for high SNR values led to a notable increase in faulty segmentation of fluorescence signals in deeper regions of the samples, resulting in instances of both over- and undersegmentation. To increase uniformity of signal intensity and SNR across the z-range, imaging parameters were adjusted to include a linear, stepwise increase of the excitation laser energy with increasing depth. Through the application of this technique, known as "z-compensation," the image quality in deeper sample regions was significantly enhanced, resulting in nearly uniform profiles for depth-dependent signal intensity and SNR. This enhanced image quality is evident in the segmentation results, which exhibited considerable improvements in deeper sample layers following z-compensation²⁴⁷. In addition to the overall increased counts of nuclei and KI67+ cells, a change of the ratio for the respective labels further emphasized the importance of uniform image quality upon segmentation. The quantification of nuclei and proliferating or apoptotic cells plays a crucial role in drug testing, serving as a means to assess drug efficacy. However, relying on assessments derived from incomplete or erroneous segmentations due to varying image qualities can lead to misleading conclusions. For a comprehensive assessment of segmentation quality, it is recommended to compare the obtained results with manually segmented ground truth data. This comparative approach enables the calculation of more refined metrics like precision, recall, and F-Score, which contribute significantly to the evaluation of overall segmentation quality.

4.4 Conclusion and outlook

In this thesis, I have demonstrated the successful transition from 2D-cultivation of hiPSC-derived NPCs to a scaffold-free 3D-cultivation method, forming compact spheroids. The cell line utilized in this study exhibits remarkable scalability, with the ability to be expanded, frozen, and thawed for multiple passages. This feature not only ensures cost-effective generation of human neurons *in vitro* but also eliminates the need for concurrent maintenance culture of hiPSCs. Using this cultivation method, differentiation into a mixture of neurons and astrocytes can be carried out in 3D and samples can be kept in culture for over 60 days. The presented model was characterized with respect to 3D-proliferation, apoptosis and neural differentiation and showed to be a suitable option for *in vitro* studies on neuronal differentiation and method establishment for hiPSC-derived neurons. Moving forward, further investigations are necessary to delve deeper into the functionality of neural cells within these models, including assessments of excitability and synaptic activity in developing neurons. Additionally, a more comprehensive analysis of neuronal subtypes can provide insights into specific characteristics of the model, given the inherent variability in hiPSC-derived cells. For the same reason, similar analyses should be performed with NPC-lines from different donors to investigate the influence of donor-specific genetic backgrounds.

In response to the challenges posed by traditional cryosectioning for the analysis of neurons in 3D-cultures, several optical clearing protocols were assessed for their suitability in whole-mount confocal (CLSM) and light-sheet microscopy (LSFM). Among the protocols tested, the most favorable results were achieved through immersion in an 88% aqueous glycerol solution with a refractive index (RI) of 1.459. This immersion protocol can be seamlessly incorporated into established staining procedures, requiring no specialized equipment, and preserving sample dimensions exceptionally well. Importantly, compatibility was observed with commonly used nuclear dyes, expressed fluorescent proteins, live cell labeling dyes, and selected antibodies for labeling proteins associated with neural lineage commitment and proliferation. Glycerol's non-toxic properties make it a suitable choice for immersion in both CLSM, with imaging depths of up to approximately 250–300 μm , and LSFM, with depths of around 600 μm . The resulting whole-mount image stacks can be subjected to automated image segmentation, providing reliable results for the upper sample regions. This reliability can be extended to greater depths through z-compensation adjustments made during the imaging process. This protocol offers researchers an additional valuable tool for enhancing microscopy analyses of 3D-cell culture models in a manner which is non-destructive to the sample. As glycerol is a commonly available laboratory chemical, no additional compounds are necessary. Moreover, RI of the solution can be tailored to suit the microscope setup by adjusting the glycerol or water content within the clearing solution. In the future, the quality of segmentation should be assessed by comparing it to manually segmented ground truth data, allowing for the calculation of metrics such as precision, recall, and F-score.

Comparative analysis of different optical clearing protocols across 3D-cell cultures of varying complexity revealed high variability between the different models with respect to fluorescence signal

preservation, maximum signal intensity and SNR. The results show that inherent characteristics of cell lines influence the outcome of optical clearing and that protocols for optical clearing should be chosen in a sample-dependent manner. Factors to consider include size, cellular density, complexity and composition of 3D cultures, and compatibility with the necessary fluorophores. Before committing to a particular clearing protocol, it is advisable to conduct tests on several methods to assess clearing efficiency and select the most suitable approach for the intended application. The methods examined in this thesis encompass four simple immersion protocols: Clear^{T2}, CytoVista, ScaleS, and glycerol, each exhibiting varying degrees of efficacy concerning the criteria mentioned and which should be taken into account when choosing optical clearing procedures. However, other protocols which are reported in literature are interesting approaches and report good results in optical clearing of *in vitro* cell culture systems. A more in-depth exploration of the specific molecular composition of 3D-*in vitro* models can provide further insights into the reasons behind the varying efficiency of certain clearing protocols. This knowledge can help narrow down the selection of protocols to be tested for optical clearing efficiency.

5 Summary

3D cell cultures are a significant advancement in cell biology, providing a more physiologically relevant environment compared to traditional 2D cultures. One notable application involves the neural differentiation of human induced pluripotent stem cells (hiPSCs) into complex 3D structures, like brain organoids, which closely resemble fetal brain development and are able to recapitulate complex processes in the human brain. While these models hold great promise for studying human brain development and diseases, they pose several challenges: a high level of expertise is necessary to generate these cultures, they are expensive to maintain, and exhibit a high variability between cell lines and experiments. In contrast, stable neural precursor cells (NPCs) derived from hiPSCs, while possessing lower differentiation potential and complexity, offer a more practical and consistent method for generating human neural cells *in vitro*.

Unfortunately, the microscopic analysis of 3D-cultures presents difficulties owing to the intricate, extensively branched structure of neural cells, which span considerable distances, rendering it challenging to extract comprehensive information solely from cryosectioning techniques. One viable approach for analyzing these models involves whole mount confocal laser scanning microscopy (CLSM), which utilizes the intact sample for 3D visualization. However, optical effects, such as lateral light scattering due to refractive index (RI) mismatches prevent the generation of high-quality images beyond imaging depths of ~ 50 μm . Optical tissue clearing (OTC) techniques are a means to overcome these limitations by homogenizing the RI across the sample and enabling image acquisition at high resolution deep into biological specimens. Although OTC protocols have been thoroughly examined in tissue, their application was seldom extended to *in vitro* systems. In the limited studies conducted on this topic, a substantial variation in optical clearing efficiency is observed across different methods and cell lines, indicating the absence of a universal gold standard in this field of research.

The presented work describes the establishment of a 3D-spheroid model of hiPSC-derived NPCs, which can be generated in low attachment microwell plates, and which can be differentiated into a mixture of neurons and astrocytes. The differentiation process was monitored in cryosections over an extended time period of 50 days for marker proteins indicative of proliferation, apoptosis, as well as neuronal and astroglial differentiation. The results show a constant growth of spheroids over a period of two weeks, which correlated with KI67-expression level. Markers for young neurons were already present at the start of 3D-cultivation, whereas astrocytes emerged at a later differentiation state. While proportions of neural cells changed over time, a steady pool of SOX2⁺ NPCs was maintained throughout the cultivation period.

Furthermore, a range of optical tissue clearing methods were established and evaluated for their effectiveness in clearing hiPSC-derived NPC spheroids. Specifically, Clear^{T2}, CytoVista, ScaleS, and an 88% glycerol solution were tested to determine their capacity to maintain sample size while enhancing optical transparency. This assessment was conducted through a depth-dependent analysis of

signal intensity and signal-to-noise ratio (SNR), as well as suitability for semi-automated image segmentation of nuclear signals. Although results showed the highest degree of spheroid size preservation upon ScaleS clearing, remaining analyses confirm superiority of glycerol clearing with respect to optical transparency and image quality. Furthermore, in addition to optical clearing of undifferentiated hiPSC-derived neural spheroids, glycerol clearing was applied to differentiated spheroids which were then subjected to light sheet fluorescence microscopy (LSFM). This confirmed the method's applicability to both undifferentiated and differentiated 3D samples.

In the light of high variability of optical clearing efficiency in 3D-*in vitro* systems reported in literature, Clear^{T2}, CytoVista, ScaleS, and 88% glycerol were applied to additional cell culture models of varying complexity. These included four monoculture spheroid models, one complex tri-culture model of skin cancer and a chip-based co-culture model. Obtained results show a high degree of variability between the respective methods and cell culture models with respect to fluorescent dye preservation and optical transparency. Overall, optical clearing with glycerol proved to be the most reliable method across all models, although clearing efficiency was generally affected by the complexity of the cell culture model. Furthermore, application of linear z-compensation during imaging substantially improved image segmentation by stabilizing signal intensity and SNR across the sample dimensions.

6 Zusammenfassung

3D-Zellkulturen stellen einen bedeutenden Fortschritt in der Zellbiologie dar und bieten im Vergleich zu traditionellen 2D-Kulturen oftmals eine physiologischere Umgebung. Eine hervorzuhebende Anwendung ist die neuronale Differenzierung menschlicher induzierter pluripotenter Stammzellen (hiPSCs) in komplexe 3D-Strukturen wie Gehirnorganoide, die der Entwicklung des fetalen Gehirns stark ähneln und in der Lage sind, komplexe Prozesse im menschlichen Gehirn nachzubilden. Diese Modelle sind zwar vielversprechend für die Untersuchung von Krankheiten und der Entwicklung des menschlichen Gehirns, stellen jedoch auch mehrere Herausforderungen dar. Für die Herstellung dieser Kulturen ist ein hohes Maß an Expertise erforderlich, die Kultivierung ist teuer und die Variabilität zwischen Zelllinien und Experimenten ist hoch. Im Gegensatz dazu bieten stabile neurale Vorläuferzellen (NPCs), die von hiPSCs abgeleitet sind, zwar ein geringeres Differenzierungspotenzial und eine geringere Komplexität, aber auch eine kosteneffizientere und konsistentere Methode zur Erzeugung menschlicher neuronaler Zellen *in vitro*.

Die Analyse von neuronalen 3D-Kulturen mit Hilfe von Mikroskopie gestaltet sich jedoch schwierig. Die komplexe Struktur von neuronalen Zellen, deren feine Verzweigungen sich durch das ganze Sphäroid erstrecken können, macht es nahezu unmöglich räumliche Informationen mit Hilfe traditioneller Methoden wie Kryoschnitten abzubilden. Ein praktikablerer Ansatz ist die gesamtheitliche *in toto*-Analyse dieser Modelle mittels konfokaler Laser-Scanning-Mikroskopie (CLSM). Jedoch verhindern optische Effekte wie laterale Lichtstreuung aufgrund von Unterschieden im Brechungsindex (RI) die Erzeugung hochwertiger Bilddaten jenseits von Tiefen von etwa 50 μm . Techniken zur optischen Gewebeklärun (OTC) bieten Möglichkeiten, diese Einschränkungen zu überwinden, indem sie den RI im gesamten Probenmaterial homogenisieren und die Aufnahme hochauflösender Bilder tief in biologischen Proben ermöglichen. Obwohl OTC-Protokolle in Geweben umfassend untersucht wurden, wird ihre Anwendung selten auf *in vitro* Systeme übertragen. In den begrenzten Studien zu diesem Thema wurde eine erhebliche Variation in der optischen Klärungseffizienz zwischen verschiedenen Methoden und Zelllinien festgestellt, was darauf hindeutet, dass es in diesem Forschungsbereich keinen universellen Goldstandard gibt.

Die vorliegende Arbeit beschreibt die Etablierung eines 3D-Sphäroidmodells aus hiPSC-abgeleiteten NPCs, welches zu einer Mischung aus Neuronen und Astrozyten differenziert werden kann. Der Differenzierungsprozess wurde in Kryoschnitten über einen Zeitraum von 50 Tagen überwacht und umfasste die Analyse von Markerproteinen für Proliferation, Apoptose sowie neuronale und astrogliale Differenzierung. Die Ergebnisse zeigten ein ständiges Wachstum der Sphäroide über einen Zeitraum von zwei Wochen hinweg, welches mit dem KI67-Expressionsniveau korrelierte. Marker für junge Neuronen waren bereits zu Beginn der 3D-Kultivierung nachweisbar, während Astrozyten in einem späteren Differenzierungsstadium auftraten. Trotz der sich ändernden Anteile von neuronalen Zellen im

Laufe der Zeit blieb eine konstante Population von SOX2⁺ NPCs während des gesamten Kultivierungszeitraums erhalten.

Darüber hinaus wurden eine Reihe von optischen Gewebeklärungsmethoden etabliert und auf ihre Wirksamkeit bei der Klärung von hiPSC-abgeleiteten NPC-Sphäroiden hin untersucht. Konkret wurden Clear^{T2}, CytoVista, ScaleS und eine 88%ige Glycerinlösung auf ihre Fähigkeit getestet, die Sphäroidgröße zu erhalten und die optische Transparenz zu verbessern. Diese Bewertung wurde durch eine tiefenabhängige Analyse der Signalintensität und des Signal-Rausch-Verhältnisses (SNR), sowie der Eignung für die halbautomatische Bildsegmentierung von Zellkernsignalen durchgeführt. Obwohl ScaleS-Klärung im Hinblick auf die Erhaltung der Sphäroidgröße optimale Resultate erzielen konnte, bestätigen die verbleibenden Analysen die Überlegenheit der Glycerin-Klärung in Bezug auf optische Transparenz und Bildqualität. Darüber hinaus wurde, zusätzlich zur optischen Klärung von undifferenzierten hiPSC-abgeleiteten neuronalen Sphäroiden, die Glycerin-Klärung auf differenzierte Sphäroide angewendet und diese mittels Lichtblattmikroskopie (LSFM) untersucht. Diese zusätzlichen Experimente bestätigten die Anwendbarkeit der Methode auf sowohl undifferenzierte als auch differenzierte 3D-Proben.

Angesichts der hohen Variabilität der optischen Klärungseffizienz in 3D-in-vitro-Systemen, wurden Clear^{T2}, CytoVista, ScaleS und 88% Glycerin auf zusätzliche Zellkulturmodelle unterschiedlicher Komplexität angewendet. Diese umfassten vier weitere Monokultur-Sphäroid-Modelle, ein komplexes Trikultur-Modell und ein Chip-basiertes Co-Kultur-Modell. Die erzielten Ergebnisse zeigen einen hohen Grad an Variabilität zwischen den jeweiligen Methoden und Zellkulturmodellen in Bezug auf die Erhaltung von Fluoreszenzfarbstoffen und optische Transparenz. Insgesamt erwies sich die optische Klärung mit Glycerin als die zuverlässigste Methode für alle Modelle, wobei die Kläreffizienz insgesamt von der Komplexität des Zellkulturmodells beeinflusst wurde. Darüber hinaus konnte die Anwendung der linearen Z-Kompensation während der Bildaufnahme die Segmentierung erheblich verbessern, indem sie die Signalintensität und das Signal-Rausch-Verhältnis (SNR) über die Abmessungen der Probe stabilisierte.

7 References

1. Jedrzejczak-Silicka M: History of Cell Culture. In: *New Insights into Cell Culture Technology*, edited by Gowder SJT, InTech, 2017
2. Arrowsmith J, Miller P: Trial watch: phase II and phase III attrition rates 2011-2012. *Nature reviews. Drug discovery* 12(8): 569, 2013
3. Langhans SA: Three-Dimensional in Vitro Cell Culture Models in Drug Discovery and Drug Repositioning. *Frontiers in pharmacology* 9: 6, 2018
4. Baker BM, Chen CS: Deconstructing the third dimension: how 3D culture microenvironments alter cellular cues. *Journal of Cell Science* 125(Pt 13): 3015–24, 2012
5. Duval K, Grover H, Han L-H, Mou Y, Pegoraro AF, Fredberg J, Chen Z: Modeling Physiological Events in 2D vs. 3D Cell Culture. *Physiology* 32(4): 266–77, 2017
6. Breslin S, O'Driscoll L: Three-dimensional cell culture: the missing link in drug discovery. *Drug Discovery Today* 18(5-6): 240–9, 2013
7. Knight E, Przyborski S: Advances in 3D cell culture technologies enabling tissue-like structures to be created in vitro. *J. Anat.* 227(6): 746–56, 2015
8. Breslin S, O'Driscoll L: The relevance of using 3D cell cultures, in addition to 2D monolayer cultures, when evaluating breast cancer drug sensitivity and resistance. *Oncotarget* 7(29): 45745–56, 2016
9. Florczyk SJ, Kievit FM, Wang K, Erickson AE, Ellenbogen RG, Zhang M: 3D Porous Chitosan-Alginate Scaffolds Promote Proliferation and Enrichment of Cancer Stem-Like Cells. *J. Mater. Chem. B* 4(38): 6326–34, 2016
10. Pineda ET, Nerem RM, Ahsan T: Differentiation patterns of embryonic stem cells in two- versus three-dimensional culture. *Cells Tissues Organs* 197(5): 399–410, 2013
11. Melissaridou S, Wiechec E, Magan M, Jain MV, Chung MK, Farnebo L, Roberg K: The effect of 2D and 3D cell cultures on treatment response, EMT profile and stem cell features in head and neck cancer. *Cancer Cell Int* 19(1): 16, 2019
12. Vantangoli MM, Madnick SJ, Huse SM, Weston P, Boekelheide K: MCF-7 Human Breast Cancer Cells Form Differentiated Microtissues in Scaffold-Free Hydrogels. *PLoS ONE* 10(8): e0135426, 2015
13. Lagies S, Schlimpert M, Neumann S, Wäldin A, Kammerer B, Borner C, Peintner L: Cells grown in three-dimensional spheroids mirror in vivo metabolic response of epithelial cells. *Commun Biol* 3(1): 246, 2020
14. Voss AK, Strasser A: The essentials of developmental apoptosis. *FI000Research* 9, 2020
15. Gumbiner BM, Kim N-G: The Hippo-YAP signaling pathway and contact inhibition of growth. *Journal of Cell Science* 127(Pt 4): 709–17, 2014
16. Pavel M, Renna M, Park SJ, Menzies FM, Ricketts T, Füllgrabe J, Ashkenazi A, Frake RA, Lombarte AC, Bento CF, Franze K, Rubinsztein DC: Contact inhibition controls cell survival and proliferation via YAP/TAZ-autophagy axis. *Nature communications* 9(1): 2961, 2018
17. Riwaldt S, Corydon TJ, Pantalone D, Sahana J, Wise P, Wehland M, Krüger M, Melnik D, Kopp S, Infanger M, Grimm D: Role of Apoptosis in Wound Healing and Apoptosis Alterations in Microgravity. *Frontiers in bioengineering and biotechnology* 9: 679650, 2021
18. Wilkinson HN, Hardman MJ: Wound healing: cellular mechanisms and pathological outcomes. *Open biology* 10(9): 200223, 2020
19. Yamaguchi Y, Miura M: Programmed cell death in neurodevelopment. *Developmental cell* 32(4): 478–90, 2015
20. Evan GI, Vousden KH: Proliferation, cell cycle and apoptosis in cancer. *Nature* 411(6835): 342–8, 2001
21. Harrison RG: The outgrowth of the nerve fiber as a mode of protoplasmic movement. *J. Exp. Zool.* 9(4): 787–846, 1910
22. Hurrell T, Ellero AA, Masso ZF, Cromarty AD: Characterization and reproducibility of HepG2 hanging drop spheroids toxicology in vitro. *Toxicology in vitro an international journal published in association with BIBRA* 50: 86–94, 2018

23. Mueller D, Koetemann A, Noor F: Organotypic Cultures of Hepg2 Cells for In Vitro Toxicity Studies. *J Bioengineer & Biomedical Sci* 01(S2), 2011
24. Takahashi Y, Hori Y, Yamamoto T, Urashima T, Ohara Y, Tanaka H: 3D spheroid cultures improve the metabolic gene expression profiles of HepaRG cells. *Bioscience reports* 35(3), 2015
25. Amaral RLF, Miranda M, Marcato PD, Swiech K: Comparative Analysis of 3D Bladder Tumor Spheroids Obtained by Forced Floating and Hanging Drop Methods for Drug Screening. *Frontiers in physiology* 8: 605, 2017
26. Hsiao AY, Tung Y-C, Qu X, Patel LR, Pienta KJ, Takayama S: 384 hanging drop arrays give excellent Z-factors and allow versatile formation of co-culture spheroids. *Biotechnology and Bioengineering* 109(5): 1293–304, 2012
27. Kelm JM, Timmins NE, Brown CJ, Fussenegger M, Nielsen LK: Method for generation of homogeneous multicellular tumor spheroids applicable to a wide variety of cell types. *Biotechnology and Bioengineering* 83(2): 173–80, 2003
28. Raghavan S, Ward MR, Rowley KR, Wold RM, Takayama S, Buckanovich RJ, Mehta G: Formation of stable small cell number three-dimensional ovarian cancer spheroids using hanging drop arrays for preclinical drug sensitivity assays. *Gynecologic oncology* 138(1): 181–9, 2015
29. Timmins NE, Dietmair S, Nielsen LK: Hanging-drop multicellular spheroids as a model of tumour angiogenesis. *Angiogenesis* 7(2): 97–103, 2004
30. Timmins NE, Nielsen LK: Generation of multicellular tumor spheroids by the hanging-drop method. *Methods in molecular medicine* 140: 141–51, 2007
31. Tung Y-C, Hsiao AY, Allen SG, Torisawa Y, Ho M, Takayama S: High-throughput 3D spheroid culture and drug testing using a 384 hanging drop array. *The Analyst* 136(3): 473–8, 2011
32. Barros AS, Costa EC, Nunes AS, Melo-Diogo D de, Correia IJ: Comparative study of the therapeutic effect of Doxorubicin and Resveratrol combination on 2D and 3D (spheroids) cell culture models. *International journal of pharmaceutics* 551(1-2): 76–83, 2018
33. Cesarz Z, Tamama K: Spheroid Culture of Mesenchymal Stem Cells. *Stem cells international* 2016: 9176357, 2016
34. Hundsberger H, Stierschneider A, Sarne V, Ripper D, Schimon J, Weitzenböck HP, Schild D, Jacobi N, Eger A, Atzler J, Klein CT, Wiesner C: Concentration-Dependent Pro- and Antitumor Activities of Quercetin in Human Melanoma Spheroids: Comparative Analysis of 2D and 3D Cell Culture Models. *Molecules (Basel, Switzerland)* 26(3), 2021
35. Yue X, Lukowski JK, Weaver EM, Skube SB, Hummon AB: Quantitative Proteomic and Phosphoproteomic Comparison of 2D and 3D Colon Cancer Cell Culture Models. *Journal of proteome research* 15(12): 4265–76, 2016
36. Keller F, Bruch R, Clauder F, Hafner M, Rudolf R: Extracellular Matrix Components Regulate Bone Sialoprotein Expression in MDA-MB-231 Breast Cancer Cells. *Cells* 10(6), 2021
37. Keller F, Rudolf R, Hafner M: Towards optimized breast cancer 3D spheroid mono- and co-culture models for pharmacological research and screening. *JCB* 5(2): 89–101, 2019
38. Klicks J, Maßlo C, Kluth A, Rudolf R, Hafner M: A novel spheroid-based co-culture model mimics loss of keratinocyte differentiation, melanoma cell invasion, and drug-induced selection of ABCB5-expressing cells. *BMC cancer* 19(1): 402, 2019
39. Lazzari G, Nicolas V, Matsusaki M, Akashi M, Couvreur P, Mura S: Multicellular spheroid based on a triple co-culture: A novel 3D model to mimic pancreatic tumor complexity. *Acta biomaterialia* 78: 296–307, 2018
40. Meier-Hubberten JC, Sanderson MP: Establishment and Analysis of a 3D Co-Culture Spheroid Model of Pancreatic Adenocarcinoma for Application in Drug Discovery. *Methods in molecular biology (Clifton, N.J.)* 1953: 163–79, 2019
41. Yakavets I, Francois A, Benoit A, Merlin J-L, Bezdetnaya L, Vogin G: Advanced co-culture 3D breast cancer model for investigation of fibrosis induced by external stimuli: optimization study. *Scientific reports* 10(1): 21273, 2020
42. Giandomenico SL, Sutcliffe M, Lancaster MA: Generation and long-term culture of advanced cerebral organoids for studying later stages of neural development. *Nature protocols* 16(2): 579–602, 2021

43. Kumar SV, Er PX, Lawlor KT, Motazedian A, Scurr M, Ghobrial I, Combes AN, Zappia L, Oshlack A, Stanley EG, Little MH: Kidney micro-organoids in suspension culture as a scalable source of human pluripotent stem cell-derived kidney cells. *Development (Cambridge, England)* 146(5), 2019
44. Lancaster MA, Renner M, Martin C-A, Wenzel D, Bicknell LS, Hurles ME, Homfray T, Penninger JM, Jackson AP, Knoblich JA: Cerebral organoids model human brain development and microcephaly. *Nature* 501(7467): 373–9, 2013
45. Morizane R, Bonventre JV: Generation of nephron progenitor cells and kidney organoids from human pluripotent stem cells. *Nature protocols* 12(1): 195–207, 2017
46. Uchimura K, Wu H, Yoshimura Y, Humphreys BD: Human Pluripotent Stem Cell-Derived Kidney Organoids with Improved Collecting Duct Maturation and Injury Modeling. *Cell reports* 33(11): 108514, 2020
47. Cui X, Hartanto Y, Zhang H: Advances in multicellular spheroids formation. *Journal of the Royal Society, Interface* 14(127), 2017
48. Carmona-Fontaine C, Bucci V, Akkari L, Deforet M, Joyce JA, Xavier JB: Emergence of spatial structure in the tumor microenvironment due to the Warburg effect. *Proceedings of the National Academy of Sciences of the United States of America* 110(48): 19402–7, 2013
49. Lee SY, Ju MK, Jeon HM, Jeong EK, Lee YJ, Kim CH, Park HG, Han SI, Kang HS: Regulation of Tumor Progression by Programmed Necrosis. *Oxidative medicine and cellular longevity* 2018: 3537471, 2018
50. Wang L-T, Proulx M-È, Kim AD, Lelarge V, McCaffrey L: A proximity proteomics screen in three-dimensional spheroid cultures identifies novel regulators of lumen formation. *Scientific reports* 11(1): 22807, 2021
51. Dikovsky D, Bianco-Peled H, Seliktar D: The effect of structural alterations of PEG–fibrinogen hydrogel scaffolds on 3-D cellular morphology and cellular migration. *Biomaterials* 27(8): 1496–506, 2006
52. Gao G, Hubbell K, Schilling AF, Dai G, Cui X: Bioprinting Cartilage Tissue from Mesenchymal Stem Cells and PEG Hydrogel. *Methods in molecular biology (Clifton, N.J.)* 1612: 391–8, 2017
53. Hilderbrand AM, Ford EM, Guo C, Sloppy JD, Kloxin AM: Hierarchically structured hydrogels utilizing multifunctional assembling peptides for 3D cell culture. *Biomaterials science* 8(5): 1256–69, 2020
54. Nam S, Stowers R, Lou J, Xia Y, Chaudhuri O: Varying PEG density to control stress relaxation in alginate-PEG hydrogels for 3D cell culture studies. *Biomaterials* 200: 15–24, 2019
55. Dou X, Li P, Schönherr H: Three-Dimensional Microstructured Poly(vinyl alcohol) Hydrogel Platform for the Controlled Formation of Multicellular Cell Spheroids. *Biomacromolecules* 19(1): 158–66, 2018
56. Lamponi S, Leone G, Consumi M, Nelli N, Magnani A: Porous multi-layered composite hydrogel as cell substrate for in vitro culture of chondrocytes. *International Journal of Polymeric Materials and Polymeric Biomaterials* 70(11): 764–73, 2021
57. Molyneaux K, Wnek MD, Craig SEL, Vincent J, Rucker I, Wnek GE, Brady-Kalnay SM: Physically-cross-linked poly(vinyl alcohol) cell culture plate coatings facilitate preservation of cell-cell interactions, spheroid formation, and stemness. *Journal of biomedical materials research. Part B, Applied biomaterials* 109(11): 1744–53, 2021
58. Ma S, Rong M, Lin P, Bao M, Xie J, Wang X, Huck WTS, Zhou F, Liu W: Fabrication of 3D Tubular Hydrogel Materials through On-Site Surface Free Radical Polymerization. *Chem. Mater.* 30(19): 6756–68, 2018
59. Passos MF, Carvalho NMS, Rodrigues AA, Bavaresco VP, Jardini AL, Maciel MRW, Maciel Filho R: PHEMA Hydrogels Obtained by Infrared Radiation for Cartilage Tissue Engineering. *International Journal of Chemical Engineering* 2019: 1–9, 2019
60. Zhao W, Shi Z, Chen X, Yang G, Lenardi C, Liu C: Microstructural and mechanical characteristics of PHEMA-based nanofibre-reinforced hydrogel under compression. *Composites Part B: Engineering* 76: 292–9, 2015
61. Sun T, Mai S, Norton D, Haycock JW, Ryan AJ, MacNeil S: Self-organization of skin cells in three-dimensional electrospun polystyrene scaffolds. *Tissue engineering* 11(7-8): 1023–33, 2005
62. Unal AZ, West JL: Synthetic ECM: Bioactive Synthetic Hydrogels for 3D Tissue Engineering. *Bioconjugate chemistry* 31(10): 2253–71, 2020
63. Griffith LG, Swartz MA: Capturing complex 3D tissue physiology in vitro. *Nature reviews. Molecular cell biology* 7(3): 211–24, 2006

-
64. Nicolas J, Magli S, Rabbachin L, Sampaolesi S, Nicotra F, Russo L: 3D Extracellular Matrix Mimics: Fundamental Concepts and Role of Materials Chemistry to Influence Stem Cell Fate. *Biomacromolecules* 21(6): 1968–94, 2020
 65. Bonnans C, Chou J, Werb Z: Remodelling the extracellular matrix in development and disease. *Nature reviews. Molecular cell biology* 15(12): 786–801, 2014
 66. Frantz C, Stewart KM, Weaver VM: The extracellular matrix at a glance. *Journal of Cell Science* 123(Pt 24): 4195–200, 2010
 67. Hynes RO, Naba A: Overview of the matrisome--an inventory of extracellular matrix constituents and functions. *Cold Spring Harbor perspectives in biology* 4(1): a004903, 2012
 68. Naba A, Clauser KR, Hoersch S, Liu H, Carr SA, Hynes RO: The matrisome: in silico definition and in vivo characterization by proteomics of normal and tumor extracellular matrices. *Molecular & cellular proteomics MCP* 11(4): M111.014647, 2012
 69. Hynes RO: The extracellular matrix: not just pretty fibrils. *Science (New York, N.Y.)* 326(5957): 1216–9, 2009
 70. Brown TE, Anseth KS: Spatiotemporal hydrogel biomaterials for regenerative medicine. *Chemical Society reviews* 46(21): 6532–52, 2017
 71. Deo KA, Singh KA, Peak CW, Alge DL, Gaharwar AK: Bioprinting 101: Design, Fabrication, and Evaluation of Cell-Laden 3D Bioprinted Scaffolds. *Tissue engineering. Part A* 26(5-6): 318–38, 2020
 72. Moroni L, Burdick JA, Highley C, Lee SJ, Morimoto Y, Takeuchi S, Yoo JJ: Biofabrication strategies for 3D in vitro models and regenerative medicine. *Nature reviews. Materials* 3(5): 21–37, 2018
 73. Ozbolat IT, Hospodiuk M: Current advances and future perspectives in extrusion-based bioprinting. *Biomaterials* 76: 321–43, 2016
 74. Daly AC, Prendergast ME, Hughes AJ, Burdick JA: Bioprinting for the Biologist. *Cell* 184(1): 18–32, 2021
 75. Wang Y, Li J, Li Y, Yang B: Biomimetic bioinks of nanofibrillar polymeric hydrogels for 3D bioprinting. *Nano Today* 39: 101180, 2021
 76. Jeon S, Heo J-H, Kim MK, Jeong W, Kang H-W: High-Precision 3D Bio-Dot Printing to Improve Paracrine Interaction between Multiple Types of Cell Spheroids. *Advanced functional materials* 30(52): 2005324, 2020
 77. Lee H, Kim J, Choi Y, Cho D-W: Application of Gelatin Bioinks and Cell-Printing Technology to Enhance Cell Delivery Capability for 3D Liver Fibrosis-on-a-Chip Development. *ACS biomaterials science & engineering* 6(4): 2469–77, 2020
 78. Lin NYC, Homan KA, Robinson SS, Kolesky DB, Duarte N, Moisan A, Lewis JA: Renal reabsorption in 3D vascularized proximal tubule models. *Proceedings of the National Academy of Sciences of the United States of America* 116(12): 5399–404, 2019
 79. Morley CD, Ellison ST, Bhattacharjee T, O'Bryan CS, Zhang Y, Smith KF, Kabb CP, Sebastian M, Moore GL, Schulze KD, Niemi S, Sawyer WG, Tran DD, Mitchell DA, Sumerlin BS, Flores CT, Angelini TE: Quantitative characterization of 3D bioprinted structural elements under cell generated forces. *Nature communications* 10(1): 3029, 2019
 80. Skylar-Scott MA, Uzel SGM, Nam LL, Ahrens JH, Truby RL, Damaraju S, Lewis JA: Biomanufacturing of organ-specific tissues with high cellular density and embedded vascular channels. *Science advances* 5(9): eaaw2459, 2019
 81. Song KH, Highley CB, Rouff A, Burdick JA: Complex 3D-Printed Microchannels within Cell-Degradable Hydrogels. *Advanced functional materials* 28(31): 1801331, 2018
 82. Surendran V, Rutledge D, Colmon R, Chandrasekaran A: A novel tumor-immune microenvironment (TIME)-on-Chip mimics three dimensional neutrophil-tumor dynamics and neutrophil extracellular traps (NETs)-mediated collective tumor invasion. *Biofabrication*, 2021
 83. van Duinen V, Trietsch SJ, Joore J, Vulto P, Hankemeier T: Microfluidic 3D cell culture: from tools to tissue models. *Current opinion in biotechnology* 35: 118–26, 2015
 84. Young EWK, Beebe DJ: Fundamentals of microfluidic cell culture in controlled microenvironments. *Chemical Society reviews* 39(3): 1036–48, 2010
 85. Ataç B, Wagner I, Horland R, Lauster R, Marx U, Tonevitsky AG, Azar RP, Lindner G: Skin and hair on-a-chip: in vitro skin models versus ex vivo tissue maintenance with dynamic perfusion. *Lab on a chip* 13(18): 3555–61, 2013
-

-
86. Trietsch SJ, Israëls GD, Joore J, Hankemeier T, Vulto P: Microfluidic titer plate for stratified 3D cell culture. *Lab on a chip* 13(18): 3548–54, 2013
 87. Wagner I, Materne E-M, Brincker S, Süßbier U, Frädrieh C, Busek M, Sonntag F, Sakharov DA, Trushkin EV, Tonevitsky AG, Lauster R, Marx U: A dynamic multi-organ-chip for long-term cultivation and substance testing proven by 3D human liver and skin tissue co-culture. *Lab on a chip* 13(18): 3538–47, 2013
 88. Del Piccolo N, Shirure VS, Bi Y, Goedegebuure SP, Gholami S, Hughes CCW, Fields RC, George SC: Tumor-on-chip modeling of organ-specific cancer and metastasis. *Advanced drug delivery reviews* 175: 113798, 2021
 89. Gjorevski N, Ranga A, Lutolf MP: Bioengineering approaches to guide stem cell-based organogenesis. *Development (Cambridge, England)* 141(9): 1794–804, 2014
 90. Gupta A, Lutolf MP, Hughes AJ, Sonnen KF: Bioengineering in vitro models of embryonic development. *Stem cell reports* 16(5): 1104–16, 2021
 91. Han S, Yan J-J, Shin Y, Jeon JJ, Won J, Jeong HE, Kamm RD, Kim Y-J, Chung S: A versatile assay for monitoring in vivo-like transendothelial migration of neutrophils. *Lab on a chip* 12(20): 3861–5, 2012
 92. Havins L, Capel A, Christie SD, Lewis MP, Roach P: Gradient biomimetic platforms for neurogenesis studies. *Journal of neural engineering*, 2021
 93. Verbridge SS, Chakrabarti A, DelNero P, Kwee B, Varner JD, Stroock AD, Fischbach C: Physicochemical regulation of endothelial sprouting in a 3D microfluidic angiogenesis model. *Journal of biomedical materials research. Part A* 101(10): 2948–56, 2013
 94. Kim S, Lee H, Chung M, Jeon NL: Engineering of functional, perfusable 3D microvascular networks on a chip. *Lab on a chip* 13(8): 1489–500, 2013
 95. Lee H, Kim S, Chung M, Kim JH, Jeon NL: A bioengineered array of 3D microvessels for vascular permeability assay. *Microvascular research* 91: 90–8, 2014
 96. Lee SH, Shim KY, Kim B, Sung JH: Hydrogel-based three-dimensional cell culture for organ-on-a-chip applications. *Biotechnology progress* 33(3): 580–9, 2017
 97. Sanderson J (ed): *Understanding Light Microscopy*, Wiley, 2019
 98. Basic Microscope Optics. In: *Understanding Light Microscopy*, edited by Sanderson J, Wiley, 2019, pp 55–74
 99. Optical Aberrations of the Microscope. In: *Understanding Light Microscopy*, edited by Sanderson J, Wiley, 2019, pp 101–125
 100. *The Evolution of the Microscope*, Elsevier, 1967
 101. BRADBURY S: THE FIRST MICROSCOPES. In: *The Evolution of the Microscope*, Elsevier, 1967, pp 1–35
 102. BRADBURY S: SIMPLE OR SINGLE-LENS MICROSCOPES. In: *The Evolution of the Microscope*, Elsevier, 1967, pp 68–103
 103. Kubitscheck U (ed): *Fluorescence Microscopy*, Weinheim, Germany, Wiley-VCH Verlag GmbH & Co. KGaA, 2017
 104. Conchello J-A, Lichtman JW: Optical sectioning microscopy. *Nature methods* 2(12): 920–31, 2005
 105. Minsky M: Memoir on inventing the confocal scanning microscope. *Scanning* 10(4): 128–38, 1988
 106. Diffraction and Interference in Image Formation. In: *Fundamentals of Light Microscopy and Electronic Imaging*, edited by Murphy DB, Davidson MW, Hoboken, NJ, USA, John Wiley & Sons, Inc, 2012, pp 79–101
 107. Murphy DB, Davidson MW (eds): *Fundamentals of Light Microscopy and Electronic Imaging*, Hoboken, NJ, USA, John Wiley & Sons, Inc, 2012
 108. Herbert S, Soares H, Zimmer C, Henriques R: Single-molecule localization super-resolution microscopy: deeper and faster. *Microscopy and microanalysis the official journal of Microscopy Society of America, Microbeam Analysis Society, Microscopical Society of Canada* 18(6): 1419–29, 2012
 109. The Microscope Objective. In: *Understanding Light Microscopy*, edited by Sanderson J, Wiley, 2019, pp 127–160
 110. Light. In: *Understanding Light Microscopy*, edited by Sanderson J, Wiley, 2019, pp 29–54
-

-
111. Dobrucki JW, Kubitscheck U: Fluorescence Microscopy. In: *Fluorescence Microscopy*, edited by Kubitscheck U, Weinheim, Germany, Wiley-VCH Verlag GmbH & Co. KGaA, 2017, pp 85–132
 112. Kvapilová V: Evaluation of microwave drying effects on historical brickwork and modern building materials. *IOP Conf. Ser.: Mater. Sci. Eng.* 867(1): 12026, 2020
 113. Zhernovaya O, Sydoruk O, Tuchin V, Douplik A: The refractive index of human hemoglobin in the visible range. *Physics in medicine and biology* 56(13): 4013–21, 2011
 114. Richardson DS, Lichtman JW: Clarifying Tissue Clearing. *Cell* 162(2): 246–57, 2015
 115. Richardson DS, Lichtman JW: SnapShot: Tissue Clearing. *Cell* 171(2): 496–496.e1, 2017
 116. Costa EC, Silva DN, Moreira AF, Correia IJ: Optical clearing methods: An overview of the techniques used for the imaging of 3D spheroids. *Biotechnology and Bioengineering* 116(10): 2742–63, 2019
 117. Silvestri L, Costantini I, Sacconi L, Pavone FS: Clearing of fixed tissue: a review from a microscopist's perspective. *Journal of Biomedical Optics* 21(8): 81205, 2016
 118. Tuchin VV, Maksimova IL, Zimnyakov DA, Kon IL, Mavlyutov AH, Mishin AA: Light propagation in tissues with controlled optical properties. *Journal of Biomedical Optics* 2(4): 401–17, 1997
 119. Tuchin VV: Tissue optics, light distribution, and spectroscopy. *Opt. Eng.* 33(10): 3178, 1994
 120. Khan R, Gul B, Khan S, Nisar H, Ahmad I: Refractive index of biological tissues: Review, measurement techniques, and applications. *Photodiagnosis and photodynamic therapy* 33: 102192, 2021
 121. Gul B, Ashraf S, Khan S, Nisar H, Ahmad I: Cell refractive index: Models, insights, applications and future perspectives. *Photodiagnosis and photodynamic therapy* 33: 102096, 2021
 122. ASCENZI A, FABRY C: Technique for dissection and measurement of refractive index of osteones. *The Journal of biophysical and biochemical cytology* 6(1): 139–42, 1959
 123. Bacallao R, Sohrab S, Phillips C: Guiding Principles of Specimen Preservation for Confocal Fluorescence Microscopy. In: *Handbook of biological confocal microscopy*, 3rd ed., edited by Pawley JB, New York, NY, Springer, 2006, pp 368–380
 124. Stritzel J, Rahlves M, Roth B: Refractive-index measurement and inverse correction using optical coherence tomography. *Optics letters* 40(23): 5558–61, 2015
 125. Acerbo AS, Carr GL, Judex S, Miller LM: Imaging the material properties of bone specimens using reflection-based infrared microspectroscopy. *Analytical chemistry* 84(8): 3607–13, 2012
 126. Dou L, Zhang Y, Sun H: Advances in Synthesis and Functional Modification of Nanohydroxyapatite. *Journal of Nanomaterials* 2018: 1–7, 2018
 127. Meng Z, Yao XS, Yao H, Liang Y, Liu T, Li Y, Wang G, Lan S: Measurement of the refractive index of human teeth by optical coherence tomography. *Journal of Biomedical Optics* 14(3): 34010, 2009
 128. Ohmi M, Ohnishi Y, Yoden K, Haruna M: In vitro simultaneous measurement of refractive index and thickness of biological tissue by the low coherence interferometry. *IEEE transactions on bio-medical engineering* 47(9): 1266–70, 2000
 129. Sand M, Gambichler T, Moussa G, Bechara FG, Sand D, Altmeyer P, Hoffmann K: Evaluation of the epidermal refractive index measured by optical coherence tomography. *Skin research and technology official journal of International Society for Bioengineering and the Skin (ISBS) [and] International Society for Digital Imaging of Skin (ISDIS) [and] International Society for Skin Imaging (ISSI)* 12(2): 114–8, 2006
 130. Zhang XU, Faber DJ, Post AL, van Leeuwen TG, Sterenborg HJCM: Refractive index measurement using single fiber reflectance spectroscopy. *Journal of biophotonics* 12(7): e201900019, 2019
 131. Tearney GJ, Brezinski ME, Southern JF, Bouma BE, Hee MR, Fujimoto JG: Determination of the refractive index of highly scattering human tissue by optical coherence tomography. *Optics letters* 20(21): 2258, 1995
 132. Bhandari A, Stamnes S, Hamre B, Frette O, Stamnes K, Stamnes JJ: Stokes scattering matrix for human skin. *Applied optics* 51(31): 7487–98, 2012
 133. Yarovenko IP, Prokhorov IV: Determination of Refractive Indices of a Layered Medium under Pulsed Irradiation. *Opt. Spectrosc.* 124(4): 567–74, 2018
 134. Churmakov DY, Meglinski IV, Greenhalgh DA: Amending of fluorescence sensor signal localization in human skin by matching of the refractive index. *Journal of Biomedical Optics* 9(2): 339–46, 2004
-

-
135. Gebhart SC, Lin WC, Mahadevan-Jansen A: In vitro determination of normal and neoplastic human brain tissue optical properties using inverse adding-doubling. *Physics in medicine and biology* 51(8): 2011–27, 2006
 136. Pisanello M, Pisano F, Hyun M, Maglie E, Balena A, Vittorio M de, Sabatini BL, Pisanello F: The Three-Dimensional Signal Collection Field for Fiber Photometry in Brain Tissue. *Frontiers in neuroscience* 13: 82, 2019
 137. Sawosz P, Wojtkiewicz S, Kacprzak M, Weigl W, Borowska-Solonynko A, Krajewski P, Bejm K, Milej D, Ciszek B, Maniewski R, Liebert A: Human skull translucency: post mortem studies. *Biomedical optics express* 7(12): 5010–20, 2016
 138. Dirckx JJJ, Kuypers LC, Decraemer WF: Refractive index of tissue measured with confocal microscopy. *Journal of Biomedical Optics* 10(4): 44014, 2005
 139. Tuchina DK, Bashkatov AN, Genina EA, Tuchin VV: Quantification of glucose and glycerol diffusion in myocardium. *J. Innov. Opt. Health Sci.* 08(03): 1541006, 2015
 140. Lai J-C, Zhang Y-Y, Li Z-H, Jiang H-J, He A-Z: Complex refractive index measurement of biological tissues by attenuated total reflection ellipsometry. *Applied optics* 49(16): 3235–8, 2010
 141. Dehghani H, Brooksby BA, Pogue BW, Paulsen KD: Effects of refractive index on near-infrared tomography of the breast. *Applied optics* 44(10): 1870–8, 2005
 142. Matiatou M, Giannios P, Koutsoumpou S, Toutouzou KG, Zografos GC, Moutzouris K: Data on the refractive index of freshly-excised human tissues in the visible and near-infrared spectral range. *Results in Physics* 22: 103833, 2021
 143. Bolin FP, Preuss LE, Taylor RC, Ference RJ: Refractive index of some mammalian tissues using a fiber optic cladding method. *Applied optics* 28(12): 2297–303, 1989
 144. Young PA, Clendenon SG, Byars JM, Dunn KW: The effects of refractive index heterogeneity within kidney tissue on multiphoton fluorescence excitation microscopy. *Journal of microscopy* 242(2): 148–56, 2011
 145. Johnsen S, Widder EA: The physical basis of transparency in biological tissue: ultrastructure and the minimization of light scattering. *Journal of theoretical biology* 199(2): 181–98, 1999
 146. Meyer RA: Light scattering from biological cells: dependence of backscatter radiation on membrane thickness and refractive index. *Applied optics* 18(5): 585–8, 1979
 147. Suhling K, Siegel J, Phillips D, French PMW, Lévêque-Fort S, Webb SED, Davis DM: Imaging the environment of green fluorescent protein. *Biophysical journal* 83(6): 3589–95, 2002
 148. van Manen H-J, Verkuijlen P, Wittendorp P, Subramaniam V, van den Berg TK, Roos D, Otto C: Refractive index sensing of green fluorescent proteins in living cells using fluorescence lifetime imaging microscopy. *Biophysical journal* 94(8): L67-9, 2008
 149. Choi W, Fang-Yen C, Badizadegan K, Oh S, Lue N, Dasari RR, Feld MS: Tomographic phase microscopy. *Nature methods* 4(9): 717–9, 2007
 150. Zhang Q, Zhong L, Tang P, Yuan Y, Liu S, Tian J, Lu X: Quantitative refractive index distribution of single cell by combining phase-shifting interferometry and AFM imaging. *Scientific reports* 7(1): 2532, 2017
 151. Steelman ZA, Eldridge WJ, Weintraub JB, Wax A: Is the nuclear refractive index lower than cytoplasm? Validation of phase measurements and implications for light scattering technologies. *Journal of biophotonics* 10(12): 1714–22, 2017
 152. Cohen-Maslaton S, Barnea I, Taieb A, Shaked NT: Cell and nucleus refractive-index mapping by interferometric phase microscopy and rapid confocal fluorescence microscopy. *Journal of biophotonics* 13(9): e202000117, 2020
 153. Liu PY, Chin LK, Ser W, Chen HF, Hsieh C-M, Lee C-H, Sung K-B, Ayi TC, Yap PH, Liedberg B, Wang K, Bourouina T, Leprince-Wang Y: Cell refractive index for cell biology and disease diagnosis: past, present and future. *Lab on a chip* 16(4): 634–44, 2016
 154. Su J-W, Hsu W-C, Chou C-Y, Chang C-H, Sung K-B: Digital holographic microtomography for high-resolution refractive index mapping of live cells. *Journal of biophotonics* 6(5): 416–24, 2013
 155. Haseda K, Kanematsu K, Noguchi K, Saito H, Umeda N, Ohta Y: Significant correlation between refractive index and activity of mitochondria: single mitochondrion study. *Biomedical optics express* 6(3): 859–69, 2015
 156. Wilson JD, Cottrell WJ, Foster TH: Index-of-refraction-dependent subcellular light scattering observed with organelle-specific dyes. *Journal of Biomedical Optics* 12(1): 14010, 2007
-

-
157. Matryba P, Kaczmarek L, Gołąb J: Advances in Ex Situ Tissue Optical Clearing. *Laser & Photonics Reviews* 13(8): 1800292, 2019
158. Boutin ME, Hoffman-Kim D: Application and Assessment of Optical Clearing Methods for Imaging of Tissue-Engineered Neural Stem Cell Spheres. *Tissue Engineering Part C: Methods* 21(3): 292–302, 2014
159. Lee E, Choi J, Jo Y, Kim JY, Jang YJ, Lee HM, Kim SY, Lee H-J, Cho K, Jung N, Hur EM, Jeong SJ, Moon C, Choe Y, Im Rhyu J, Kim H, Sun W: ACT-PRESTO: Rapid and consistent tissue clearing and labeling method for 3-dimensional (3D) imaging. *Scientific reports* 6: 18631, 2016
160. Toga AW, Ambach KL, Schluender S: High-resolution anatomy from in situ human brain. *NeuroImage* 1(4): 334–44, 1994
161. Tsai PS, Blinder P, Migliori BJ, Neev J, Jin Y, Squier JA, Kleinfeld D: Plasma-mediated ablation: an optical tool for submicrometer surgery on neuronal and vascular systems. *Current opinion in biotechnology* 20(1): 90–9, 2009
162. Zhao J, Lai HM, Qi Y, He D, Sun H: Current Status of Tissue Clearing and the Path Forward in Neuroscience. *ACS chemical neuroscience* 12(1): 5–29, 2021
163. Tian T, Yang Z, Li X: Tissue clearing technique: Recent progress and biomedical applications. *Journal of anatomy* 238(2): 489–507, 2021
164. Spalteholz W: *Über das Durchsichtigmachen von menschlichen und tierischen Präparaten u. s. theoret. Bedingungen*, 2nd ed., Leipzig, Hirzel, 1914
165. Spalteholz W: *Handatlas der Anatomie des Menschen*, Leipzig, Hirzel, 1913
166. Dent JA, Polson AG, Klymkowsky MW: A whole-mount immunocytochemical analysis of the expression of the intermediate filament protein vimentin in *Xenopus*. *Development (Cambridge, England)* 105(1): 61–74, 1989
167. Dodt H-U, Leischner U, Schierloh A, Jährling N, Mauch CP, Deininger K, Deussing JM, Eder M, Zieglgänsberger W, Becker K: Ultramicroscopy: three-dimensional visualization of neuronal networks in the whole mouse brain. *Nature methods* 4(4): 331–6, 2007
168. Zhan Y, Wu H, Liu L, Lin J, Zhang S: Organic solvent-based tissue clearing techniques and their applications. *Journal of biophotonics* 14(6): e202000413, 2021
169. Becker K, Jährling N, Saghafi S, Weiler R, Dodt H-U: Chemical clearing and dehydration of GFP expressing mouse brains. *PloS one* 7(3): e33916, 2012
170. Ertürk A, Becker K, Jährling N, Mauch CP, Hojer CD, Egen JG, Hellal F, Bradke F, Sheng M, Dodt H-U: Three-dimensional imaging of solvent-cleared organs using 3DISCO. *Nature protocols* 7(11): 1983–95, 2012
171. Schwarz MK, Scherbarth A, Sprengel R, Engelhardt J, Theer P, Giese G: Fluorescent-protein stabilization and high-resolution imaging of cleared, intact mouse brains. *PloS one* 10(5): e0124650, 2015
172. Ertürk A, Bradke F: High-resolution imaging of entire organs by 3-dimensional imaging of solvent cleared organs (3DISCO). *Experimental neurology* 242: 57–64, 2013
173. Molbay M, Kolabas ZI, Todorov MI, Ohn T-L, Ertürk A: A guidebook for DISCO tissue clearing. *Molecular Systems Biology* 17(3): e9807, 2021
174. Renier N, Wu Z, Simon DJ, Yang J, Ariel P, Tessier-Lavigne M: iDISCO: a simple, rapid method to immunolabel large tissue samples for volume imaging. *Cell* 159(4): 896–910, 2014
175. Renier N, Adams EL, Kirst C, Wu Z, Azevedo R, Kohl J, Autry AE, Kadiri L, Umadevi Venkataraju K, Zhou Y, Wang VX, Tang CY, Olsen O, Dulac C, Osten P, Tessier-Lavigne M: Mapping of Brain Activity by Automated Volume Analysis of Immediate Early Genes. *Cell* 165(7): 1789–802, 2016
176. Pan C, Cai R, Quacquarelli FP, Ghasemigharagoz A, Lourbopoulos A, Matryba P, Plesnila N, Dichgans M, Hellal F, Ertürk A: Shrinkage-mediated imaging of entire organs and organisms using uDISCO. *Nature methods* 13(10): 859–67, 2016
177. Qi Y, Yu T, Xu J, Wan P, Ma Y, Zhu J, Li Y, Gong H, Luo Q, Zhu D: FDISCO: Advanced solvent-based clearing method for imaging whole organs. *Science advances* 5(1): eaau8355, 2019
178. Hahn C, Becker K, Saghafi S, Pende M, Avdibašić A, Foroughipour M, Heinz DE, Wotjak CT, Dodt H-U: High-resolution imaging of fluorescent whole mouse brains using stabilised organic media (sDISCO). *Journal of biophotonics* 12(8): e201800368, 2019
-

-
179. Gusachenko I, Nylk J, Tello JA, Dholakia K: Multimode fibre based imaging for optically cleared samples. *Biomedical optics express* 8(11): 5179–90, 2017
180. Simon JE, Villani T, Koroch A: *Clearing agent and mounting medium for microscopy* US9464971B2(US9464971B2), 2016. Available at <https://patents.google.com/patent/us9464971/en>
181. Staudt T, Lang MC, Medda R, Engelhardt J, Hell SW: 2,2'-thiodiethanol: a new water soluble mounting medium for high resolution optical microscopy. *Microscopy research and technique* 70(1): 1–9, 2007
182. Aoyagi Y, Kawakami R, Osanai H, Hibi T, Nemoto T: A Rapid Optical Clearing Protocol Using 2,2'-Thiodiethanol for Microscopic Observation of Fixed Mouse Brain. *PLoS one* 10(1), 2015
183. Costantini I, Ghobril J-P, Di Giovanna AP, Allegra Mascaro AL, Silvestri L, Müllenbroich MC, Onofri L, Conti V, Vanzi F, Sacconi L, Guerrini R, Markram H, Iannello G, Pavone FS: A versatile clearing agent for multi-modal brain imaging. *Scientific reports* 5: 9808, 2015
184. Tsai PS, Kaufhold JP, Blinder P, Friedman B, Drew PJ, Karten HJ, Lyden PD, Kleinfeld D: Correlations of Neuronal and Microvascular Densities in Murine Cortex Revealed by Direct Counting and Colocalization of Nuclei and Vessels. *The Journal of Neuroscience* 29(46): 14553–70, 2009
185. Ke M-T, Fujimoto S, Imai T: SeeDB: a simple and morphology-preserving optical clearing agent for neuronal circuit reconstruction. *Nature neuroscience* 16(8): 1154–61, 2013
186. Ke M-T, Imai T: Optical Clearing and Index Matching of Tissue Samples for High-resolution Fluorescence Imaging Using SeeDB2. *Bio-protocol* 8(20), 2018
187. Hou B, Zhang D, Zhao S, Wei M, Yang Z, Wang S, Wang J, Zhang X, Liu B, Fan L, Li Y, Qiu Z, Zhang C, Jiang T: Scalable and DiI-compatible optical clearance of the mammalian brain. *Frontiers in Neuroanatomy* 9, 2015
188. Chiang A-S: *Aqueous tissue clearing solution*(US6472216B1), 2002. Available at <https://patents.google.com/patent/us6472216b1/en>
189. Williams MPI, Rigon M, Straka T, Hörner SJ, Thiel M, Gretz N, Hafner M, Reischl M, Rudolf R: A Novel Optical Tissue Clearing Protocol for Mouse Skeletal Muscle to Visualize Endplates in Their Tissue Context. *Frontiers in cellular neuroscience* 13: 49, 2019
190. Straka T, Schröder C, Roos A, Kollipara L, Sickmann A, Williams MPI, Hafner M, Khan MM, Rudolf R: Regulatory Function of Sympathetic Innervation on the Endo/Lysosomal Trafficking of Acetylcholine Receptor. *Frontiers in physiology* 12: 626707, 2021
191. Zhao Y-J, Yu T-T, Zhang C, Li Z, Luo Q-M, Xu T-H, Zhu D: Skull optical clearing window for in vivo imaging of the mouse cortex at synaptic resolution. *Light, science & applications* 7: 17153, 2018
192. Zhu X, Huang L, Zheng Y, Song Y, Xu Q, Wang J, Si K, Duan S, Gong W: Ultrafast optical clearing method for three-dimensional imaging with cellular resolution. *Proceedings of the National Academy of Sciences of the United States of America* 116(23): 11480–9, 2019
193. Hama H, Hioki H, Namiki K, Hoshida T, Kurokawa H, Ishidate F, Kaneko T, Akagi T, Saito T, Saido T, Miyawaki A: ScaleS: an optical clearing palette for biological imaging. *Nature neuroscience* 18(10): 1518–29, 2015
194. Hama H, Kurokawa H, Kawano H, Ando R, Shimogori T, Noda H, Fukami K, Sakaue-Sawano A, Miyawaki A: Scale: a chemical approach for fluorescence imaging and reconstruction of transparent mouse brain. *Nature neuroscience* 14(11): 1481–8, 2011
195. Chung K, Wallace J, Kim S-Y, Kalyanasundaram S, Andalman AS, Davidson TJ, Mirzabekov JJ, Zalocusky KA, Mattis J, Denisin AK, Pak S, Bernstein H, Ramakrishnan C, Grosenick L, Gradinaru V, Deisseroth K: Structural and molecular interrogation of intact biological systems. *Nature* 497(7449): 332–7, 2013
196. Yu T, Zhu J, Li D, Zhu D: Physical and chemical mechanisms of tissue optical clearing. *iScience* 24(3): 102178, 2021
197. Rylander CG, Stumpp OF, Milner TE, Kemp NJ, Mendenhall JM, Diller KR, Welch AJ: Dehydration mechanism of optical clearing in tissue. *Journal of Biomedical Optics* 11(4): 41117, 2006
198. Yu T, Li D, Zhu D: Tissue Optical Clearing for Biomedical Imaging: From In Vitro to In Vivo. *Advances in experimental medicine and biology* 3233: 217–55, 2021
-

-
199. Hua L, Zhou R, Thirumalai D, Berne BJ: Urea denaturation by stronger dispersion interactions with proteins than water implies a 2-stage unfolding. *Proceedings of the National Academy of Sciences of the United States of America* 105(44): 16928–33, 2008
 200. Tainaka K, Murakami TC, Susaki EA, Shimizu C, Saito R, Takahashi K, Hayashi-Takagi A, Sekiya H, Arima Y, Nojima S, Ikemura M, Ushiku T, Shimizu Y, Murakami M, Tanaka KF, Iino M, Kasai H, Sasaoka T, Kobayashi K, Miyazono K, Morii E, Isa T, Fukayama M, Kakita A, Ueda HR: Chemical Landscape for Tissue Clearing Based on Hydrophilic Reagents. *Cell reports* 24(8): 2196-2210.e9, 2018
 201. Susaki EA, Tainaka K, Perrin D, Kishino F, Tawara T, Watanabe TM, Yokoyama C, Onoe H, Eguchi M, Yamaguchi S, Abe T, Kiyonari H, Shimizu Y, Miyawaki A, Yokota H, Ueda HR: Whole-brain imaging with single-cell resolution using chemical cocktails and computational analysis. *Cell* 157(3): 726–39, 2014
 202. Tainaka K, Kubota SI, Suyama TQ, Susaki EA, Perrin D, Ukai-Tadenuma M, Ukai H, Ueda HR: Whole-body imaging with single-cell resolution by tissue decolorization. *Cell* 159(4): 911–24, 2014
 203. Kuwajima T, Sitko AA, Bhansali P, Jurgens C, Guido W, Mason C: ClearT: a detergent- and solvent-free clearing method for neuronal and non-neuronal tissue. *Development (Cambridge, England)* 140(6): 1364–8, 2013
 204. Dapper CH, Valivullah HM, Keenan TW: Use of polar aprotic solvents to release membranes from milk lipid globules. *Journal of dairy science* 70(4): 760–5, 1987
 205. Chung K, Deisseroth K: CLARITY for mapping the nervous system. *Nature methods* 10(6): 508–13, 2013
 206. Kim S-Y, Cho JH, Murray E, Bakh N, Choi H, Ohn K, Ruelas L, Hubbert A, McCue M, Vassallo SL, Keller PJ, Chung K: Stochastic electrotransport selectively enhances the transport of highly electromobile molecules. *Proceedings of the National Academy of Sciences of the United States of America* 112(46): E6274-83, 2015
 207. Tomer R, Ye L, Hsueh B, Deisseroth K: Advanced CLARITY for rapid and high-resolution imaging of intact tissues. *Nature protocols* 9(7): 1682–97, 2014
 208. Yang B, Treweek JB, Kulkarni RP, Deverman BE, Chen C-K, Lubeck E, Shah S, Cai L, Gradinaru V: Single-Cell Phenotyping within Transparent Intact Tissue Through Whole-Body Clearing. *Cell* 158(4): 945–58, 2014
 209. Park Y-G, Sohn CH, Chen R, McCue M, Yun DH, Drummond GT, Ku T, Evans NB, Oak HC, Trieu W, Choi H, Jin X, Lilascharoen V, Wang J, Truttmann MC, Qi HW, Ploegh HL, Golub TR, Chen S-C, Frosch MP, Kulik HJ, Lim BK, Chung K: Protection of tissue physicochemical properties using polyfunctional crosslinkers. *Nature biotechnology*, 2018
 210. Poguzhelskaya E, Artamonov D, Bolshakova A, Vlasova O, Bezprozvanny I: Simplified method to perform CLARITY imaging. *Molecular Neurodegeneration* 9: 19, 2014
 211. Xu N, Tamadon A, Liu Y, Ma T, Leak RK, Chen J, Gao Y, Feng Y: Fast free-of-acrylamide clearing tissue (FACT)-an optimized new protocol for rapid, high-resolution imaging of three-dimensional brain tissue. *Scientific reports* 7(1): 9895, 2017
 212. Murray E, Cho JH, Goodwin D, Ku T, Swaney J, Kim S-Y, Choi H, Park Y-G, Park J-Y, Hubbert A, McCue M, Vassallo S, Bakh N, Frosch MP, van Wedeer J, Seung HS, Chung K: Simple, Scalable Proteomic Imaging for High-Dimensional Profiling of Intact Systems. *Cell* 163(6): 1500–14, 2015
 213. Azaripour A, Lagerweij T, Scharfbillig C, Jadczyk AE, Willershausen B, van Noorden CJF: A survey of clearing techniques for 3D imaging of tissues with special reference to connective tissue. *Progress in histochemistry and cytochemistry* 51(2): 9–23, 2016
 214. Wenzel C, Riefke B, Gründemann S, Krebs A, Christian S, Prinz F, Osterland M, Golfier S, Räsé S, Ansari N, Esner M, Bickle M, Pampaloni F, Mattheyer C, Stelzer EH, Parczyk K, Prechtel S, Steigemann P: 3D high-content screening for the identification of compounds that target cells in dormant tumor spheroid regions. *Experimental cell research* 323(1): 131–43, 2014
 215. Smyrek I, Stelzer EHK: Quantitative three-dimensional evaluation of immunofluorescence staining for large whole mount spheroids with light sheet microscopy. *Biomedical optics express* 8(2): 484–99, 2017
 216. Schmitz A, Fischer SC, Mattheyer C, Pampaloni F, Stelzer EHK: Multiscale image analysis reveals structural heterogeneity of the cell microenvironment in homotypic spheroids. *Scientific reports* 7, 2017
 217. Desmaison A, Guillaume L, Triclin S, Weiss P, Ducommun B, Lobjois V: Impact of physical confinement on nuclei geometry and cell division dynamics in 3D spheroids. *Scientific reports* 8, 2018
-

-
218. Renner H, Grabos M, Becker KJ, Kagermeier TE, Wu J, Otto M, Peischard S, Zeuschner D, TsyTsyura Y, Disse P, Klingauf J, Leidel SA, Seeböhm G, Schöler HR, Bruder JM: A fully automated high-throughput workflow for 3D-based chemical screening in human midbrain organoids. *eLife* 9, 2020
219. Renner H, Otto M, Grabos M, Schöler HR, Bruder JM: Fluorescence-based Single-cell Analysis of Whole-mount-stained and Cleared Microtissues and Organoids for High Throughput Screening. *Bio-protocol* 11(12): e4050, 2021
220. Goranci-Buzhala G, Mariappan A, Gabriel E, Ramani A, Ricci-Vitiani L, Buccarelli M, D'Alessandris QG, Pallini R, Gopalakrishnan J: Rapid and Efficient Invasion Assay of Glioblastoma in Human Brain Organoids. *Cell reports* 31(10): 107738, 2020
221. Goranci-Buzhala G, Mariappan A, Ricci-Vitiani L, Josipovic N, Pacioni S, Gottardo M, Ptok J, Schaal H, Callaini G, Rajalingam K, Dynlacht B, Hadian K, Papantonis A, Pallini R, Gopalakrishnan J: Cilium induction triggers differentiation of glioma stem cells. *Cell reports* 36(10): 109656, 2021
222. Masselink W, Reumann D, Murawala P, Pasierbek P, Taniguchi Y, Bonnay F, Meixner K, Knoblich JA, Tanaka EM: Broad applicability of a streamlined ethyl cinnamate-based clearing procedure. *Development (Cambridge, England)* 146(3), 2019
223. Wörsdörfer P, Dalda N, Kern A, Krüger S, Wagner N, Kwok CK, Henke E, Ergün S: Generation of complex human organoid models including vascular networks by incorporation of mesodermal progenitor cells. *Scientific reports* 9, 2019
224. Paiè P, Bragheri F, Bassi A, Osellame R: Selective plane illumination microscopy on a chip. *Lab on a chip* 16(9): 1556–60, 2016
225. Lallemand L, Lebreton C, Garfa-Traoré M: Comparison of different clearing and acquisition methods for 3D imaging of murine intestinal organoids. *Journal of Biological Methods* 7(4), 2020
226. Grist SM, Nasser SS, Poon T, Roskelley C, Cheung KC: On-chip clearing of arrays of 3-D cell cultures and micro-tissues. *Biomicrofluidics* 10(4), 2016
227. Bekkouche BMB, Fritz HKM, Rigosi E, O'Carroll DC: Comparison of Transparency and Shrinkage During Clearing of Insect Brains Using Media With Tunable Refractive Index. *Frontiers in Neuroanatomy* 14, 2020
228. Steinberg E, Orehov N, Tischenko K, Schwob O, Zamir G, Hubert A, Manevitch Z, Benny O: Rapid Clearing for High Resolution 3D Imaging of Ex Vivo Pancreatic Cancer Spheroids. *International Journal of Molecular Sciences* 21(20), 2020
229. Govindan S, Batti L, Osterop SF, Stoppini L, Roux A: Mass Generation, Neuron Labeling, and 3D Imaging of Minibrains. *Frontiers in bioengineering and biotechnology* 8: 582650, 2020
230. Boutin ME, Kramer LL, Livi LL, Brown T, Moore C, Hoffman-Kim D: A three-dimensional neural spheroid model for capillary-like network formation. *Journal of neuroscience methods* 299: 55–63, 2018
231. Dingle Y-TL, Boutin ME, Chirila AM, Livi LL, Labriola NR, Jakubek LM, Morgan JR, Darling EM, Kauer JA, Hoffman-Kim D: Three-Dimensional Neural Spheroid Culture: An In Vitro Model for Cortical Studies. *Tissue Engineering Part C: Methods* 21(12): 1274–83, 2015
232. Kabadi PK, Vantangoli MM, Rodd AL, Leary E, Madnick SJ, Morgan JR, Kane A, Boekelheide K: Into the depths: Techniques for in vitro three-dimensional microtissue visualization. *BioTechniques* 59(5): 279–86, 2015
233. Costa EC, Moreira AF, Melo-Diogo D de, Correia IJ: Polyethylene glycol molecular weight influences the ClearT2 optical clearing method for spheroids imaging by confocal laser scanning microscopy. *Journal of Biomedical Optics* 23(5): 1–11, 2018
234. Costa EC, Moreira AF, Melo-Diogo D de, Correia IJ: ClearT immersion optical clearing method for intact 3D spheroids imaging through confocal laser scanning microscopy. *Optics & Laser Technology* 106: 94–9, 2018
235. Castellanos-Montiel MJ, Chaineau M, Franco-Flores AK, Haggi G, Carrillo-Valenzuela D, Reintsch WE, Chen CX-Q, Durcan TM: An Optimized Workflow to Generate and Characterize iPSC-Derived Motor Neuron (MN) Spheroids. *Cells* 12(4), 2023
236. Chen YY, Silva PN, Syed AM, Sindhvani S, Rocheleau JV, Chan WCW: Clarifying intact 3D tissues on a microfluidic chip for high-throughput structural analysis. *Proceedings of the National Academy of Sciences of the United States of America* 113(52): 14915–20, 2016
-

-
237. Silva Santisteban T, Rabajania O, Kalinina I, Robinson S, Meier M: Rapid spheroid clearing on a microfluidic chip. *Lab on a chip* 18(1): 153–61, 2017
238. Cora V, Haderspeck J, Antkowiak L, Mattheus U, Neckel PH, Mack AF, Bolz S, Ueffing M, Pashkovskaia N, Achberger K, Liebau S: A Cleared View on Retinal Organoids. *Cells* 8(5), 2019
239. Renner M, Lancaster MA, Bian S, Choi H, Ku T, Peer A, Chung K, Knoblich JA: Self-organized developmental patterning and differentiation in cerebral organoids. *The EMBO journal* 36(10): 1316–29, 2017
240. Albanese A, Swaney JM, Yun DH, Evans NB, Antonucci JM, Velasco S, Sohn CH, Arlotta P, Gehrke L, Chung K: Multiscale 3D phenotyping of human cerebral organoids. *Scientific reports* 10, 2020
241. Susaki EA, Takasato M: Perspective: Extending the Utility of Three-Dimensional Organoids by Tissue Clearing Technologies. *Frontiers in cell and developmental biology* 9: 679226, 2021
242. Chen L, Li G, Li Y, Li Y, Zhu H, Tang L, French P, McGinty J, Ruan S: UbasM: An effective balanced optical clearing method for intact biomedical imaging. *Scientific reports* 7(1): 12218, 2017
243. Hofmann J, Gadjalova I, Mishra R, Ruland J, Keppler SJ: Efficient Tissue Clearing and Multi-Organ Volumetric Imaging Enable Quantitative Visualization of Sparse Immune Cell Populations During Inflammation. *Frontiers in immunology* 11: 599495, 2020
244. Xu J, Ma Y, Yu T, Zhu D: Quantitative assessment of optical clearing methods in various intact mouse organs. *Journal of biophotonics* 12(2): e201800134, 2019
245. Diosdi A, Hirling D, Kovacs M, Toth T, Harmati M, Koos K, Buzas K, Piccinini F, Horvath P: Cell lines and clearing approaches: a single-cell level 3D light-sheet fluorescence microscopy dataset of multicellular spheroids. *Data in Brief* 36: 107090, 2021
246. Diosdi A, Hirling D, Kovacs M, Toth T, Harmati M, Koos K, Buzas K, Piccinini F, Horvath P: A quantitative metric for the comparative evaluation of optical clearing protocols for 3D multicellular spheroids. *Computational and structural biotechnology journal* 19: 1233–43, 2021
247. Nürnberg E, Vitacolonna M, Klicks J, Molitor E von, Cesetti T, Keller F, Bruch R, Ertongur-Fauth T, Riedel K, Scholz P, Lau T, Schneider R, Meier J, Hafner M, Rudolf R: Routine Optical Clearing of 3D-Cell Cultures: Simplicity Forward. *Frontiers in molecular biosciences* 7: 20, 2020
248. Nürnberg E, Horschitz S, Schloss P, Meyer-Lindenberg A: Basal glucocorticoid receptor activation induces proliferation and inhibits neuronal differentiation of human induced pluripotent stem cell-derived neuronal precursor cells. *The Journal of steroid biochemistry and molecular biology* 182: 119–26, 2018
249. Hochheimer A, Krohn M, Rudert K, Riedel K, Becker S, Thirion C, Zinke H: Endogenous gustatory responses and gene expression profile of stably proliferating human taste cells isolated from fungiform papillae. *Chemical senses* 39(4): 359–77, 2014
250. Molitor E von, Nürnberg E, Ertongur-Fauth T, Scholz P, Riedel K, Hafner M, Rudolf R, Cesetti T: Analysis of calcium signaling in live human Tongue cell 3D-Cultures upon tastant perfusion. *Cell calcium* 87: 102164, 2020
251. Keller F, Bruch R, Schneider R, Meier-Hubberten J, Hafner M, Rudolf R: A Scaffold-Free 3-D Co-Culture Mimics the Major Features of the Reverse Warburg Effect In Vitro. *Cells* 9(8), 2020
252. Horschitz S, Matthäus F, Groß A, Rosner J, Galach M, Greffrath W, Treede R-D, Utikal J, Schloss P, Meyer-Lindenberg A: Impact of preconditioning with retinoic acid during early development on morphological and functional characteristics of human induced pluripotent stem cell-derived neurons. *Stem cell research* 15(1): 30–41, 2015
253. Rose A: The Sensitivity Performance of the Human Eye on an Absolute Scale*. *J. Opt. Soc. Am.* 38(2): 196–208, 1948
254. Eichmüller OL, Knoblich JA: Human cerebral organoids - a new tool for clinical neurology research. *Nature reviews. Neurology* 18(11): 661–80, 2022
255. Kim J, Koo B-K, Knoblich JA: Human organoids: model systems for human biology and medicine. *Nature reviews. Molecular cell biology* 21(10): 571–84, 2020
256. Mayhew CN, Singhanian R: A review of protocols for brain organoids and applications for disease modeling. *STAR protocols* 4(1), 2022
257. Ardhanareeswaran K, Mariani J, Coppola G, Abyzov A, Vaccarino FM: Human induced pluripotent stem cells for modelling neurodevelopmental disorders. *Nature reviews. Neurology* 13(5): 265–78, 2017
-

-
258. Papariello A, Newell-Litwa K: Human-Derived Brain Models: Windows into Neuropsychiatric Disorders and Drug Therapies. *Assay and drug development technologies* 18(2): 79–88, 2020
259. Wilson ES, Newell-Litwa K: Stem cell models of human synapse development and degeneration. *Molecular biology of the cell* 29(24): 2913–21, 2018
260. Cetin S, Knez D, Gobec S, Kos J, Pišlar A: Cell models for Alzheimer's and Parkinson's disease: At the interface of biology and drug discovery. *Biomedicine & pharmacotherapy = Biomedecine & pharmacotherapie* 149: 112924, 2022
261. Scott CW, Peters MF, Dragan YP: Human induced pluripotent stem cells and their use in drug discovery for toxicity testing. *Toxicology letters* 219(1): 49–58, 2013
262. Martí Y, Nürnberg E, Horschitz S, Hafner M, Schloss P, Meyer-Lindenberg A, Lau T: Refinement of a neuronal differentiation protocol predominantly yields human iPSC cell-derived dopaminergic neurons for the investigation of neurodegenerative pathomechanisms in vitro. *JCB* 3(1): 61–80, 2017
263. Falk A, Koch P, Kesavan J, Takashima Y, Ladewig J, Alexander M, Wiskow O, Tailor J, Trotter M, Pollard S, Smith A, Brüstle O: Capture of neuroepithelial-like stem cells from pluripotent stem cells provides a versatile system for in vitro production of human neurons. *PLoS one* 7(1): e29597, 2012
264. Nicholas CR, Chen J, Tang Y, Southwell DG, Chalmers N, Vogt D, Arnold CM, Chen Y-JJ, Stanley EG, Elefanty AG, Sasai Y, Alvarez-Buylla A, Rubenstein JLR, Kriegstein AR: Functional maturation of hPSC-derived forebrain interneurons requires an extended timeline and mimics human neural development. *Cell stem cell* 12(5): 573–86, 2013
265. Kobolak J, Teglas A, Bellak T, Janstova Z, Molnar K, Zana M, Bock I, Laszlo L, Dinnyes A: Human Induced Pluripotent Stem Cell-Derived 3D-Neurospheres are Suitable for Neurotoxicity Screening. *Cells* 9(5), 2020
266. Pamies D, Barrera P, Block K, Makri G, Kumar A, Wiersma D, Smirnova L, Zhang C, Bressler J, Christian KM, Harris G, Ming G, Berlinicke CJ, Kyro K, Song H, Pardo CA, Hartung T, Hogberg HT: A Human Brain Microphysiological System Derived from Induced Pluripotent Stem Cells to Study Neurological Diseases and Toxicity. *ALTEX* 34(3): 362–76, 2016
267. Hausrat TJ, Radwitz J, Lombino FL, Breiden P, Kneussel M: Alpha- and beta-tubulin isotypes are differentially expressed during brain development. *Developmental neurobiology* 81(3): 333–50, 2021
268. Park H, Kim J, Ryou C: A three-dimensional spheroid co-culture system of neurons and astrocytes derived from Alzheimer's disease patients for drug efficacy testing. *Cell proliferation* 56(6): e13399, 2023
269. Mercurio S, Serra L, Nicolis SK: More than just Stem Cells: Functional Roles of the Transcription Factor Sox2 in Differentiated Glia and Neurons. *International Journal of Molecular Sciences* 20(18), 2019
270. O'Connor SA, Feldman HM, Arora S, Hoellerbauer P, Toledo CM, Corrin P, Carter L, Kufeld M, Bolouri H, Basom R, Delrow J, McFaline-Figueroa JL, Trapnell C, Pollard SM, Patel A, Paddison PJ, Plaisier CL: Neural G0: a quiescent-like state found in neuroepithelial-derived cells and glioma. *Molecular Systems Biology* 17(6): e9522, 2021
271. Surzenko N, Crowl T, Bachleda A, Langer L, Pevny L: SOX2 maintains the quiescent progenitor cell state of postnatal retinal Müller glia. *Development (Cambridge, England)* 140(7): 1445–56, 2013
272. Stern CD: Initial patterning of the central nervous system: how many organizers? *Nature reviews. Neuroscience* 2(2): 92–8, 2001
273. Lau T, Proissl V, Ziegler J, Schloss P: Visualization of neurotransmitter uptake and release in serotonergic neurons. *Journal of neuroscience methods* 241: 10–7, 2015
274. Matthaeus F, Schloss P, Lau T: Differential Uptake Mechanisms of Fluorescent Substrates into Stem-Cell-Derived Serotonergic Neurons. *ACS chemical neuroscience* 6(12): 1906–12, 2015
275. Chen F, Tillberg PW, Boyden ES: Optical imaging. Expansion microscopy. *Science (New York, N.Y.)* 347(6221): 543–8, 2015
276. Jonkman J, Brown CM, Cole RW: Quantitative confocal microscopy: beyond a pretty picture. *Methods in cell biology* 123: 113–34, 2014
277. Brown RC, Lemmon BE: Methods in plant immunolight microscopy. *Methods in cell biology* 49: 85–107, 1995
-

-
278. Ghosh KK, Goodchild AK, Sefton AE, Martin PR: Morphology of retinal ganglion cells in a New World monkey, the marmoset *Callithrix jacchus*. *J. Comp. Neurol.* 366(1): 76–92, 1996
279. Silva DN, Costa EC, Rodrigues CF, Melo-Diogo D de, Correia IJ, Moreira AF: Influence of ClearT and ClearT2 Agitation Conditions in the Fluorescence Imaging of 3D Spheroids. *International Journal of Molecular Sciences* 22(1), 2020
280. Acharya M, Arsi K, Donoghue AM, Liyanage R, Rath NC: Production and characterization of avian cryptovirus enteroids and the effect of chemicals. *BMC veterinary research* 16(1): 179, 2020
281. Sunil V, Mozhi A, Zhan W, Teoh JH, Wang C-H: Convection enhanced delivery of light responsive antigen capturing oxygen generators for chemo-phototherapy triggered adaptive immunity. *Biomaterials* 275: 120974, 2021
282. Hsiao F-T, Chien H-J, Chou Y-H, Peng S-J, Chung M-H, Huang T-H, Lo L-W, Shen C-N, Chang H-P, Lee C-Y, Chen C-C, Jeng Y-M, Tien Y-W, Tang S-C: Transparent tissue in solid state for solvent-free and antifade 3D imaging. *Nature communications* 14(1): 3395, 2023
283. Boutin ME, Voss TC, Titus SA, Cruz-Gutierrez K, Michael S, Ferrer M: A high-throughput imaging and nuclear segmentation analysis protocol for cleared 3D culture models. *Scientific reports* 8, 2018
284. Bruch R, Keller F, Böhlend M, Vitacolonna M, Klinger L, Rudolf R, Reischl M: Synthesis of large scale 3D microscopic images of 3D cell cultures for training and benchmarking. *PLoS one* 18(3), 2023
285. Toyoshima Y, Tokunaga T, Hirose O, Kanamori M, Teramoto T, Jang MS, Kuge S, Ishihara T, Yoshida R, Iino Y: Accurate Automatic Detection of Densely Distributed Cell Nuclei in 3D Space. *PLoS computational biology* 12(6): e1004970, 2016
286. Stringer C, Wang T, Michaelos M, Pachitariu M: Cellpose: a generalist algorithm for cellular segmentation. *Nature methods* 18(1): 100–6, 2021
287. Pachitariu M, Stringer C: Cellpose 2.0: how to train your own model. *Nature methods* 19(12): 1634–41, 2022
288. Rizwan I Haque I, Neubert J: Deep learning approaches to biomedical image segmentation. *Informatics in Medicine Unlocked* 18: 100297, 2020
289. Dehmelt L, Halpain S: The MAP2/Tau family of microtubule-associated proteins. *Genome Biology* 6(1): 204, 2004
290. Kanai Y, Hirokawa N: Sorting mechanisms of tau and MAP2 in neurons: suppressed axonal transit of MAP2 and locally regulated microtubule binding. *Neuron* 14(2): 421–32, 1995
291. Yu T, Qi Y, Wang J, Feng W, Xu J, Zhu J, Yao Y, Gong H, Luo Q, Zhu D: Rapid and prodium iodide-compatible optical clearing method for brain tissue based on sugar/sugar-alcohol. *Journal of Biomedical Optics* 21(8): 81203, 2016
292. Li W, Germain RN, Gerner MY: Multiplex, quantitative cellular analysis in large tissue volumes with clearing-enhanced 3D microscopy (Ce3D). *Proceedings of the National Academy of Sciences of the United States of America* 114(35): E7321-E7330, 2017

8 Appendix

8.1 List of cell culture materials

Table 8-1: List of cell culture materials

Reagent	Supplier	Catalogue No.	Lot No.
10x Trypsin-EDTA solution	Sigma-Aldrich	59418C	SLCC3240
5 % AseI enzyme	New England Biolabs	R0526S	131701
96-well Clear Round Bottom Ultra-Low Attachment (ULA) Microplate	Corning	7007	
Alkaline phosphatase	Invitrogen	100012546	1752270
AseI buffer 3.1	New England Biolabs	B7203S	421612
B27 Supplement (50x), serum free	Invitrogen	17504044	1987565
Basal Iscove Medium	Biochrome	F0465	1173E
CellTracker Green CMFDA Dye	ThermoFisher Scientific	C2925	1781143
CellTracker Red CMPTX Dye	ThermoFisher Scientific	C34552	1890538
Collagen 1 from rat tail tendon	Sigma-Aldrich	11179179001	38429220
DMEM	Capricorn	DMEM-HPA	CP18-2096
DMEM/Ham's F-12, w/ GlutaMAX supplement	Invitrogen	10565018	2124955
Dynarrays MCA-CXXX-300-PC	300MICRONS		
Fetal bovine serum (FBS)	Capricorn	FBS-12A	CP16-1422
Gentamicine	Biochrome	A2712	950302
GlutaMAX	Invitrogen	35050061	2063464
IMDM	Sigma-Aldrich	I3390	RNBG9989
Insulin	Sigma-Aldrich	I-6634	74H00845
L-Glutamine (200 mM)	Capricorn	GLN-B	CP17-1801
McCoy's 5A	Capricorn	MCC-A	CP19-2689
MCDB	Biochrome	F8105	0674G
Minimum Essential Medium Nonessential Amino Acids (MEM-NEAA)	Invitrogen	10370070	2026977
N-2 Supplement (100x)	Invitrogen	17502048	1911689
Pen/Strep (10.000 U penicillin, 10 mg/mL streptomycin)	Sigma-Aldrich	P4333	049M4857V
Poly-L-ornithine (PLO)	Sigma Aldrich	P4957	
Recombinant human FGF-2 Type 147	Cell Guidance Systems	GFH28-100	313
TrypLE Express Enzyme (1X), no phenol red	Invitrogen	12604021	2085298

8.2 Consumables and chemicals used for immunofluorescence and optical clearing experiments

Table 8-2: List of materials for immunofluorescence labeling and optical clearing

Reagent	Supplier	Catalogue No.	Lot No.
μ -Slide 18 Well - Flat	Ibidi	81826	
Albumin Fraktion V (BSA)	Carl Roth	8076.3	69279339
CytoVista 3D Cell Culture Clearing Reagent	Invitrogen	V11315	9QZ53
D(+)-Saccharose (sucrose)	Carl Roth	4621.1	
Dimethylsulfoxid (DMSO)	Carl Roth	A994.1	199282083
D-sorbitol	Sigma-Aldrich	1077581000	M529358845
Formamide	Sigma-Aldrich	47671	372879/1 44997
Gelatin from cold water fish skin	Sigma Aldrich	G7041	
Glass coverslips 24 x 60 mm	Thermo Scientific / Menzel	MEZ102460	
Glycerol	Carl Roth	3783.2	237259780
Glycine	Carl Roth	3908.2	177257836
Heparin sodium salt from porcine intestinal mucosa	Sigma-Aldrich	H3149-250KU	SLBN6012V
Mowiol 4-88	Sigma-Aldrich	713.2	269278961
OCT, FSC22 Clear,	Leica Biosystems	3801480	
Paraformaldehyde (PFA)	Carl Roth	335.3	259284291
Polyethylenglykol 8000 (PEG)	Sigma-Aldrich	P5413	BCCC6496
Sodium citrate tribasic dihydrate	Sigma-Aldrich	C8532	
SuperFrost® plus objective slides	Thermo Scientific / Menzel	J1800AMNZ	
Triton X-100	Carl Roth	T9284	19K01512
Tween-20	Sigma-Aldrich	P9416-50ML	125K01031
Urea	Sigma-Aldrich	1084871000	K40676887002

8.3 Percentage loss of depth-dependent signal intensity in cleared B7_033#1NPC1 spheroids

Table 8-3: Percentage loss of depth-dependent signal intensity in cleared B7_033#1NPC1 spheroids. Adapted from Nürnberg et al. (2020)²⁴⁷.

		DAPI							
	Depth [μm]	25	50	75	100	125	150	175	200
PBS	% of darkening	21,91	48,33	64,61	73,79	78,89	81,76	83,74	85,02
	s.d. [%]	5,2	6,56	6,56	6,04	5,21	4,78	4,39	3,97
Mowiol	% of darkening	12,95	32,62	49,85	63,59	73,43	81,42	88,34	92,15
	s.d. [%]	4,53	5,44	6,39	6,71	6,38	4,13	3,38	2,19
Clear ^{T2}	% of darkening	33,5	66,96	81,04	87	89,75	91,21	92,07	92,78
	s.d. [%]	3,96	3,23	2,12	1,64	1,29	1,14	1,04	1,05
CytoVista	% of darkening	38,62	77,41	89,84	93,55	95,69	100	100	100
	s.d. [%]	11,04	8,96	5,44	3,07	1,11	0	0	0
ScaleS	% of darkening	16,18	36,96	54,31	67,87	76,7	82,92	88,81	93,25
	s.d. [%]	5,91	8,69	8,55	7,29	5,45	4,16	3,13	1,33
Glycerol	% of darkening	8,3	23,09	39	56,69	69,02	76,63	84,83	89,03
	s.d. [%]	3,79	5,58	7,63	8,38	10,25	5,37	6,12	4,55
		DRAQ5							
	Depth [μm]	25	50	75	100	125	150	175	200
PBS	% of darkening	21,35	46,89	64,46	75,15	81,62	85,44	87,89	89,76
	s.d. [%]	6,12	5,91	6,38	6,25	5,7	4,86	4,2	3,55
Mowiol	% of darkening	20,49	44,26	61,45	74,42	83,45	95,65	97,45	100
	s.d. [%]	5,92	6,62	6,99	5,59	5,52	1,49	0,1	0
Clear ^{T2}	% of darkening	30,45	67,3	84,88	92,41	96,62	97,15	97,45	97,67
	s.d. [%]	4,71	3,86	2,15	1,44	0,59	0,41	0,34	0,28
CytoVista	% of darkening	43,89	77,29	88,35	95,71	97,62	97,82	100	100
	s.d. [%]	10,25	4,95	2,5	0,61	0,36	0	0	0
ScaleS	% of darkening	20,59	37,91	55,04	68,23	80,75	91,86	96,34	100
	s.d. [%]	7,88	11,11	11,49	9,93	9,34	3,37	1,04	0
Glycerol	% of darkening	13,06	30,34	44,81	62,69	83,48	90,88	92,64	100
	s.d. [%]	4,46	6,62	8,47	8,68	5,39	5,29	5,29	0

8.4 Overview of fluorescence penetration and SNR in depth of simple spheroids sorted by cell type

Table 8-4: Summary of depth-dependent signal loss and SNR in B7_033#1NPC1 spheroids. Adapted from Nürnberg et al. (2020)^{247, xx}.

B7_033#1NPC1												
	DAPI						DRAQ5					
	Absolute depth [μm]			Normalized depth [μm]			Absolute depth [μm]			Normalized depth [μm]		
	50% signal loss	90% signal loss	SNR < 5	50% signal loss	90% signal loss	SNR < 5	50% signal loss	90% signal loss	SNR < 5	50% signal loss	90% signal loss	SNR < 5
PBS	75	--	103,5	76,6	--	105,7	78	216	139,5	79,6	220,5	142,4
Mowiol	111	220,5	154,5	138,2	274,5	192,4	94,5	190,5	171	117,7	237,2	212,9
Clear ^{T2}	60	153	73,5	81,3	207,2	99,5	64,5	117	123	87,4	158,4	166,6
Cyto Vista	78	118,5	96	143,5	218	176,6	49,5	99	85,5	91,1	182,1	157,3
Sca/eS	102	214,5	133,5	105,4	221,6	137,9	114	211,5	187,5	117,8	218,5	193,7
Glycerol	133,5	237	201	118,9	211,1	179	123	226,5	265,5	109,6	201,8	236,5

Table 8-5 Summary of depth-dependent signal loss and SNR in HaCaT spheroids. Adapted from Nürnberg et al. (2020)^{247, xx}.

HaCaT												
	DAPI						DRAQ5					
	Absolute depth [μm]			Normalized depth [μm]			Absolute depth [μm]			Normalized depth [μm]		
	50% signal loss	90% signal loss	SNR < 5	50% signal loss	90% signal loss	SNR < 5	50% signal loss	90% signal loss	SNR < 5	50% signal loss	90% signal loss	SNR < 5
PBS	40,5	--	64,5	45,4	--	72,2	45	156	87	50,4	174,7	97,4
Mowiol	43,5	103,5	69	56,3	134,1	89,4	49,5	117	105	64,1	151,6	136
Clear ^{T2}	42	154,5	61,5	60	220,6	87,8	48	103,5	96	68,5	147,8	137,1
Cyto Vista	51	121,5	117	95,6	227,7	219,3	66	126	117	123,7	236,2	219,3
Sca/eS	88,5	189	153	103,2	220,4	178,4	84	232,5	205,5	98	271,2	239,7
Glycerol	73,5	--	142,5	84	--	162,8	78	--	195	89,1	--	222,8

^{xx} Contribution from Roman Bruch, see Table 8-10: Contributions from other persons, p. 117

Table 8-6 Summary of depth-dependent signal loss and SNR in CCD-1137SK spheroids. Adapted from Nürnberg et al. (2020)^{247, xx}.

CCD-1137SK												
	DAPI						DRAQ5					
	Absolute depth [μm]			Normalized depth [μm]			Absolute depth [μm]			Normalized depth [μm]		
	50% signal loss	90% signal loss	SNR < 5	50% signal loss	90% signal loss	SNR < 5	50% signal loss	90% signal loss	SNR < 5	50% signal loss	90% signal loss	SNR < 5
PBS	49,5	--	51	54,9	--	56,6	52,5	--	85,5	58,2	--	94,9
Mowiol	75	--	85,5	96,7	--	110,3	103,5	276	154,5	133,5	355,9	199,2
Clear ^{T2}	48	222	54	64,4	297,7	72,4	58,5	199,5	120	78,4	267,5	160,9
Cyto Vista	60	156	105	109	283,5	190,8	73,5	171	142,5	133,6	310,7	258,9
Sca/eS	84	244,5	102	92,2	268,3	111,9	78	303	243	85,6	332,5	266,7
Glycerol	123	327	175,5	132,3	351,7	188,8	127,5	331,5	309	137,1	356,6	332,4

Table 8-7 Summary of depth-dependent signal loss and SNR in HT29 spheroids. Adapted from Nürnberg et al. (2020)^{247, xxi}.

HT29												
	DAPI						DRAQ5					
	Absolute depth [μm]			Normalized depth [μm]			Absolute depth [μm]			Normalized depth [μm]		
	50% signal loss	90% signal loss	SNR < 5	50% signal loss	90% signal loss	SNR < 5	50% signal loss	90% signal loss	SNR < 5	50% signal loss	90% signal loss	SNR < 5
PBS	31,5	--	53,5	50,3	--	85,9	39,5	115,5	81,5	63,2	186,5	131,4
Mowiol	34,5	122,5	58,5	57,4	205,8	97,9	43,5	133,5	89,5	72,5	224,4	150,2
Clear ^{T2}	27,5	--	37,5	49,8	--	68,3	34,5	102,5	68,5	62,8	188,3	125,5
Cyto Vista	50,5	96,5	70,5	109,1	209,4	152,7	56,5	100,5	92,5	122,2	218,1	200,7
Sca/eS												
Glycerol	43,5	151,5	81,5	70,9	249,1	133,6	49,5	121,5	Full Range	80,8	199,6	Full Range

Table 8-8 Summary of depth-dependent signal loss and SNR in HTC-8 spheroids. Adapted from Nürnberg et al. (2020)^{247, xxi}.

HTC-8												
	DAPI						DRAQ5					
	Absolute depth [μm]			Normalized depth [μm]			Absolute depth [μm]			Normalized depth [μm]		
	50% signal loss	90% signal loss	SNR < 5	50% signal loss	90% signal loss	SNR < 5	50% signal loss	90% signal loss	SNR < 5	50% signal loss	90% signal loss	SNR < 5
PBS	45	112,5	45	52,5	131,2	52,5	46,5	124,5	64,5	54,2	145,2	75,2
Mowiol	51	168	40,5	56,8	187	45,1	58,5	184,5	102	65,1	205,4	113,5
Clear ^{T2}	43,5	--	42	52,5	--	50,6	52,5	150	96	63,3	180,9	115,8
Cyto Vista	63	145,5	79,5	96,7	223,3	122	75	162	129	115,1	248,6	198
Sca/eS	85,5	259,5	88,5	84,5	256,6	87,5	81	312	162	80,1	308,5	160,2
Glycerol	84	264	85,5	84,5	265,4	86	85,5	276	232,5	86	277,5	233,7

xxi Contribution from Roman Bruch, see Table 8-10: Contributions from other persons, p. 117

8.5 Overview of fluorescence penetration and SNR in depth in complex 3D cell cultures

Table 8-9: Summary of depth-dependent signal loss and SNR in complex 3D-cell cultures. Adapted from Nürnberg et al. (2020)^{247, xxii}

Triculture												
	DAPI						CellTracker Green					
	Absolute depth [μm]			Normalized depth [μm]			Absolute depth [μm]			Normalized depth [μm]		
	50% signal loss	90% signal loss	SNR < 5	50% signal loss	90% signal loss	SNR < 5	50% signal loss	90% signal loss	SNR < 5	50% signal loss	90% signal loss	SNR < 5
PBS	25,5	90,5	34,5	43,9	158,1	59,7	27,5	--	--	47,4	--	--
Mowiol	38,5	81,5	78,5	70,2	149,6	144,1	30,5	--	--	55,4	--	--
Clear ^{T2}	30,5	80,5	47,5	59,8	159,5	93,7	28,5	--	--	55,8	--	--
Cyto Vista	33,5	71,5	59,5	83,1	178,9	148,6	21,5	--	--	52,9	--	--
Sca/eS	48,5	168,5	67,5	80	279,9	111,6	33,5	--	--	55	--	--
Glycerol	49,5	128,5	88,5	78,3	204,5	140,6	34,5	--	--	54,3	--	--
Dynarrays												
	CellTracker Red						DRAQ5					
	Absolute depth [μm]			Normalized depth [μm]			Absolute depth [μm]			Normalized depth [μm]		
	50% signal loss	90% signal loss	SNR < 5	50% signal loss	90% signal loss	SNR < 5	50% signal loss	90% signal loss	SNR < 5	50% signal loss	90% signal loss	SNR < 5
PBS	--	--	--	--	--	--	--	--	--	--	--	--
Mowiol	58,5	--	--	--	--	--	56,5	--	74,5	--	--	--
Clear ^{T2}	47,5	--	--	--	--	--	44,5	--	64,5	--	--	--
Cyto Vista	42,5	--	--	--	--	--	43,5	--	45,5	--	--	--
Sca/eS	92,5	--	--	--	--	--	91,5	--	115,5	--	--	--
Glycerol	85,5	--	--	--	--	--	74,5	148,5	112,5	--	--	--

^{xxii} Contribution from Roman Bruch, see Table 8-10: Contributions from other persons, p. 117

8.6 Publications

Publication of the results presented in this thesis:

Nürnberg, Elina; Vitacolonna, Mario; Klicks, Julia; von Molitor, Elena; Cesetti, Tiziana; Keller, Florian; Bruch, Roman; Ertongur-Fauth, Torsten; Riedel, Katja; Scholz, Paul; Lau, Thorsten; Schneider, Richard; Meier, Julia; Hafner, Mathias; Rudolf, Rüdiger (2020): Routine Optical Clearing of 3D-Cell Cultures: Simplicity Forward. *Frontiers in molecular biosciences* 7: 20.
DOI: 10.3389/fmolb.2020.00020

Other publications based on techniques established within the framework of this thesis:

Von Molitor, Elena; **Nürnberg, Elina**; Ertongur-Fauth, Torsten; Scholz, Paul; Riedel, Katja; Hafner, Mathias; Rudolf, Rüdiger; Cesetti, Tiziana (2020): Analysis of calcium signaling in live human Tongue cell 3D-Cultures upon tastant perfusion. *Cell calcium* 87: 102164.
DOI: 10.1016/j.ceca.2020.102164

8.7 Statement on contributions, copyright, and self-plagiarism

I, Elina Nürnberg, hereby confirm that this thesis and the data presented therein is the result of my own independent work. Contributions by other persons have been clearly indicated and are listed in summary in the following Table. No other sources than those indicated have been used. Figures were obtained with appropriate permission and sources/licenses are given in the respective figure legends. The figures in the Results section (Section 3) of this work, which include elements from previously published figures as listed in Section 8.6 with proper references in the figure legends, were originally created by me.

Table 8-10: Contributions from other persons

Contributor	Section	Contribution
Bruch, Roman	2.5.1, and 2.5.2	Calculated 50 % and 90 % signal loss depth and depths for Rose criterion
	3.2.3	Data shown in Table 3-1, and Table 3-2 were produced jointly with the methods described above
	3.3.2, 8.4, and 8.5	Data shown in Table 8-3, Table 8-4, Table 8-5, Table 8-6, Table 8-7, Table 8-8, and Table 8-9 were produced jointly with the methods described above
Cesetti, Tiziana	2.1.2	Preparation and culture of HTC-8 spheroids
	3.3	Provided samples of HTC-8 spheroids generated with the methods described above
Keller, Florian	2.1.3	Preparation and culture of Dynarray cocultures of CCD-1137SK and MDA-MB-231 cells
	3.3.3	Provided samples of Dynarray cocultures and participated in data analysis for Figure 3-16
Klicks, Julia	2.1.2	Preparation and culture of CCD-1137SK and melanoma triculture spheroids
	3.3, and 3.3.3	Provided samples of CCD-1137SK and melanoma triculture spheroids with the methods described above
Maxhuni, Samira (supervised Bachelor thesis)	2.1.2, 2.2.1, and 2.2.2	Cultivation of B7_033#1NPC1 cells, spheroid generation; fixation and cryosectioning of B7_033#1NPC1 spheroids with subsequent staining

	3.1.1, and 0	Participated in sample generation, cryosectioning and fluorescence labeling of B7_033#1NPC1 spheroids with the methods described above; participated in data analysis for Figure 3-2 and Figure 3-3
Vitacolonna, Mario	2.1.2	Preparation and culture of HT29 spheroids
	3.3	Provided samples of HT29 spheroids generated with the methods described above and participated in data analysis for HT29 samples
	2.5.3	3D-segmentation of nuclei<
	3.2.4, 0, and 3.3.5	Participated in 3D-segmentation of nuclei with the methods described above.
von Molitor, Elena	2.1.2	Preparation and culture of HaCaT spheroids
	3.3	Provided samples of HaCaT spheroids generated with the methods described above and participated in data analysis for HaCaT spheroids

9 Curriculum Vitae

PERSONALIEN

Vorname, Name: Elina Nürnberg
 Geburtsdatum: 22.08.1986
 Geburtsort: Schwetzingen, Deutschland

SCHULISCHER WERDEGANG

(1997) – (2006) Johann-Sebastian-Bach-Gymnasium, Mannheim
 (20.06.2006) Abitur

UNIVERSITÄRER WERDEGANG

09/2006 – 02/2009	Studium der Verfahrenstechnik an der Hochschule Mannheim
03/2009 – 08/2013	Biotechnologie an der Hochschule Mannheim Abschluss: Bachelor of Science
03/2013 – 08/2013	Bachelorthesis im Biochemischen Labor, Abteilung für Psychiatrie und Psychotherapie, Zentralinstitut für Seelische Gesundheit, Mannheim Thema: “Brain-derived neurotrophic factor plays an essential role in the differentiation of stem cell-derived serotonergic neurons.“
09/2013 – 01/2016	Biotechnology – Biomedical Science and Technology an der Hochschule Mannheim Abschluss: Master of Science
04/2015 – 12/2015	Masterthesis im Biochemischen Labor, Abteilung für Psychiatrie und Psychotherapie, Zentralinstitut für Seelische Gesundheit, Mannheim Thema: “Analyses of a glucocorticoid-mediated stress response in human induced pluripotent stem cell-derived neurons.“
05/2016	Promotion (Dr. sc. hum) im Rahmen des Graduiertenkollegs „Tissue Analytics for Stem Cell-based Diagnostics and Therapy“ an der Medizinischen Fakultät Mannheim der Universität Heidelberg und dem Institut für Molekular- und Zellbiologie der Hochschule Mannheim Thema: “Optimizing Microscopy in Three Dimensions: Optical Clearing Techniques for the Study of hiPSC-Derived Neural Spheroids and 3D Cell Cultures”

10 Acknowledgments

During the life of a PhD student, there are moments, which I firmly believe everyone encounters at some point, where you cannot imagine ever reaching the point of writing this section. And then arrives that moment when you find yourself before a blank page, unsure of where to start, overwhelmed by the multitude who have joined you on this journey, whether from the sidelines or steadfastly by your side through the heart of the storm. There simply isn't enough room on one page to adequately express my gratitude toward all these people.

First and foremost, I want to express my gratitude to Prof. Dr. Mathias Hafner for entrusting me with this project and granting me the opportunity and creative freedom to delve into this topic. Thank you for advice, enriching discussions during our meetings, and the knowledge you have generously shared. Similarly, I want to thank PD. Dr. Thorsten Lau for all his contributions to this project. Your role in shaping me as a researcher and fostering my passion for microscopy and neuroscience has left an indelible mark, and I am grateful the years of support and motivation. I also would like to thank Prof. Dr. Rüdiger Rudolf for his contribution to the optical clearing aspect of this project. Your knowledge, experience, and unwavering support in my abilities consistently provided me with the motivation to expand my personal horizons and explore uncharted territories.

To my colleagues in the Hafner/Rudolf group, both past and present, I want to convey my heartfelt gratitude for your support, valuable advice, the wonderful working atmosphere. Special thanks to Florian, Tiziana, Julia, and Elena for your invaluable contributions to “the clearing paper”. I'd like to extend my deep appreciation to Mario Vitacolonna, my partner in crime when testing new image segmentation algorithms. To Nathalie and Dani, your exceptional expertise and ability to brighten up each day have been truly appreciated. I would also like to express my gratitude to the entire IMZ lab and the STZ for creating such an incredible work environment.

Furthermore, I extend my gratitude to Matteo Rigon, Patrick Williams, and Diego Pastene Maldonado for their enduring friendship throughout the years. I deeply miss those post-work gatherings at the pub. To Patrick, I appreciate your knack for making people approach me to 'fix the internet.' To Dani and Cinzia: thank you for your help in keeping the guys in line.

I want to thank Sarah Hörner for her friendship, for her advice and constant support. I cannot thank you enough for everything you did in the last years, and I will be forever grateful. I promise we will make it to that festival, and there will be more highs, fewer lows, and undoubtedly more music and food in our future.

Ultimately, I want to express my profound gratitude to my family. Without your unwavering support, I would have never come this far. To my mother: thank you for imparting the wisdom that there is always

more strength within, even when one feels depleted. To my father, who ignited my passion for science from the start. Thank you for molding me into both a scientist and a person, for your teachings, and for always showing your pride in me. To my brother Michael, your lesson that being different is a blessing, not a curse, has left an enduring impact. Finally, to my sister Anja, your daily example proves that with sheer determination, one can achieve anything.

To Isabell Moskal: you are family, and none of this journey would have been possible without your friendship. Thank you for your unwavering companionship, for always being there, and for the nights filled with music, laughter, and Even Flow when I needed them most. To Christopher: thank you for over two decades of unwavering friendship and your constant support, no matter the circumstances. Especially while fighting the zombie apocalypse.

Finally, I extend my heartfelt gratitude to Dominik. There are simply not enough words to convey your significance in this journey and in my life. You helped me leave behind the negatives and embrace the positives. You have consistently been the calm amidst my storms, unwavering when I falter, and a source of strength when I need it most. What's more, you don't just encourage me to pursue my dreams; you stand alongside me. Thank you for your boundless love, unwavering support, and all of the fireflies.

“When I reach for the edge of the universe, I do so, knowing that along some paths of cosmic discovery, there are times when, at least for now, one must be content to love the questions themselves”

by Neil deGrasse Tyson